Development And Optimization Of Automated Fibre Production For Recombinant Spider Wrapping Silk

by

Nathan Weatherbee-Martin

Submitted in partial fulfilment of the requirements
for the degree of Master of Science

at

Dalhousie University
Halifax, Nova Scotia
March 2016

Dedication

To my parents (*Doris and Lionel*),

my brother (*Thomas*),

my grandparents,

my closest friend and soul mate (*Alice*),

and everyone else who has been there for me along the way.

Table of Contents

List of Tables

List of Figures

Abstract

Spiders produce up to seven different types of silk, each serving different biological functions. Wrapping silk, used for wrapping of prey, is the toughest of the seven types. Limited information is available on wrapping silk fibre formation and structure. Native wrapping silk protein (AcSp1) in *Argiope trifasciata* consists of a core domain with at least 14 consecutive 200 amino acid repeat ("W") units. A recombinant 3 W-unit protein (W_3) was produced in *Escherichia coli*. Automated fibre production ("spinning") was achieved by solubilization of W_3 in two different solvent-based spinning "dopes", followed by extrusion, dehydration, and post-spin stretching. Post-spin stretching improved fibre strength, enriched β-sheet conformation, and increased birefringence. Additionally, fibre extensibility differed with spinning dope composition, corresponding to differences in anisotropy of secondary structuring, and in birefringence. This high-throughput synthetic recombinant spider silk fibre production methodology will make possible studies of its atomic-level structuring using nuclear magnetic resonance spectroscopy.

List of Abbreviations and Symbols Used

||: Parallel

⊥: Perpendicular

ε: Molar extinction coefficient

θ: Mean residue ellipticity

ΔL: Change in length

σ: Stress

ε: Strain

A: Absorbance

A_o: Original cross-sectional area

AcSp: Aciniform (wrapping) silk spidroin

ADF: *Araneus diadematus* fibroin

AFM: Atomic force microscopy

AS: As-spun

c: Concentration

CD: Circular dichroism

dH_2O: Distilled water

EtOH: Ethanol

F: Force

Flag: Flagelliform silk

GPa: Gigapascals

H_6: Hexahistidine

HFA: Hexafluoroacetone

HFIP: 1,1,1,3,3,3-hexafluoro-2-propanol

IPA: Isopropyl alcohol

IPTG: Isopropyl β-D-1-thiogalactopyranoside

L_o: Original length

LB: Luria-Bertani

MA: Major ampullate (dragline) silk

MaSp: Major ampullate (dragline) silk spidroin

MeOH: Methanol

MiA: Minor ampullate silk

NMMO: N-methylmorpholine-N-oxide

PEEK: Polyetheretherketone

PS: Post-spun

PZT: Piezoelectric

RN: Reversible needle

SEM: Scanning electron microscopy

Sp: Spidroin (spider silk protein)

SUMO: Small ubiquitin-like modifier

TFA: Trifluoroacetic acid

TFE: 2,2,2-Trifluoroethanol

TuSp: Cylindriform/tubiliform silk spidroin

UV: Ultraviolet

W: Repeat unit

W/v: Weight/volume

Acknowledgements

I would like to first thank my supervisor Dr. Jan K. Rainey. Ever since I joined his lab as a co-op student in 2012, he has supported me and guided me in so many ways. He has not only shaped me into the scientist and individual I am today, but he has also opened many doors of opportunity for me. After giving me the opportunity to join his lab as a graduate student, I began to realise what a great supervisor and person he is. He consistently provided me with an environment where I was free to explore my ideas, and control the direction of my work, as well as steered me into the right direction whenever I needed it. I believe that Jan has always looked out for my best interests, and I am truly grateful for that.

During my time in Jan's lab, both past and present, I have had the honour of working with many wonderful people. If it was not for them and their support, my experience would not have been nearly as enjoyable. That being said, I would like to thank Marie-Laurence Tremblay, Aditya Pandey, Kyungsoo Shin, Nigel Chapman, Robin Patterson, Danielle LeBlanc, Sara Sparavalo, Aaron Banks, Matthew Speckert, Lesley Seto, Kathleen Orrell, Ellie Scott, Bruce Stewart, Pascaline Ngweniform, Emily Truong, Johnny Farah, Doug Miller, Jessi Bak, Kate Huang, Ben Morash, Calem Kenward, Andy Song, Muzaddid Sarker, and Lingling Xu. In particular, I would like to thank Marie for training me and being an excellent mentor as well as a friend when I first joined the lab. I want to thank Adi, Kyung, and Nigel for not only being great support and guidance, but also for being great friends. The same goes for everyone else. I also want to thank Bruce for all the technical support that I needed along the way. As well, I want to thank Lingling, because without her I do not think I would have reached this point.

There are also many other people outside the lab that I would like to thank. First I would like to thank my committee members Drs. Laurent Kreplak and Paul Xiang-Qin Liu

for helpful discussion, constructive criticism, and their willingness to help me whenever I needed it. Thank you Drs. Laurent Kreplak, David Waisman, and J. Michael Lee for providing access to equipment that were essential for experiments. Thank you Sam Baldwin for providing valuable information about the instrumentation that I used in Dr. Laurent Kreplak's lab. Thank you Brandon Scott for providing assistance in Dr. J. Michael Lee's lab when I needed it. Thank you Dr. Melanie Dobson, Joyce Chew, and Mary McQuaid for advice and encouragement along the way, as well as sharing of equipment. Paul Briggs and Heidi MacKinnon also deserve my gratitude for making my teaching assistantship experience an enjoyable one, as well as providing technical support whenever it was needed. Thank you Dr. Douglas S. Fudge and Andre Hupe at the University of Guelph for collaborating and providing access to equipment crucial for some experiments. Thank you Kevin Borgel and John Noddin for building the instruments that were required for many experiments. Both of them consistently provided great service and quality in everything that they did. Thank you Dennis Baev for your assistance with building these instruments. I also want to thank NSERC for the CGS-M award, which has been great support for me in graduate school.

I would like to thank my parents, Doris and Lionel, for allowing me to realise my own potential. More importantly, I am grateful for their continuous love, support, encouragement, and understanding. I would like to thank my brother, Thomas, for always being there for me and being a genuinely great person. The same goes for my grandparents who time and time again are always there for me. Last but not least, I would like to thank Alice, for her strong love and support.

Thank you!

Chapter 1: Introduction

The overall objective of this work was to develop an understanding of formation and structure of aciniform (wrapping) silk fibres. Specifically, this work is based on artificial production of recombinantly produced wrapping silk fibres. In this chapter, I introduce fundamental knowledge of spiders and their silk. I then discuss our current understanding of the processes involved in natural spider silk production, particularly focusing on major ampullate (MA), or dragline silk, as it is the only extensively characterized form of spider silk. This is followed by a comparison of primary and secondary structures of different silk types and an explanation of how these seem to play a role in the functional (i.e., mechanical) properties of these nanomaterials. After this introduction, I discuss the manner in which artificial production was developed and used on recombinant wrapping silk protein (Chapter 2) and then detail the biophysical, mechanical, and morphological properties of the resulting fibres (Chapter 3). I then focus on optimization of some of the methodologies developed in Chapter 2 based on experimental results gathered in Chapter 3, followed by characterization of fibres produced from this optimized method (Chapter 4). In Chapter 5, I conclude with potential for future development stemming from this project.

1.1 Spiders and Their Silk

The impressive properties of spider silks, such as high tensile strength and extensibility, have been crafted by evolutionary pressure and have promoted the survival of spiders over the last ~400 million years (1,2). The dependence of spiders on their silk for evolutionary success has driven the development of seven different types of protein-based self-assembling nanomaterials with various biological functions (3,4). Specifically, female orb-weaver spiders can produce up to seven types of silk (Figure 1.1) (3-5). The varying

biological functions of these silk materials are as follows: MA silk acts as structural silk and functions in locomotion; minor ampullate (MiA) silk is responsible for the auxiliary spiral of a web; wrapping silk is involved in sperm webs, soft inner lining of egg sacs, web decorations, and wrapping and immobilization of prey; cylindriform/tubiliform silk functions in coating the outer egg sac; flagelliform (Flag) silk is the fibrous component of the capture spiral web; aggregate silk allows for aqueous coating of the capture spiral web; and, pyriform silk is responsible for the cement and joints for attachments of different silk types (1,2,4-6).

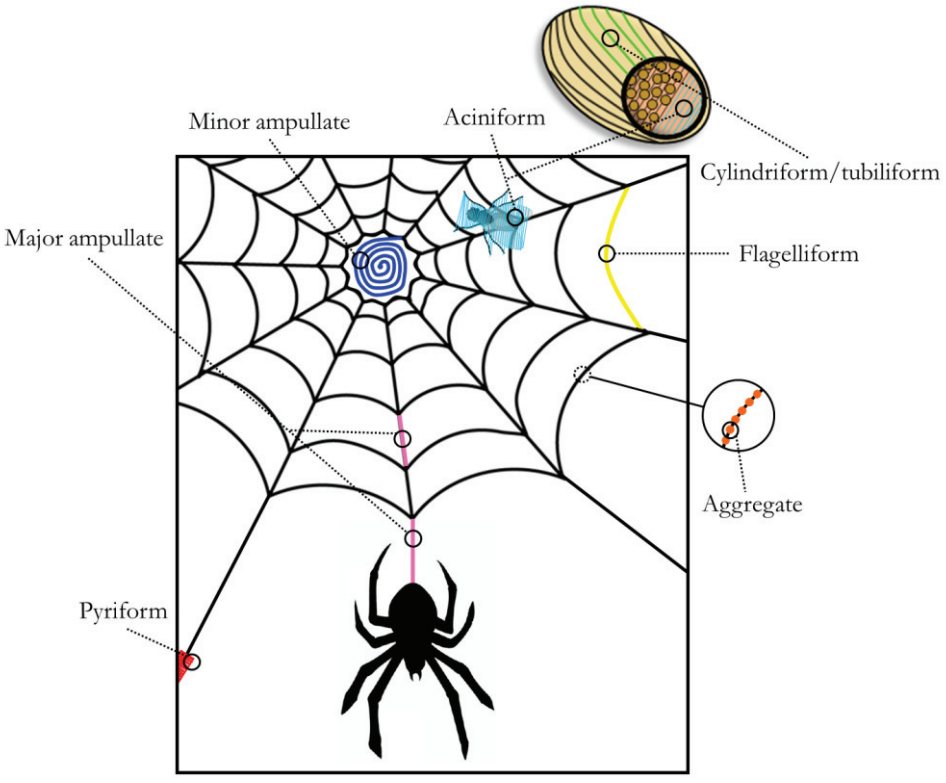

Figure 1.1 Schematic of the seven different types of spider silk and their various biological functions. Each colour corresponds to a particular silk type produced from an independent gland: major ampullate silk functions in locomotion and structure (pink), minor ampullate silk functions in the auxiliary spiral of a web (blue), aciniform silk functions in the soft inner lining of egg sacs and capturing prey (cyan), cylindriform/tubiliform silk functions in the outer coating of egg sacs (green), flagelliform silk functions in the core fibres of a capture spiral web (yellow), aggregate silk functions as an aqueous coating of a capture spiral (orange) and pyriform silk functions as cement for joints and attachments (red).

1.1.1 Our Current Understanding of Natural Spider Silk Production

Most of our knowledge on spider silk fibre formation and structure pertains to MA silk, with a particular focus on two types of silk protein: MaSp1 and MaSp2 found within the *Nephila* genus (7). This follows a common nomenclature used for different silk types: the first two letters relate to the gland where the gene/protein are expressed (Ma); the following two letters are for spidroin (Sp), a term defined as spider silk protein; and, the number represents the paralogue number of the spidroin (in this case 1 or 2) (5).

Although each gland for a particular silk type has a different shape and size (2,5,8,9), Lewis (2) has suggested that they are all functionally organized in a similar manner. In particular, each gland has a location(s) where spidroins are produced, followed by a central location where the protein is stored/solubilized (resulting in a suspension referred to as the spinning dope) and a narrow spinning duct promoting protein self-assembly and fibre formation. The spinning duct(s) exits through a protruding spinneret(s) containing a combination of many tubes called spools and spigots, where the spools and spigots are microscopic protrusions from the spinneret(s) (2,5,10). Each spinning apparatus consist of three pairs of spinnerets (anterior, median, and posterior), which vary in size and in microstructural organisation depending on the type of silk being produced (2,5,10). Additionally, these spinnerets have a muscular valve, which allows for a controlled flow rate of silk production (2,5,10). The scanning electron micrographs in Figure 1.2 of adult female orb-weaver spiders, *Argiope bruennichi* (10), demonstrate this.

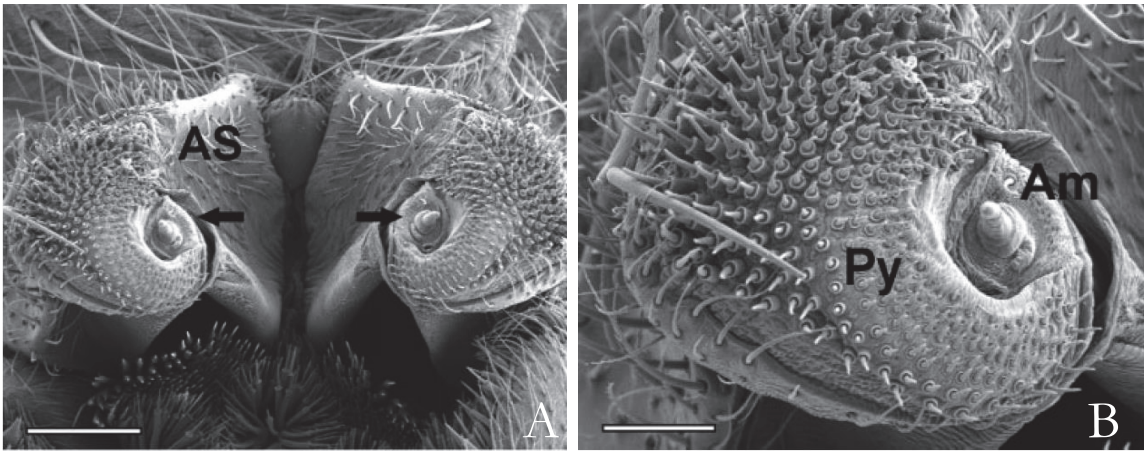

Figure 1.2 Scanning electron micrographs of adult female orb-weaver spiders, *Argiope bruennichi*. A pair of anterior spinnerets (AS) with a pair of MA spigots (arrows) surrounded by 200 pairs of distributed pyriform spools (A). Increased magnification showing the pair of MA (Am) spigots separated from the pyriform (Py) spools (B). Scale bars represent 250 μm (a) and 100 μm (b). This figure is reproduced with permission from John Wiley and Sons. (Moon, M. J. Organization of the spinnerets and spigots in the orb web spider, *Argiope bruennichi* (Araneae: Araneidae). Entomological Research. 2012; 42: 85-93.)

In addition, it is known that spidroins of different silk types vary in size from 250-500 kDa but are all organized in a tripartite structure (Figure 1.3) consisting of a central repetitive core domain capped by two (<150 amino acid (aa)) non-repetitive globular N- and C-terminal domains (2,5,11-13). Importantly, the repetitive core domain varies greatly from spidroin to spidroin while both terminal domains are evolutionarily conserved across most spidroins (2,5,11-13). Such spidroin-dependent vs. –independent properties imply essential roles for the former in imbuing functional variability and the latter in the mechanisms of natural spider silk production, as discussed in more detail shortly (section 1.1.3).

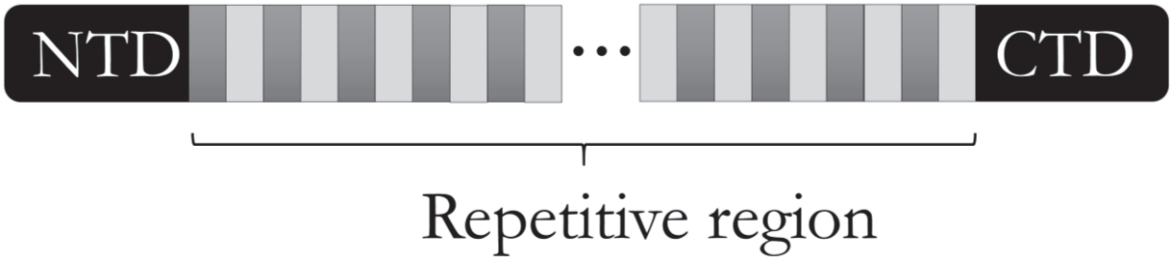

Figure 1.3 Representative tripartite primary structure of spider silk proteins. The structure consists of a highly repetitive region flanked by N- and C-terminal domains.

1.1.2 A Biochemical Overview of MA Spider Silk Glands

Despite Lewis' contention that all spider silk glands are similar in functional organisation (2), the MA gland has an exquisitely complex set of biochemical changes that occur over the long axis of the silk gland (Figure 1.4). In particular, the nuances of spidroin production, spidroin solubilization, and spidroin assembly into silk seem unlikely to be identical from gland to gland given the dramatically different anatomical features of each (2,5,8,9). With this caveat in mind, since most of the available information on natural spider silk production is focused on MA silk, MA silk glands will be described.

The spinning apparatus used to make MA silk consists of four regions (labelled 1-4), as shown in Figure 1.4. Each of the first three regions contains its own cell types, as will be detailed shortly (11,14). Figure 1.4 also indicates the presence of a decreasing pH gradient from the proximal region (winding tail, pH ~8) to the distal region (spinning duct, pH ~5) (5,15). Although not explicitly illustrated in Figure 1.4, an ionic gradient is also present in which there is four-fold increase in potassium ions with a simultaneous increase in phosphate ions and a one-tenth decrease in sodium and chloride ions from the proximal to distal regions (15).

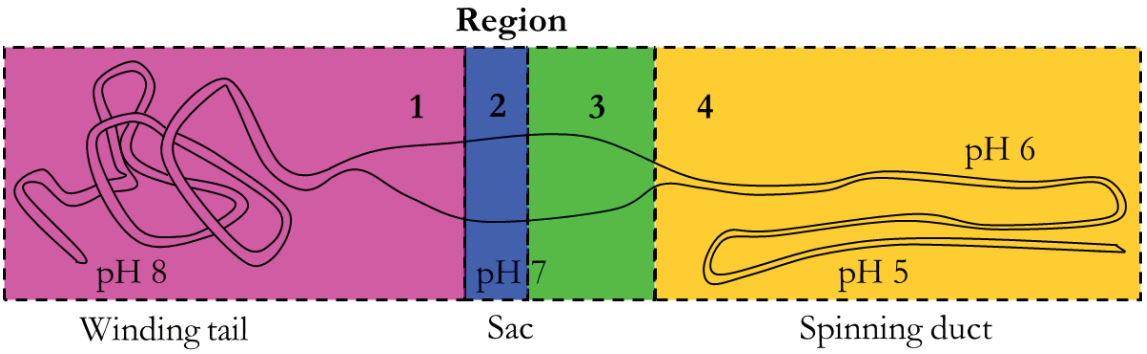

Figure 1.4 Schematic of the MA silk gland spinning apparatus. The pH gradient that is present along the gland is illustrated. Spidroin production takes place in the winding tail and the sac, where epithelial cells produce spidroins as a high concentration dope. Toward the end of the sac and beginning of the spinning duct, lower pH and pressurized CO_2 (pCO_2) is generated to promote pre-assembly of spidroin silk (region 3). Finally, in the spinning duct, spidroin assembly into fibres occurs (region 4). This figure was adapted from Rising and Johansson (5).

Andersson and colleagues (11) have found that regions 1 and 2 contain two different types of epithelial cells that secrete both MaSp1 and MaSp2. Shortly afterwards, Andersson and colleagues (14) discovered that region 3 has high levels of active carbonic anhydrase, which is responsible for generating pCO_2 and protons (H^+), thereby decreasing pH. This decrease in pH plays a role in inducing pre-assembly of the solubilized spidroin prior to entry into the spinning duct (14). Beyond region 3 is the spinning duct, which essentially dehydrates the dope and promotes alignment of the protein molecules by shearing forces, which are the result of elongational flow (see section 2.1.3.2) (5).

A remarkable feature of this apparatus is the ability to store the spinning dope, an aqueous solution containing 30-50% (w/v) soluble protein, in the sac (16,17). There have been two proposed models of how these spidroins may be organized in solution. In the first model, proposed by Jin and Kaplan (18), micelles are formed from spidroins. This is proposed to take place through an arrangement where the terminal domains act as hydrophilic surface exposed headgroups and the repetitive core domain forms the

hydrophobic center. It is important to note that this model was based on *Bombyx mori* silkworm silk and not spider silk. However, *in vitro* micelle formation has been observed with recombinant spider MA silk-based proteins (19,20) and recombinant spider wrapping silk-based proteins (21), implying that the Jin and Kaplan mechanism may apply more generally. The second model was proposed by Vollrath and Knight (9), who suggested that the spinning dope is liquid crystalline in nature and that progression through the gland leads to increased orientation within the liquid crystal. In particular, it is thought that spidroins form what is known as a nematic liquid crystal phase, where they maintain the ability to flow as a liquid while also having behaviour characteristic of a crystal with increasing orientation as the spinning dope progresses through the gland. This model was based on spider MA silk. Considering the basis of these two models, it can be suggested that perhaps they are not mutually exclusive; rather, they may act in conjunction with one another. As well, beyond different silk types, spidroins may behave differently *in vivo* as compared to *in vitro* – it should be noted that the same spidroin may behave differently *in vitro* depending on the nature of the spinning dope and process. This will become clearer with the results reported and discussed in the following chapters.

1.1.3 Molecular Mechanisms of Spidroin N- and C-Terminal Domains Involved with Solubilization and Spider Silk Fibre Assembly

Currently, it is understood that by responding to both the pH and ion gradients along the MA gland, the N- and C-terminal domains both stabilize spidroin structure in solution and promote spidroin polymerization (22). As the spidroin passes from the proximal to the distal regions of the gland (Figure 1.4), the N-terminal domain is initially monomeric, with a transition into loose homodimeric form with other spidroin N-termini and then forms stable

dimers, essentially inducing interdigitation of the spidroins (22). The C-terminal domain (a disulfide linked homodimer in the oxidized state) is initially α-helical, then becomes destabilized and transforms into β-sheet fibrils, triggering polymerization of the spidroins (22). This set of processes for spider silk formation has been termed a "lock and trigger" mechanism (14,22,23).

Ultimately, the stage between solubilization and polymerization of the spidroins is initiated at region 3 (Figure 1.4), where pH is decreased even further by carbonic anhydrase alongside a simultaneous increase in pCO_2 (14,22,23). Stable dimer formation by the N- and C-termini are proposed to allow for structural transformation of the spidroins, and, likely, refolding of the repetitive regions (14,22,23). In addition to the structural changes induced by changes in pH and pCO_2, shearing forces resulting from elongational flow are produced in the spinning ducts, which likely further promotes β-strand structural transitions (14,22,23). The lock and trigger mechanism, providing a dramatic transformation of properties between the stored soluble to fibrous states, in addition to shearing forces combine to allow rapid fibre production at speeds reaching greater than 1 m/s (5).

1.1.4 The Link between Primary Structure and Mechanical Properties

When comparing mechanical properties (described in section 3.1.2) of both synthetic and natural fibres as a function of material mass, spider silk is stronger than steel, more extensible than nylon, and tougher than Kevlar (Table 1.1). Although it is known that the terminal domains play a role in solubilization and polymerisation of the spidroins, we know that, at least in MA silk proteins, they are not directly involved in the resulting mechanical properties of fibres (20). Instead, it is the central repetitive core domain within the spidroin tripartite structure that correlates and likely contributes to certain mechanical properties (2,15,20,24,25). Among the different types of silk, three categories will be described based on

the MA, the Flag, and the wrapping silks, which are the strongest, the most extensible, and the toughest silk fibres, respectively (Table 1.1).

Table 1.1 Mechanical properties of well-known synthetic and natural fibres alongside four different types of natural spider silk fibres. References are provided in the footnote for the given spider genera and species.

Source of materials	True stress (MPa)	True strain (%)	Young's modulus (GPa)	Toughness ($MJ \cdot m^{-3}$)
Steel (26)	1500	0.8	200	6
Kevlar 49 (26)	3600	2.7	130	50
Nylon 6.6 (26)	950	18	5	80
Elastin (26)	2	15	0.001	2
Wool (26)	200	5	0.5	60
B. mori cocoon (26)	600	18	7	70
MA silk[a]	880-4700	21-33	1.2-8.6	90-194
MiA silk[b]	923-1400	22-33	8.9-10.6	137-150
Flag silk[c]	534-1338	119-175	0.001	75-283
Wrapping silk[d]	1052	40	9.8-10.4	230-376
Source of materials	**Engineering stress (MPa)**	**Engineering strain (%)**		
MA silk[e]	600-1217	23-40		
MiA silk[f]	483-669	34-56		
Flag silk[c]	95-296	329-475		
Wrapping silk[d]	636-687	51-83		

[a] *Argiope argentata* (27), *Araneus sericatus* (28), *Araneus diadematus* (29), *Araneus gemmoides* (30), and *Argiope trifasciata* (31).
[b] *Argiope argentata* (27), *Argiope trifasciata* (13), and *Araneus gemmoides* (30).
[c] *Argiope argentata* (27), *Araneus sericatus* (28), and *Araneus diadematus* (29).
[d] *Argiope argentata* (27) and *Argiope trifasciata* (13).
[e] *Argiope argentata* (27), *Araneus sericatus* (28), *Araneus diadematus* (29), and *Argiope trifasciata* (31).
[f] *Argiope argentata* (27), *Argiope trifasciata* (13), and *Araneus diadematus* (32).

1.1.4.1 The Strongest Type of Spider Silk: MA Silk

Of all of the spider silk types, MA silk is the strongest (Table 1.1). The first reported sequence of a MA spidroin was deduced from a partial cDNA library of the golden silk orb-weaver *Nephila clavipes* MaSp1 (33), followed by a second MA spidroin sequence, MaSp2, from the same species (34). Both sequences encoded for repeats of the repetitive core domain through to the C-terminal domain. Shortly thereafter, additional partial sequences of

MA spidroins from *N. clavipes*, *Araneus bicentenarius*, and *Araneus diadematus* were published (35,36). Recently, sequencing has been reported for the N-terminal domains of *N. clavipes* MaSp1 (37), *Euprosthenops australis* MaSp1 (38), and on both MA spidroins from *N. inaurata*, *Latrodectus aeometricus*, and *Argiope trifasciata* (39). Two complete gene sequences for MaSp1 and MaSp2 have also been described in the Western black widow, *L. hesperus* (12).

Generally, MaSp1 and MaSp2 are large proteins having a molecular weight of around 200-350 kDa, consisting of a core domain (~40 aa) that is repeated at least a hundred times (12,24,40) with Ala_n spaced by Gly/Pro-rich repeats (15,16), flanked by two non-repetitive terminal domains (100-200 aa; Figure 1.3) (41,42). Since the repetitive core domain is not conserved across different genera and species, there is some variability in aa composition (27,43,44). However, in all reported cases, the composition is high in both Gly and Ala, which is reflected in functional attribution to motifs (27,43,44), as discussed in more detail below. Notably, Pro levels are also high with higher proportions in MaSp2 relative to MaSp1 (27,43,44).

Examining the repetitive domain in more detail, the most common aa motifs found in MA spidroins are: $(GA)_n/A_n$, GGX, and GPGXX (where X = Ala, Gly, Tyr, Ser, Leu, or Gln) (2,24,25,40). When these motifs are linked together, they form what is known as ensemble repeats (12). Ensemble repeat units that are rich in Ala have been attributed to providing high tensile strength in these silk fibres through the formation of stacked crystalline β-sheets (45,46), whereas regions rich in Gly have been attributed to promoting extensibility because of the so-called amorphous regions surrounding the crystalline β-sheets (47,48). The structures corresponding to these motifs have been studied both in solution form and fibrous form (16,49,50). In solution, MaSp's consist of 30% α-helices/30% β-turns and 40% random coils, with a complete loss of α-helical character, and a conformational

transformation into 36-37% β-sheets during fibrillogenesis surrounded by amorphous regions, parallel to the fibre long axis (16,49-51). Although this appears to be a global conformational transition of spidroins from the solution-state to fibrous state (8,16,17,49-51), because the detailed spectroscopic studies have only focused on one genus, there may be variability in the nuances of these transformations.

1.1.4.2 The Most Extensible Type of Spider Silk: Flag Silk

Compared to other spider silk fibres, Flag silk is known for its high extensibility (Table 1.1). The first reported Flag silk protein sequence was characterized from cDNA of *N. clavipes* (7). Shortly thereafter, this was followed by two more partial sequences from *N. clavipes* and *N. madagascariensis* (52). Recently, sequences have been taken for recombinant Flag silk proteins from *N. clavipes* (53).

Similar to MA silk proteins, Flag silk proteins contain a highly repetitive core domain, flanked by conserved non-repetitive terminal domains (24). However, the C-terminal domain of Flag silk proteins is not homologous to MA silk proteins (2). Similar to the MA silk proteins, there is a high Gly content, but this is coupled with contrastingly low Ala content and high Pro content (27,43,44).

As with the MA silk proteins, Flag silk proteins share common motifs, but lack A_n motifs. Conversely, they have a conserved complex spacer unit containing many charged hydrophilic aa's unlike any other silk protein (2,24,25). The structural and/or functional role of this spacer unit is still not fully understood (2), but it was recently found by Adrianos and colleagues (53) that the spacer units in synthetic Flag silk-like fibres contribute to strength. Just as with the MA silk, it has been suggested that the extensibility of Flag silk can be attributed to high Gly and Pro content (2,24,25). As a comparison to native silk proteins found in the *Nephila* genus, MaSp2 contains up to 9 GPGXX-motifs repeated in each

ensemble repeat unit (24,40), whereas Flag silk proteins contain at least 43 of these GPGXX-motifs repeated per ensemble repeat unit (7). Interestingly, enrichment with this motif in Flag silk corresponds nicely to an increase in extensibility (Table 1.1), which reinforces the idea that Gly-rich regions are attributed to extensibility. This also correlates to synthetic Flag silk-like fibres, where Adrianos and colleagues (53) also reported that the GGX motifs were found to contribute to extensibility.

1.1.4.3 The Toughest Type of Spider Silk: Wrapping Silk

Wrapping silk is the toughest of all spider silk fibres (Table 1.1), and is predominantly made up of aciniform spidroin (AcSp1). Partial sequencing on AcSp1 has been carried out for the banded orb-weaver garden spider *Argiope trifasciata* (13), the cob web-weaver Western black widow *L. hesperus* (54), and the feather-legged orb-weaver *Uloborus diversus* (55). However, one full sequence of AcSp1 was taken for *L. hesperus* (12).

AcSp1 is typically a large protein (~300-430 kDa), and unlike the core domains found in MaSp and Flag silk proteins, AcSp1 is composed of at least 14 highly conserved 200-aa long iterated repeats (termed W units) comprising >95% of the protein sequence (2,12,13,54). To emphasize how conserved the core domain is, at the DNA level there is 99.9% similarity across 600-base pair units within the repetitive region (13). As with other spidroins, AcSp1 is also flanked by conserved N- and C-terminal domains (Figure 1.5) (2,12,13,54). Compared to MA and Flag silk, wrapping silk has a relatively wide distribution in aa composition (27,43,44).

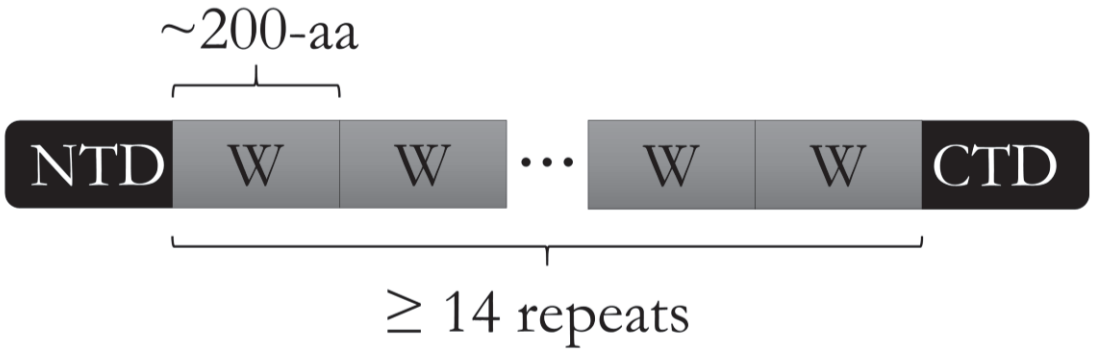

Figure 1.5 Representative tripartite primary structure of AcSp1 in *Argiope trifasciata*. The structure consists of 200-aa long iterative repeat units (W) capped by an N- and C-terminal domain.

In contrast to the MA and Flag silk proteins, AcSp1 does not contain any of the previously mentioned $(GA)_n/A_n$, GGX or GPGXX motifs or a spacer unit (2,12,13,54). Because of this, the link between structure and function remains elusive in wrapping silk, although recently a study was conducted by Wang and colleagues (56) who examined the role of the C-terminal domain in AcSp1. They found that the C-terminal domain promoted fibre assembly from shear force, but did not promote stability of the spidroin in solution as seen with the MaSps (56). However, this is restricted to only one terminal domain, and the behaviour in promoting stability of the spidroin in solution may change in the presence of the N-terminal domain, and may also change in a changing ion and pH gradient. This is already apparent with the intricate molecular mechanism seen with both terminal domains in the MaSps (14,20,22,23).

Between the soluble and fibrous forms, it is known that AcSp1 also undergoes a structural transition. Although conceptually similar to the MA silk transformation, this results in a highly distinct fibrous structuring. In the dope, AcSp1 is in a state composed of 50% globular helical domains connected by 50% disordered linkers (57). Upon fibre formation, the protein retains a similar proportion of disorder alongside a mixture of moderately

oriented β-sheets (~30%) and α-helical (~24%) domains (8,58). As with the MA and Flag silk proteins, the conformational transformation from α-helix to β-sheet is believed to be a key component in providing strength to silk fibres (59). However, the retention of significant α-helical content in the fibre is distinct. Given the unique toughness of wrapping silk, this may be an essential structural feature that promotes this property, and will be returned to later.

1.2 Rationale and Objectives

As detailed above, spider silks are extraordinary biomaterials with diverse and impressive mechanical properties. They are also biodegradable, making them desirable for many downstream applications in industry and medicine (3,4,15,60,61). Because of this, understanding and controlling spider silk fibre formation is very attractive. Since limited information is available on spider silk fibre formation and structure in wrapping silk, this topic is not only very relevant in a structural biology lab such as Dr. Jan Rainey's, but is also essential in providing new knowledge of a poorly understood yet remarkable type of silk.

The first objective of the work described in this thesis was to develop an artificial fibre production method using a recombinantly produced wrapping silk protein. This involved producing the recombinant wrapping silk protein, solubilizing it, and developing a method from this feedstock to allow for robust and reliable artificial fibre production. The second objective of this work was to characterize the biophysical, mechanical, and morphological properties of these newly formed protein-based fibres. This will, in turn, allow production of fibres for future study using solid-state nuclear magnetic resonance spectroscopy that will make possible the first atomic-level characterization of a spider wrapping silk fibre.

Chapter 2: Recombinant Spider Wrapping Silk Protein Production, Protein Solubilization, and the Development of an Automated Fibre Production Method

2.1 Introduction

As introduced and discussed in Chapter 1, I provided an overview of our current understanding of spider silk by exploring the intricate processes involved with the production, storage, and assembly of silk proteins into different types of functional nanomaterials, primarily in the form of fibres. It is clear that a key component of this complex process arises from the hierarchical molecular structure of the spidroins from the primary through to quaternary structure levels. With that being said, most of our knowledge of fibre formation and structure pertains to MA silk, with little known as of yet for wrapping silk. In this chapter, I focus on understanding more about fibre formation in wrapping silk using recombinantly produced wrapping silk protein, which is then used for the development of an artificial fibre production method.

2.1.1 Recombinant Spider Silk Protein Production

Unlike silkworms, spiders are cannibalistic and territorial in nature, making it infeasible to collect large amounts of silk for commercial applications (3,4,21). As well, it has been found that spiders produce silk in lower quantities when held in captivity, making collection of large amounts even more difficult (62,63). Currently, making recombinant spider silks using different host cells is by far the most effective way to produce artificial spider silks. At present, yeast cells (64); mammalian cells (65,66); insect cells (67); bacterial

cells (21,53,56,66,68-74); and, transgenic plants (75,76) and animals (77-80) have been used to produce recombinant spider silks. However, an *Escherichia coli* system has many advantages over other methods because of the potential for high yields, cost effectiveness, and simplicity in cultivation and protein purification. It is also the most commonly used system for recombinant spider silk protein production (20,21,53,56,66,68-74,81-84). Since fibre formation in wrapping silk is poorly understood and harvesting large amounts of fibrous material from spiders is not feasible, employment of a recombinant spider wrapping silk protein is therefore highly desirable and relevant to this work.

2.1.1.1 Recombinant Spider Silk Proteins and Wrapping Silk

As described in Chapter 1 (section 1.1.4.3) and based on proteins used in this work, native wrapping silk in *Argiope trifasciata* consists of a core domain with at least 14 consecutive 200-aa repeat units (W). Recombinant wrapping silk protein constructs with varying numbers of W units, termed W_n, have been successfully produced in *E. coli* (21,57,82,85). Specifically, a single repeat unit (199-aa) of AcSp1, designated W_1, from *Argiope trifasciata* has been produced (21,57,82,85). Additionally, proteins comprising two to four of the AcSp1 200-aa repeat units, W_2 to W_4, have also been produced (21,57). Information pertaining to construction of recombinant plasmids, protein expression, and purification of these protein constructs can be found in work described by Xu and colleagues (21).

Each of these protein constructs is initially N-terminally fused to a 106-aa N-terminally hexahistidine (H_6)-tagged small ubiquitin-like modifier (SUMO) protein tag (21). The SUMO protein fusion partner was employed to enhance protein expression through its ability to increase stability and solubility of the fusion protein, allowing for an increase in protein expression (86). This is evident when comparing the protein yield (10-40 mg/L) of W_3 (~57.1 kDa) designed by Xu and colleagues (21) to other similar sized recombinantly

produced spider silk proteins (Table 2.1) without the use of SUMO tags. SUMO protein tags can also be readily removed after site-specific cleavage by SUMO protease, leaving no residual amino acids (21,86). In short, fusion of a H_6-SUMO protein tag to a protein of interest allows for not only an increase in protein expression, but also for straightforward purification by immobilized metal affinity chromatography alongside the ability to proteolytically cleave the fusion partner using SUMO proteases (86).

Table 2.1 Summary of recombinant spider silk protein production and purification methods previously used. These proteins have been used for artificial fibre production by means of wet-spinning methods.

Protein origin	Expression system	Recombinant protein	Protein size (kDa)	Protein yield (mg/L)	Protein purification method	Reference
AcSp1	*E. coli* BL21(DE3)	W_3[a]	57.1	10-40	Nickel affinity chromatography	(21)
MaSp2	*E. coli* BL21(DE3)	1E (GPG-rich)1Ala8	80	n.d.	Nickel affinity chromatography using an AKTA Explorer	(68)
		2E (GPG-rich)2Ala8	91	n.d.		
		3E (GPG rich)3Ala8	86.5	n.d.		
MaSp and Flag	*E. coli* BL21(DE3)	G (GGX-rich)	54	0.05	Nickel affinity chromatography using an AKTA Avant 150 instrument	(53)
		GY (GGX and GPGGX-rich)	60	0.5		
		GF (GGX-rich and spacer motifs)	59	0.005		
		GFY (GGX and GPGGX-rich with spacer motifs)	66	0.05		
MaSp1	Metabolically engineered (modified) *E. coli*	16 mer	54.6	n.d. (low expression level)	Cell lysis, precipitation and solubilization	(74)
		32 mer	100.7			
		48 mer	146.7			
		64 mer	192.8			
		80 mer	238.8			
		96 mer	284.9			
TuSp1 and ECP (Thioredoxin and H_6-tag)	*E. coli*	1XC	45	7.2	Nickel affinity chromatography; precipitation and solubilization	(70)
		1X	33	4.8		
		ECP-2C	52	n.d.		
		ECP-2N	41			
MaSp and Flag	*E. coli* BL21(DE3)	(A1S8)20	58	n.d.	Nickel affinity chromatography	(72)
		(Y1S8)20	62			
TuSp (RP) and MiSp (CTD)	*E. coli* BL21(DE3)	11RPC	Dimer: 378 Monomer: 189	40	Nickel affinity chromatography	(71)
MaSp1 and MaSp2	*E. coli* BL21(DE3)	NcDS	43	n.d.	Cell lysis, precipitation and solubilization, nickel affinity chromatography or ion exchange	(83)
		$[(SPI)_4/(SpII)_1]_4$	55.7			
		$[(SPI)_4/(SpII)_1]_4$	55.7			

Protein origin	Expression system	Recombinant protein	Protein size (kDa)	Protein yield (mg/L)	Protein purification method	Reference
MaSp2 Analogue (ADF3)	Baby hamster kidney (BHK) cells	ADF3	60	25-50	Cell lysis, precipitation and solubilization	(66)
MaSp1	*E. coli* BL21(DE3)	(MaSp1)16	46	n.d.	Heat treated at 80 °C and nickel affinity chromatography	(69)
		(MaSp1)24	70	n.d.		
MaSp2 Analogue (eADF3 variants)	BLR(DE3)	$(AQ)_{12}$	48	10-30	Cell lysis, heat treated at 70 °C, precipitation, solubilization and nickel affinity chromatography	(20)
		$(AQ)_{24}$	95			
		$(AQ)_{12}$NR3	64			
		$(AQ)_{24}$NR3	112			
		N1L$(AQ)_{12}$	Dimer: 120 Monomer: 60			
		N1L$(AQ)_{24}$	Dimer: 212 Monomer: 106			
		N1L$(AQ)_{12}$ NR3[a]	Dimer: 152 Monomer: 76			
		N1L$(AQ)_{24}$ NR3[a]	Dimer: 268 Monomer: 134			
MaSp1 and MaSp2	transgenic goats	rMaSp1 and rMaSp2	200-350	n.d.	Tangential flow filtration, precipitation and washing	(81)

[a] Produced using the SUMO system.

2.1.2 Solubilization of Artificial Silk Proteins (Spinning Dope)

Once the protein has been expressed and purified, solubilizing it is the next task. The spinning dope is known to be an essential component involved in spinning fibres and can also influence fibre mechanical properties (20,83). In most wet-spinning (fibre production) protocols, 1,1,1,3,3,3-hexafluoro-2-propanol (HFIP) has been used (Table 2.2) to dissolve recombinant spider silk proteins at relatively high concentrations. It should be mentioned that a major obstacle with artificial spider silk proteins is having an effective means for solubilizing a sufficiently concentrated spinning dope for wet-spinning. 100% HFIP has been used to dissolve recombinant MA silk (MaSp1, MaSp2, and ADF3) (53,68,69,72-74,84,87), recombinant Flag silk (53), and recombinant cylindriform/tubiliform silk (TuSp1) proteins (70). Aside from using an organic solvent, aqueous solutions such as phosphate buffered

saline (66) and urea (160 mM and 1 M) (83) have been used to dissolve recombinant MA-based proteins.

Table 2.2 Summary of recombinant spider silk spinning dope content, spinning dope concentration, and wet-spinning methods/parameters previously used.

Recombinant protein	Spinning dope concentration (w/v %)	Spinning dope content	Spinning parameters	Spinning speed	Coagulation bath	Post-spin stretching bath	Reference
1E (GPG-rich)1Ala8	56	Protein dissolved in HFIP for 48 h	Extruded through a 10 cm long PEEK tube (inner diameter: 0.01 inch)	0.5 mm/min using a fibre spinning machine made by DACA Instruments	100% IPA	IPA, EtOH, MeOH, 1.2 M $(NH_4)_2SO_4$ and dH_2O mixtures; AS fibres soluble in H_2O	(68)
2E (GPG-rich)2Ala8	56						
3E (GPG rich)3Ala8	56						
G (GGX-rich)	15	Protein dissolved in HFIP with 5% toluene for 2-4 days	Extruded through a PEEK tube (inner diameter: 0.005 inch)	0.5 mm/min using a fibre spinning machine made by DACA Instruments	100% IPA	80% IPA and 20% dH_2O; fibres soluble in H_2O	(53)
GY (GGX and GPGGX-rich)	15						
GF (GGX-rich and spacer motifs)	15						
GFY (GGX, GPGGX-rich and spacer motifs)	15						
16 mer	20	Protein dissolved in HFIP	Extruded through a 26 gauge syringe needle	1-2 mL/h	90% MeOH	90% MeOH?	(74)
32 mer	20						
48 mer	20						
64 mer	20						
80 mer	20						
96 mer	20						
1XC	20	Protein dissolved in HFIP overnight	Extruded through a 26 gauge needle (inner diameter: 0.005 inch)	15 µL/min	95% IPA	75% IPA	(70)
1X	20						
ECP-2C	20						
(A1S8)20	26–27	Protein dissolved in HFIP	Extruded through a 10 cm long PEEK tube(inner diameter: 0.01 inch)	0.5 mm/min using a fibre spinning machine made by DACA Instruments	90% IPA	Step 1: 90% IPA; step 2: 90% IPA and then soaked in dH_2O	(72)
(Y1S8)20	26–27						
11RPC	8-10	Protein dissolved in HFIP	Extruded using a home-made spinning apparatus	0.2 mL/h	100 mM $ZnCl_2$ and 1 mM $FeCl_3$ in dH_2O	50–70% EtOH	(71)

Recombinant protein	Spinning dope concentration (w/v %)	Spinning dope content	Spinning parameters	Spinning speed	Coagulation bath	Post-spin stretching bath	Reference
NcDS	20-25	1 M urea	Extruded through a 6 cm long PEEK tube (innner diameter: 0.005 inch)	2-10 µL/min using a Harvard Apparatus Infusion/ Withdrawal Pump	MeOH and H_2O	Not done	(83)
$[(SPI)_4/(SpII)_1]_4$	6.5-12.5	160 mM urea					
$[(SPI)_4/(SpII)_1]_4$	10-18	160 mM urea, 10 or 100 mM glycine					
ADF3	10-28	Protein dissolved in phosphate buffered saline	Extruded through 6-cm-long PEEK tube (inner diameter: 0.005-inch)	2-10 µL/min	80% MeOH and 20% dH_2O	Step 1: Stretch 2x coagulation bath; step 2: soaked in dH_2O	(66)
$(MaSp1)_{16}$	30	Protein dissolved in HFIP	Extruded through a PEEK tube (inner diameter: 0.005 inch)	0.7 mm/min (only 2-3 m of fibres could be collected without breakage)	100% IPA	Stretched 3x in 75% IPA; fibres soluble in H_2O	(69)
$(MaSp1)_{24}$	30						
$(AQ)_{12}$	CSD[a]: 10-17	Protein dissolved in 6 M guanidinium thiocyanate and dialyzed	Extruded through a syringe needle (inner diameter: 0.03 mm)	5 µL/min	90% IPA	90% IPA	(20)
$(AQ)_{24}$	CSD: 10-17						
$(AQ)_{12}$NR3	CSD: 10-17 BSD[b]: 10-15						
$(AQ)_{24}$NR3	CSD: 10-17 BSD: 10-15						
N1L$(AQ)_{12}$	CSD: 10-17						
N1L$(AQ)_{24}$	CSD: 10-17						
N1L$(AQ)_{12}$ NR3	CSD: 10-17 BSD: 10-15						
N1L$(AQ)_{24}$ NR3	CSD: 10-17 BSD: 10-15						
rMaSp1 and rMaSp2	12	Protein dissolved, sonicated, and then heated in micro-wave for 5 sec intervals	Extruded through a PEEK tube (inner diameter: 0.005 inch)	0.5 mm/min using a fibre spinning machine made by DACA Instruments	100% IPA	Step 1: stretch in 80% IPA; step 2: stretch in 20% IPA	(81)

[a] "Classical" spinning dope.
[b] "Biomimetic" spinning dope.

Other solvent systems have also been used to produce spinning dopes of regenerated *Bombyx* spp. silkworm silk fibroin for wet-spinning (88-91). Silkworms have two silk proteins known as sericin (glue-like protein), which allows for composite fibres to hold the cocoon case for protection of the silkworms, and fibroin, which acts as the structural component to the fibres (92,93). Regenerated silk fibroin is produced by removal of sericin (termed

"degumming") to obtain isolated fibroin (3,92). Regenerated *Bombyx* spp. silkworm silk fibroin have been dissolved in 9 M lithium bromide aqueous solution (88); phosphoric acid (89); phosphoric acid/formic acid mixtures (90); hexafluoroacetone (HFA) (91); and, various organic solvents including dimethyl sulfoxide, dimethylformamide, and dimethylacetamide combined with *N*-methylmorpholine-*N*-oxide (NMMO) (94).

Even though many solvents have been successfully used to make spinning dopes for wet-spinning, each silk protein source (whether from a spider or silkworm) will behave differently because of the inherent differences in primary structure. Beyond protein compatibility, each solvent type also has distinct advantages and disadvantages that should be considered. Organic salts can be easily regenerated after use, but often require high temperatures (>100 °C) to dissolve proteins, which results in degradation (94). Conversely, inorganic salts do not require high temperature, but require long dialysis times for their removal, again resulting in degradation (91). Acids are also commonly used for dissolving regenerated silk fibroin, but degradation is again a drawback because of perturbation and attacking of peptide bonds (89,95). However, this can be avoided if wet-spinning is carried out shortly after dissolving the protein. Fluorinated organic solvents such as HFIP and HFA, which are potent hydrogen bond disruptors, have been reported to cause no measurable degradation to recombinant spider silk proteins (81). Although fluorinated organic solvents can be costly, this can be justified if sufficiently high spinning dope concentrations can be reached, resulting in a lower amount of dope required per unit mass of fibrous material produced.

As previously mentioned, recombinant wrapping silk protein constructs with varying numbers of W units have been produced in *E. coli*. Recombinant W_2, W_3, and W_4 protein constructs were demonstrated to be capable of forming silk-like fibres of multi-centimeter

length when manually drawn from a low-concentration (~0.04% w/v) buffered aqueous solution (21). However, a low-concentration spinning dope is not optimal for efficient production of fibres and cannot be applied to wet-spinning (described in the next section). In addition, increasing the concentration of these aqueous solutions tend to lead to non-productive aggregates (Xu and colleagues, unpublished). For these reasons, a new spinning dope with significantly higher concentration needed to be formulated.

2.1.3 Wet-Spinning of Silk Proteins

A number of methods involved in spinning silks from a dope solution have been employed. Electrospinning, a method that generates electrical charges to spin fibres, has been used on regenerated MA silk proteins (96,97) and also recombinant MA silk proteins (98-100). Another method that has been employed is the use of microfluidic devices for elongational flow (rather than shearing flow) to allow for changes in pH and ion gradient, essentially acting as a mimic of the MA gland. Rammensee and colleagues (101) applied elongational flow on MaSp2 analogues, where a microfluidic device was used to allow for a drop in pH from 7.0 to 6.0, simultaneously increasing potassium concentration. However, since then, no more studies of this kind have been reported. Wet-spinning methods have also been extensively employed, and this work focused on using a wet-spinning method; each stage of the wet-spinning process and the permutations that exist in the literature are therefore described in detail.

2.1.3.1 Dehydration (Coagulation) Bath

Once the protein is solubilized in an adequately concentrated spinning dope, wet-spinning in a coagulation bath is a common method used to spin the silk protein into a fibre (Table 2.2). As mentioned above, most of what we know today about the spider spinning

process is based on the processing machinery of MA spidroins from the MA gland (15,102). This machinery involves an intricate combination of pH and ion change in gradient from the spinning gland (where the spinning dope is produced) to the spinning duct leading into to spinneret(s)/spigot(s) for fibre formation. This process fundamentally dehydrates the spidroin to "shock" it out of solution and promote self-assembly of the protein molecules into a solid fibre (15,102). Although the spinning apparatus is likely different in the aciniform gland, based on the very different anatomical features of the gland (2,5,8,9), the involvement of dehydration as a key aspect of fibre formation in the MA gland implies that this may also be involved in aciniform silk fibre formation.

Following this rationale, the wet-spinning method subjects a spinning dope to shear force followed by extrusion into a coagulation bath, serving to amalgamate the protein in a solid fibre (just like the spider). Typically, either isopropyl alcohol (IPA) or methanol (MeOH) are used as dehydrating solvents (Table 2.2). The fibre thus induced (referred to as "as-spun (AS)" at this stage) may then be wound onto a spool/collector. Although several recombinant spider silk proteins, including MA silk proteins (MaSp1, MaSp2, and ADF3) (20,53,68,69,72,74,83,87), Flag silk proteins (53), and TuSp1 silk proteins (70) have been spun into fibres using a wet-spinning method, wet-spinning of wrapping silk has not been previously reported.

2.1.3.2 Post-Spin Stretching Treatments

To further promote molecular alignment within AS fibres, a post-spin stretching treatment is typically performed. As the name implies, this is simply carried out by stretching the AS fibres in a solvent (referred to as "post-spun (PS)" fibres after this point). This step is usually used to promote favourable structural changes within the fibre that lead to changes in mechanical properties such as strength, extensibility, and toughness (20,68-70,73,90,103,104).

Just like the wet-spinning method, the rationale of the post-spin stretching treatment method is based on what we know about the MA spinning gland. The spinning duct is designed to allow for elongational flow (and/or mechanical drawing) of the β-sheet crystals and/or micelle spheroids (henceforth simply referred to as spheroids) converging into an endpoint, the spinneret(s)/spigots (9,102). Fundamentally, the theory is that elongational flow allows for increased velocity with a simultaneous increase in shearing forces to unfold the protein structures. This promotes alignment within the spheroids and results in self-assembly into fibrillar precursors for fibre formation (102). This idea has been consistently demonstrated with silk in many studies using small angle X-ray scattering and atomic force microscopy (AFM) (105-107), confocal scanning light microscopy and electron microscopy (108), as well as solid-state nuclear magnetic resonance spectroscopy (109).

Instead of elongational flow (and/or mechanical drawing), shearing flow is used with wet-spinning. With shearing flow, both the velocity and shearing forces are constant. Because of this, it is likely that unfolding of the protein structures cannot occur and that alignment is hindered resulting in aggregation of the spheroids into a solid fibre-like material (102). This is why stretching of the AS fibres is a necessary step to further promote molecular alignment. Typically, the post-spin stretching bath is composed of a mixture of organic solvent and water, with water being the functional component that improves fibre properties (68-70,73,90,103,104). In most cases, organic solvent is added because many AS silk-based fibres cannot withstand water penetration without being dissolved. In order to address this issue, a two-step post-spin stretching treatment is often employed, with the first step using an organic solvent/water mixture followed by a second step in pure water (Table 2.2).

2.2 Materials and Methods

2.2.1 Protein Expression and Purification

The protein expression and purification protocols were based on those reported by Xu and colleagues (21), with some modifications. Briefly, the pEHU-W_3 expression plasmid was transformed into BL21(DE3) *E. coli* (Novagen, Darmstadt, Germany). Luria-Bertani (LB) medium was prepared (Fisher Scientific; Ottawa, ON), and a starter culture was formed by inoculating a single colony of cells in LB medium containing 50 μg/mL ampicillin (Fisher Scientific; Ottawa, ON), which was incubated with a shaker at 37 °C overnight. The resulting overnight culture was stored at 4 °C for 6 h and transferred into 1.6 L LB medium containing 50 μg/mL ampicillin. The cells were allowed to incubate with shaking at 37 °C until the optical density at 600 nm (OD_{600}) reached 0.8-0.1. Subsequently, expression of the fusion protein was induced with 0.8 mM isopropyl β-D-1-thiogalactopyranoside (IPTG; Fisher Scientific; Ottawa, ON) and incubated with shaking at room temperature (22±2 °C) overnight. Cells were then harvested by centrifuging at 7000 rcf for 5 min at 4 °C. The supernatant was discarded and the pellet resuspended by vortexing in native lysis buffer (50 mM NaH_2PO_4, 300 mM NaCl, 10 mM imidazole, pH 8.0). A French pressure cell press (American Instrument Company; Maryland, USA) was used to lyse the cells. The resulting cell lysate was centrifuged at 12,000 rcf for 30 min at 4 °C to discard insoluble debris.

Subsequently, the supernatant was loaded under non-denaturing conditions onto a column of immobilized Ni-NTA Sepharose (Qiagen, Germany), and passed through the column two times at room temperature. As per the manufacturer's instructions, the column was then washed using a wash buffer (50 mM NaH_2PO_4, 300 mM NaCl, 20 mM imidazole, pH 8.0) and then the bound recombinant proteins with a H_6-SUMO protein tag were eluted using elution buffer (50 mM NaH_2PO_4, 300 mM NaCl, 250 mM imidazole, pH 8.0).

A pEDHC plasmid comprising H_6-SUMO protease gene was kindly provided by the laboratory of Dr. Paul Xiang-Qin Liu. This plasmid was transformed into *E. coli* BL21(DE3), expressed, and purified in-house (Nigel Chapman, M.Sc.) by nickel bead affinity chromatography. Using this protease, a digestion reaction containing 100:1 SUMO protease:elution mixture (w/w) and 1 mM dithiothreitol (Fisher Scientific; Ottawa, ON) was initially carried out on ice for 1 h to cleave the H_6-SUMO tag. The reaction was allowed to proceed further by dialyzing against 50 mM K_3PO_4 (pH 7.5) using a regenerated cellulose dialysis tube (Fisher Scientific; Ottawa, ON) with a pore size of 3.5 kDa. This was incubated with stirring of the dialyzate at 4 ˚C overnight.

After overnight incubation, reverse purification was performed by passing the reaction mixture through another column with immobilized Ni-NTA Sepharose. This allowed the tag-free recombinant protein to flow through the column, while all the other remaining proteins were left bound to the column. The same mixture was passed through the column five times. Initially, this mixture was dialyzed against distilled water (dH_2O) for 3 h at 4 ˚C, with replacement of dH_2O 2-3 times before allowing to incubate with a magnetic stirrer at 4 ˚C overnight. On the next day, dH_2O was replaced 2-3 more times and then lyophilized into dry protein powder, typically yielding 20-40 mg/L culture. A schematic of this process is provided in Figure 2.1.

Protein samples were resolved by sodium dodecyl sulfate-polyacrylamide gel electrophoresis (SDS-PAGE) in 10% acrylamide gels at 180 volt (180V) for 60 min at room temperature. Visualization of gels were done with Coomassie Brilliant Blue R-250. Densitometry was used in concert with Image Lab Software (Bio-Rad Laboratories (Canada) Ltd.; Mississauga, ON) to quantify W_3 protein levels and total protein levels. This, along with

the prestained protein ladder, tetramethylethylenediamine, and reagents for making polyacrylamide gels were purchased from Thermo Scientific (Markham, ON).

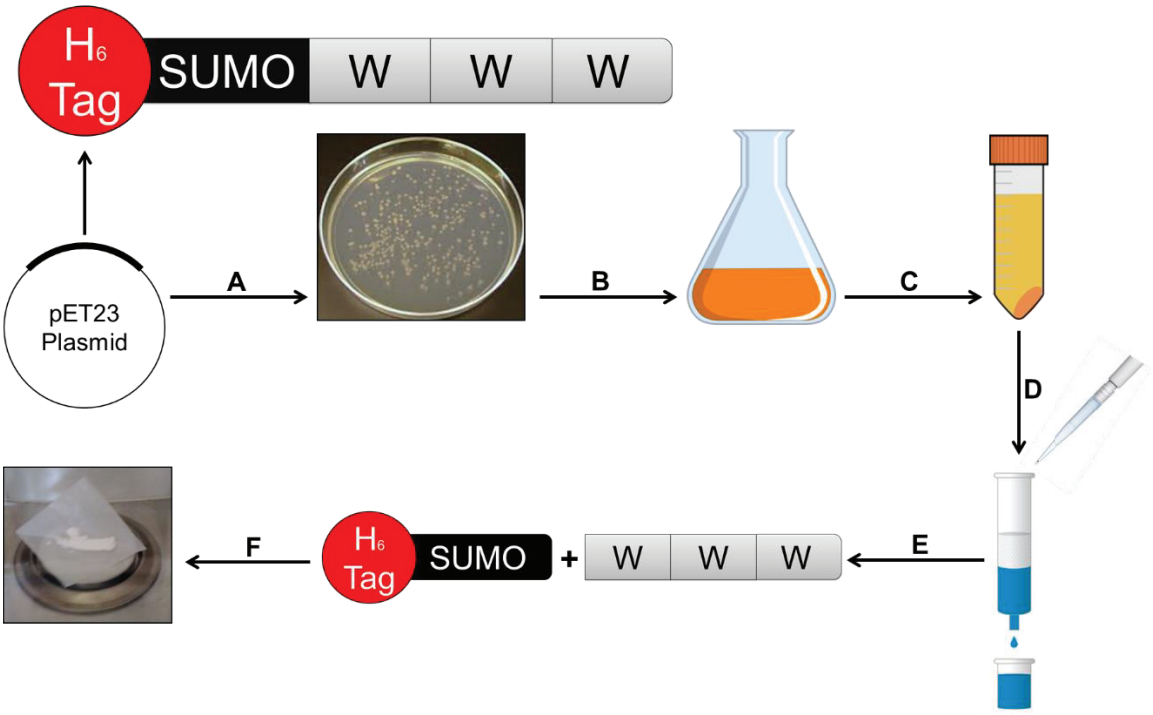

Figure 2.1 Schematic for protein expression and purification of the recombinant W_3 fusion protein. Steps are shown as: BL21(DE3) *E. coli* were transformed with expression plasmid containing the W_3 recombinant gene construct as previously described (21) (A); overnight culture from inoculated cells was transferred, induced with 0.8 M IPTG, and incubated at room temperature overnight (B); cells were harvested by centrifugation and lysed (C); nickel affinity chromatography was employed to purify the fusion protein and eluent was collected (D); SUMO cleavage reaction was carried out and dialyzed overnight against 50 mM K_3PO_4 (E); and, reverse purification by nickel affinity chromatography was carried out to collect purified recombinant W_3 followed by overnight dialysis against dH_2O and then lyophilization (F).

2.2.2 Solubilization of Recombinant Spider Wrapping Silk W_3 Protein

Spinning dopes were made by suspending ~8% (w/v) lyophilized W_3 protein powder into 70% HFIP/30% H_2O (v/v) in glass vials. HFIP (details of purity/class) was obtained from Sigma-Aldrich (Oakville, ON) and H_2O was type I distilled. Suspensions were vortexed

until homogeneous and then sonicated twice at 37 °C for 5 min, with vortexing in between. Subsequently, the glass vials were wrapped with aluminum foil to prevent exposure of the suspensions to light and incubated for ~48 h at room temperature, with occasional vortexing. After 48 h, the suspensions were centrifuged at 18,000 rcf for 30 min at 20 °C and transferred into new glass vials. This was repeated until the suspensions (now spinning dopes) were transparent with no visible insoluble components remaining.

To estimate protein concentration in each spinning dope, 200 μL aliquots were made at a 1/100 dilution and the absorbance of these solutions were measured at 214 nm with an ultraviolet (UV)/Visible (Vis) spectrophotometer (8452A, Hewlett-Packard, Palo Alto, CA) using a quartz cuvette with a path length of 0.05 cm (Hellma, Mülheim, Germany). The Beer-Lambert law could then be used to estimate concentration (c):

$$\mathbf{c} = \frac{\mathbf{A}}{\varepsilon \cdot \mathbf{l}} \quad (1)$$

where l = is the path length of the cuvette (in cm); ε = is the extinction coefficient (in $L \cdot mol^{-1}cm^{-1}$ at 214 nm), calculated for W_3 to be 812,574 $L \cdot mol^{-1}cm^{-1}$ using a script created by Dr. David Langelaan based on the quantitative relationships detailed by Kuipers and Gruppen (110); and A = is the absorbance of the spinning dope at 214 nm. If the estimated concentration was lower than ~8% (w/v), the cap of the glass vial containing the spinning dope was opened to allow evaporation. This was allowed to proceed until the spinning dope reached a final concentration of ~8% (w/v), as determined by repeated absorbance measurement. In no case was the volume allowed to change by more than 10%.

2.2.3 Fibre Formation Using Wet-Spinning

Spinning dope was loaded into a 100 μL Hamilton reversible needle (RN) syringe (Hamilton, Reno NV), which was attached to 6 cm long polyetheretherketone (PEEK) tube

(outer diameter: 1/16 inch; inner diameter: 0.005 inch; Simga-Aldrich; Oakville, ON) by RN compression fittings (1/16 inch; Hamilton; Reno, NV). The syringe containing the spinning dope was securely attached to a KD Scientific model 100 series syringe pump (Holliston, MA). The dope was extruded through the PEEK tube into a coagulation bath of 95% ethanol (EtOH) at a constant speed of 16 μL/min. Fibres formed in the coagulation bath were carefully picked up using tweezers and guided onto a collector, a 50 mL conical centrifuge tube (Fisher Scientific; Ottawa, ON) modified as shown in Figure 2.2. This was attached to a LKB 2232 MicroPerpeX S Pump (GE Healthcare Life Sciences; Mississauga, ON), with the pump set to spin at a constant speed equivalent to the extrusion rate. A schematic of this can be seen in Figure 2.3, while the step-by-step process is shown in detail in Figure 2.4.

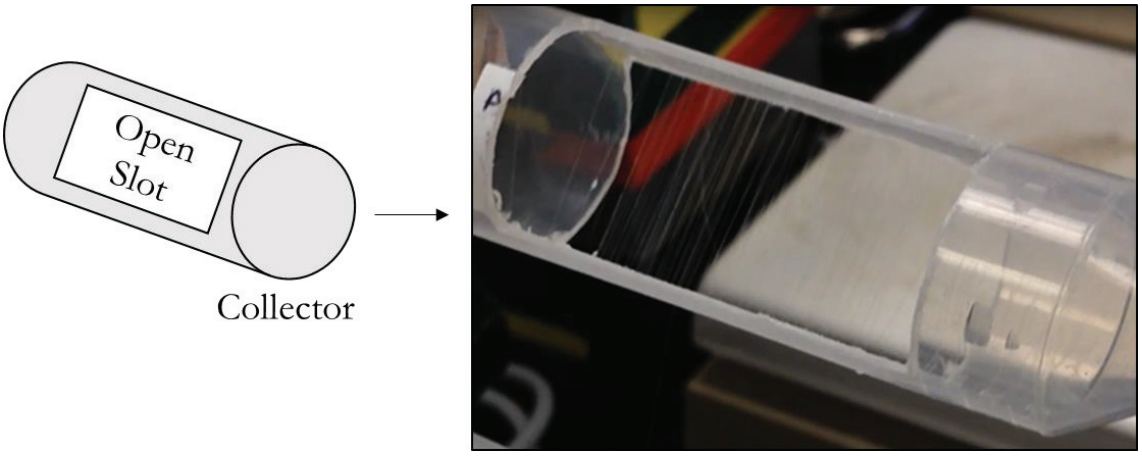

Figure 2.2 Collector employed in the wet-spinning method. A 50 mL conical centrifuge tube was modified by creating an open slot for fibre collection.

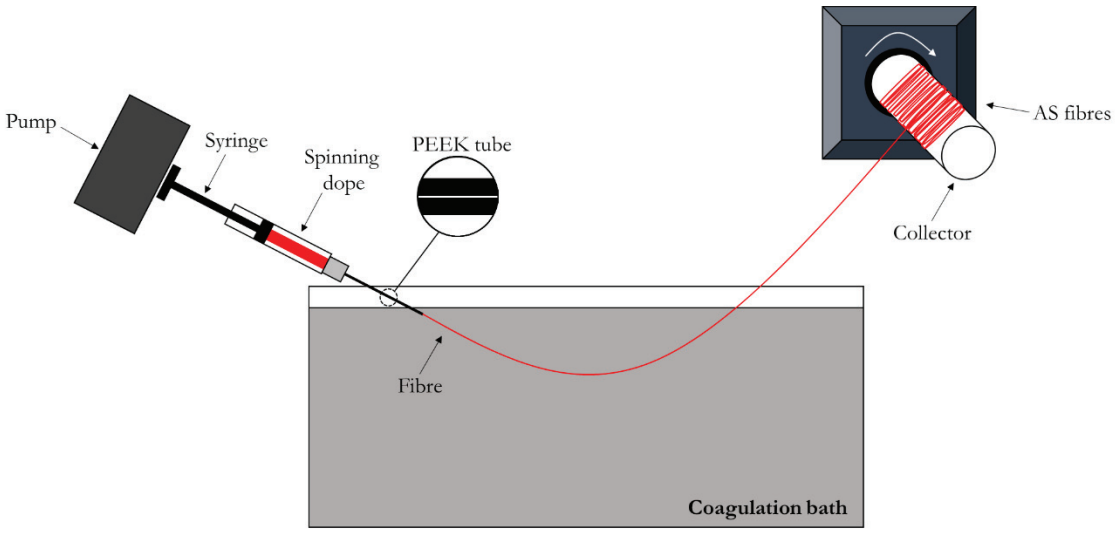

Figure 2.3 Schematic of the wet-spinning fibre production apparatus. This apparatus consists of a pump (providing a controlled extrusion rate), a glass syringe (to store and allow for controlled delivery of the spinning dope), PEEK tubing (for shear force application), a coagulation bath (to amalgamate protein in the soluble dope into an insoluble fibre form), and a collector for the AS fibres.

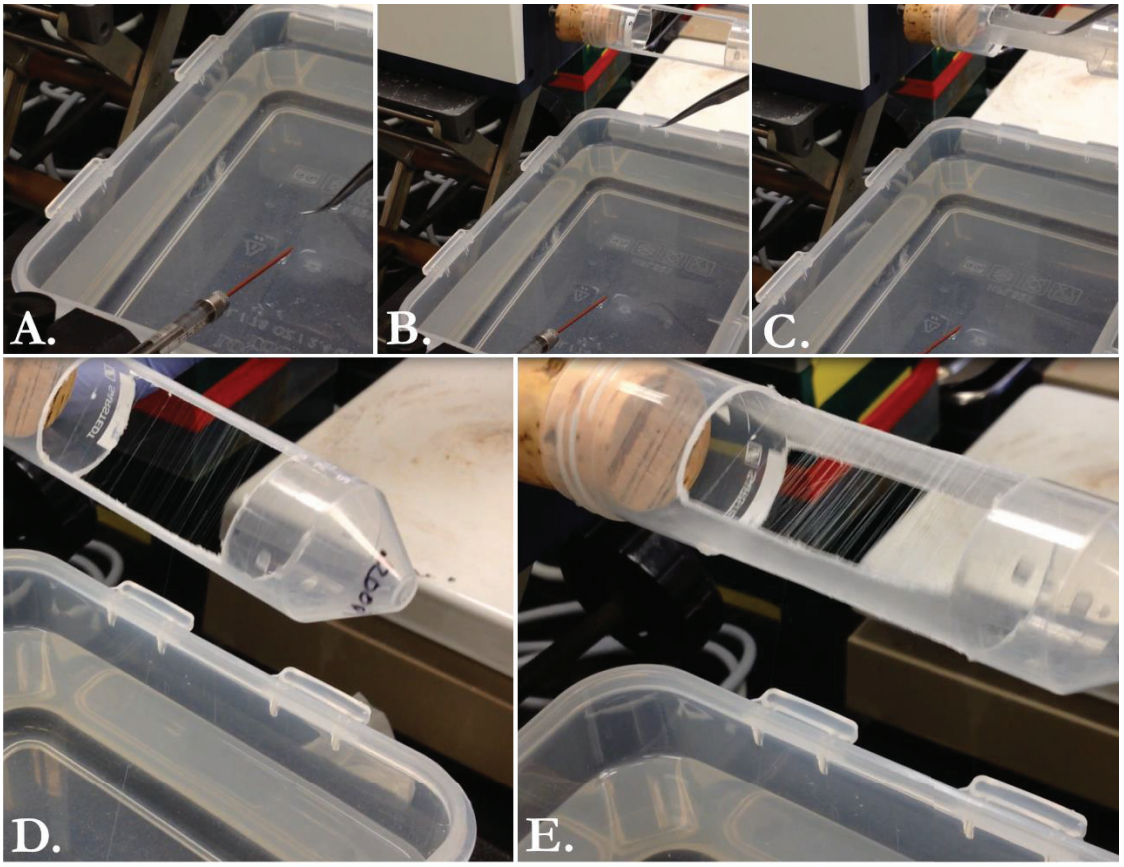

Figure 2.4 Step-by-step depiction of the wet-spinning fibre production method used for recombinant spider wrapping silk protein. The initial transition from the spinning dope into a fibre by shear force-inducing extrusion into a coagulation bath (A), the fibre being carefully guided out of the coagulation bath (B), the fibre being placed on the modified collector (C) allowing continuous collection at a constant speed (D & E).

2.2.4 Post-Spin Stretching Treatment of AS Fibres

Through helpful discussions with Dr. Laurent Kreplak, a custom-designed apparatus was built at the Department of Physics and Atmospheric Science Machine Shop (Dalhousie University; Halifax, NS) to allow consistent stretching of fibres in dH_2O (Figures 2.5 (schematic) and 2.6 (photograph)). This has been effectively applied for post-spin stretching on all fibre conditions. The container material was aluminum, the metric ruler and the bolts were stainless steel, and the single axis translation stage (Thor Labs, 50 mm; Montreal, QC) was anodized aluminum. AS fibre samples were macroscopically examined for defects before

post-spin stretching treatment. 2-3 cm long AS fibre pieces without visible defects were cut and placed at the edge and on top of the translational stage and at the edge and on top of the container mounting surface using Scotch® Double Sided Tape (1/2 inch). Scotch® Magic™ Tape (3/4 inch) was then carefully placed on top to firmly secure both ends of the AS fibres.

Following fibre affixing, the post-spin stretching apparatus was slowly filled with dH_2O until the fibres were fully immersed. Using the control knob, the fibres were smoothly stretched to 4x their original length and allowed to rest in the dH_2O bath for 3 min. The dH_2O bath was then drained while simultaneously misting the surface using 95% EtOH until the fibres were no longer in contact with dH_2O. Subsequently, the resulting "PS-stretched" fibres were allowed to dry at room temperature for 5-10 min.

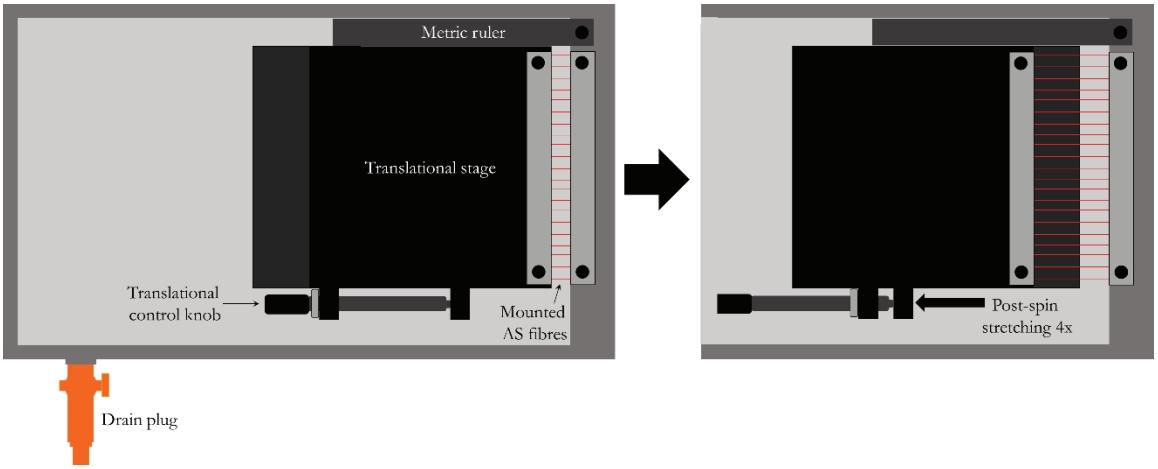

Figure 2.5 Schematic of the controlled post-spin stretching treatment apparatus. Left: fibres are affixed both to the translational stage and the inside edge of the container. The container is then filled with dH_2O, followed by stretching of the fibres with controlled translation of the stage. Right: fibres are left to sit in the dH_2O bath, with subsequent draining of the dH_2O while simultaneously misting the surface in the region of fibre extension with 95% EtOH.

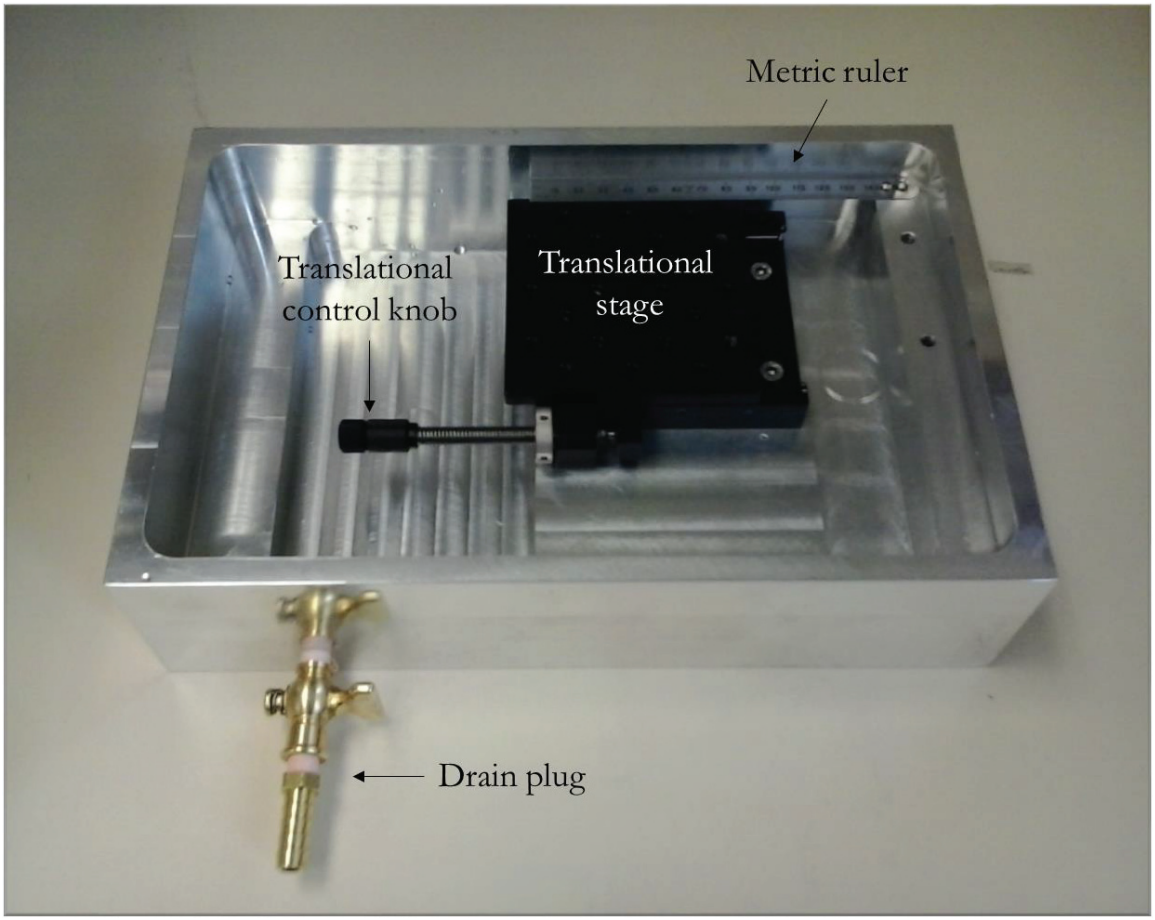

Figure 2.6 A photograph of the post-spin stretching apparatus. The translational control knob allows for controlled motion of the stage, the metric ruler allows for consistent and precise measurement of fibre stretching, and the drain plug allows the dH_2O bath to steadily drain at a controlled rate of flow.

2.2.5 Light Microscopy

AS and PS fibres were placed on a glass slide (Fisher Scientific; Ottawa, ON) and fibre morphology was observed by imaging with a 10X or 40X objective lens coupled with a 10X ocular lens, using a Zeiss Axiovert 200M inverted microscope coupled to an AttoArc2 HBO 100W lamp. Images were taken with a Hamamatsu ORCA-R2 digital camera.

2.3 Results and Discussion

2.3.1 Protein Expression of H_6-SUMO-W_3, Cleavage of H_6-SUMO, and Purification of W_3

The recombinant W_3 fusion protein consisted of three AcSp1 200-aa repetitive units from *Argiope trifasciata* attached to an N-terminally fused H_6-SUMO tag (Figure 2.7), as detailed in section 2.1.1.1. An expression plasmid encoding H_6-SUMO-W_3 was transformed into *E. coli* BL21(DE3) to express the fusion protein. Following IPTG induction and overnight protein expression at room temperature in transformed *E. coli*, cells were harvested by centrifugation and lysed to recover the expressed fusion protein. Subsequent centrifugation of the lysed cells resulted in a protein mixture containing the expressed fusion protein that was passed through a column to permit immobilization by binding of the H_6-tag to the nickel beads, while proteins without a H_6-tag passed through the column and were removed (Figure 2.8). Following bound fusion protein elution from the affinity column, site-specific cleavage at the junction of the H_6-SUMO tag and the fusion partner W_3 was carried out using recombinant SUMO protease. This reaction was allowed to proceed further during overnight dialysis at 4 °C. After overnight dialysis, the resulting dialyzate contained the cleaved H_6-SUMO tag and W_3 protein, which is clearly resolvable by SDS-PAGE analysis with a band at ~15 kDa corresponding to H_6-SUMO tag and a band at ~57.1 kDa corresponding to the W_3 protein without the attached fusion partner (Figure 2.8). No band is visible at ~72.1 kDa demonstrating practically complete cleavage. The dialyzate containing the cleaved H_6-SUMO tag and W_3 protein was then subjected to reverse purification, allowing the W_3 protein to flow through the column, while the H_6-SUMO tag was left bound to the column. To remove salts from the retrieved solubilized W_3 protein, overnight dialysis was carried out. Following dialysis, the dialyzate containing W_3 protein was lyophilized. The

resulting protein powder was either immediately used for solubilization or stored at -80 ˚C, with the latter being avoided when possible. Protein expression levels typically ranged from 20-40 mg/L of LB-medium.

MGHHHHHHGSDSEVNQEAKPEVKPEVKPETHINLKVSDGSSEIFFKIKK
TTPLRRLMEAFAKRQGKEMDSLRFLYDGIRIQADQTPEDLDMEDNDIIE
AHREQIGGAGPQGGFGATGGASAGLISRVANALANTSTLRTVLRTGVSQ
QIASSVVQRAAQSLASTLGVDGNNLARFAVQAVSRLPAGSDTSAYAQAFSS
ALFNAGVLNASNIDTLGSRVLSALLNGVSSAAQGLGINVDSGSVQSDISSSS
SFLSTSSSSASYSQASASSTSGAGYTGPSGPSTGPSGYPGPLGGGAPFGQSGF
GGSAGPQGGFGATGGASAGLISRVANALANTSTLRTVLRTGVSQQIASSV
VQRAAQSLASTLGVDGNNLARFAVQAVSRLPAGSDTSAYAQAFSSALFNAG
VLNASNIDTLGSRVLSALLNGVSSAAQGLGINVDSGSVQSDISSSSSFLSTSSS
SASYSQASASSTSGAGYTGPSGPSTGPSGYPGPLGGGAPFGQSGFGGSAGP
QGGFGATGGASAGLISRVANALANTSTLRTVLRTGVSQQIASSVVQRAAQ
SLASTLGVDGNNLARFAVQAVSRLPAGSDTSAYAQAFSSALFNAGVLNASN
IDTLGSRVLSALLNGVSSAAQGLGINVDSGSVQSDISSSSSFLSTSSSSASYSQ
ASASSTSGAGYTGPSGPSTGPSGYPGPLGGGAPFGQSGFGG

Figure 2.7 Amino acid sequence of H_6-SUMO-W_3. A H_6-SUMO tag (106-aa long; shown in yellow) was added to the N-terminus of W_3, where the first W unit (199-aa long) is shown in black and the second and third W units (each 200-aa long) are shown in blue. The first residue (S) of the second and third W units is shown in red.

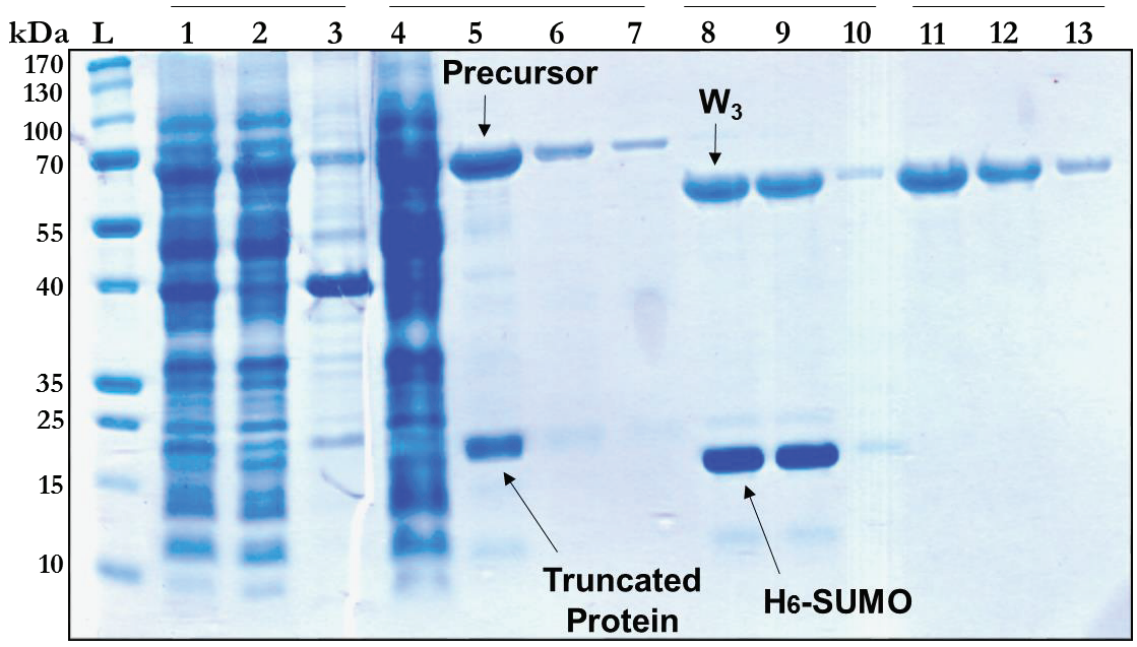

Figure 2.8 Protein expression of H_6-SUMO-W_3, cleavage of H_6-SUMO tag from W_3, and purification of W_3. Key steps in the process was resolved by SDS-PAGE, visualized with Coomassie blue staining. The prestained protein ladder is shown in lane L. Total lysate, supernatant and pellet following protein expression in *E. coli* are represented in lanes 1-3, respectively. After loading the supernatant (i.e., lane 2) onto a column for nickel affinity chromatography, lane 4 shows unattached proteins without H_6-SUMO tag that appear in the flow-through, and lanes 5-7 show the bound recombinant proteins with H_6-SUMO tag that are eluted using 5 mL, 1 mL, and 1 mL of elution buffer containing imidazole, respectively. Lanes 8-10 are total lysate, supernatant and pellet of the elution reaction mixture after SUMO protease digestion and overnight dialysis, respectively. The dialyzate containing the cleaved H_6-SUMO tag and W_3 protein was subjected to reverse purification using nickel affinity chromatography. The same dialyzate mixture was passed through the column five times (lane 11), with subsequent washes each using 2 mL of the same dialysis buffer (lanes 12 and 13), and all showing purified W_3.

2.3.2 Solubilization of W_3 Protein in a Fluorinated Organic Solvent/Water Mixture

Based on the literature precedents detailed above (section 2.1.2), a wide variety of organic solvents alongside the chaotrope urea were tested for the ability to solubilize W_3 (Table 2.3). For this screening step, small volume samples (~10-20 μL) were used. These were subjected to occasional vortexing and incubated at room temperature for 48 h prior to

assessing solubilization by qualitative observation. The criteria for assessing solubilization was based on the presence or absence of visible precipitate. Of all conditions tested, only HFIP/H_2O mixtures appeared promising, as they resulted in the least amount of precipitate visible to the naked eye (Table 2.3). This is in contrast to the fact that 100% HFIP is the most commonly used solvent for recombinant spider silk protein (Table 2.2). It was clear that this solvent by itself could not be applied to the W_3 protein (Table 2.3). Conversely, the use of an HFIP/H_2O mixture for this purpose has never been reported before.

Table 2.3 Dissolving ability of W_3[a] protein using different solvents. Each sample would be occasionally vortexed and allowed to dissolve for up to 48 h at room temperature.

Solvent	Dissolved	Observations
100% HFIP	No	Visible precipitate
80% HFIP/20% H_2O	Partially	Less visible precipitate
50% HFIP/50% H_2O	Partially	Less visible precipitate
100% HFA	No	Visible precipitate
8 M Urea in H_2O	No	Visible precipitate
100% NMMO	No	Visible precipitate
80% NMMO/20% H_2O	No	Visible precipitate
100% Acetone	No	Visible precipitate
80% Acetone/20% H_2O	No	Visible precipitate

[a] The concentration was ~5% (w/v).

To fine-tune the ratio of HFIP/H_2O, a series of tests at different solvent ratios was carried out (Table 2.4) using larger volumes (~40 μL). Beyond the use of a larger volume, a 5 min sonication treatment was added. It was found that sonication suspended the protein more effectively when an optimal HFIP/H_2O mixture was selected. As detailed in Table 2.4, three different classes of behaviour were seen when testing these solvent conditions with HFIP. First, 100% HFIP resulted in protein flakes; second, a mixture of 50% HFIP/50% H_2O resulted in swollen aggregation of the protein; and third, a mixture of 70% HFIP/30% H_2O essentially dissolved all the protein. This latter condition, therefore, was pursued for further optimization of spinning dope properties.

Table 2.4 Optimizing dissolving ability of W_3[a] protein in different concentrations of HFIP.

HFIP (vol.%)	Dissolved	Observations
100%	No	Protein flakes
90%	Partially	Protein flakes with low turbidity solvent
80%	Partially	Protein flakes with high turbidity solvent
70%	Mostly	Small amount of insoluble components with very low turbidity solvent
60%	Partially	Swollen aggregates, low turbidity solvent
50%	Partially	Swollen aggregates

[a] The concentration was ~5% (w/v).

Once a solvent mixture capable of solubilizing W_3 was established, the next consideration was to optimize the concentration of W_3 protein in the dope (Table 2.5). As a control, it was verified that ~5% W_3 (w/v) could be fully dissolved. Conversely, ~15% W_3 (w/v) was too high, resulting in a gel-like sample. Through further optimization, it was found that ~8% W_3 in 70% HFIP/30% H_2O was the most suitable concentration, allowing full dissolution and resulting in a slightly viscous spinning dope, which is ideal (53,68) for a wet-spinning procedure. This solvent was also tested on W_2 and W_4 at concentrations of ~16% (w/v) and ~4% (w/v), respectively. The rationale for using these concentrations was that a smaller protein size would require greater amounts of protein, and a larger size protein would require lesser the amounts of protein. In both cases the proteins would not dissolve, even at half the initially selected concentration, which suggested that beyond molecular size and homologous protein sequence, additional variables were at play, affecting solubility of these proteins.

Table 2.5 Optimizing the concentration of W_3 protein in the selected solvent[a].

W_3 (w/v %)	Dissolved	Observations
5	Yes	Concentration too low (spinning dope not viscous enough)
10	Mostly	Concentration too high (spinning dope too viscous)
15	Mostly	Concentration extremely high (spinning dope gel-like)

[a] 70% HFIP/30% H_2O.

Following optimization of the spinning dope conditions, the last step was to optimise the method of sample preparation. Four different methods were tested, all of which involved initial vortexing to generate homogeneous suspensions, followed by incubation for 24 h with intermittent vortexing. Once homogeneity was achieved, the four methods differed as follows: (1) intermittent vortexing with no sonication; (2) intermittent vortexing and sonication at room temperature for 5 min; (3) intermittent vortexing and sonication at 37 °C for 5 min; and, (4) intermittent vortexing with two rounds of sonication at 37 °C for 5 min (Table 2.6). W_3 concentrations achieved using each of these methods are reported in Table 2.6.

Table 2.6 Optimizing the method used for solubilizing W_3[a].

Method #	UV/Vis absorbance	Concentration
1	0.33875	4.76%
2	0.32254	4.53%
3	0.48631	6.85%
4	0.51392	7.19%

[a]~8% W_3 (w/v) in 70% HFIP/30% H_2O.

It was clear that method 4 provided the most effective dissolving of the W_3 protein, and this method was subsequently modified to include a longer incubation time (48 h) in an attempt to solubilize more protein. It was found that a protein concentration of ~8% was consistently achieved with this modified version of method 4. Any remaining insoluble debris were removed by centrifugation, and any inaccuracies arising from the initial protein weight measurements during dope preparation could be corrected by evaporation of the spinning dope until UV/Vis absorbance corresponded to a protein concentration of ~8% (w/v).

To ensure that no protein degradation occurred in the spinning dope, the effect of incubation time on protein size was followed. It was found that, over 240 h, there was no

significant change in the full-length W_3 protein band relative to the smaller protein bands as resolved by SDS-PAGE (Figure 2.9). This is consistent with other reports using HFIP for solubilization of recombinant silk proteins (81). Furthermore, densitometric analysis revealed an average purity of ~65% for W_3 relative to its smaller length proteins; however, this value is likely underestimating the actual amount of this full-length protein band, and should be taken with the caveat Coomassie Blue dye is known to have different affinities for different types of proteins (111). A slight increase in concentration occurred over 10 days, but this was likely due to unavoidable evaporation of the spinning dope (Figure 2.9) – even though the spinning dope was tightly sealed in a glass vial, evaporation was unavoidable due to repeatedly re-opening the vial to obtain sample aliquots.

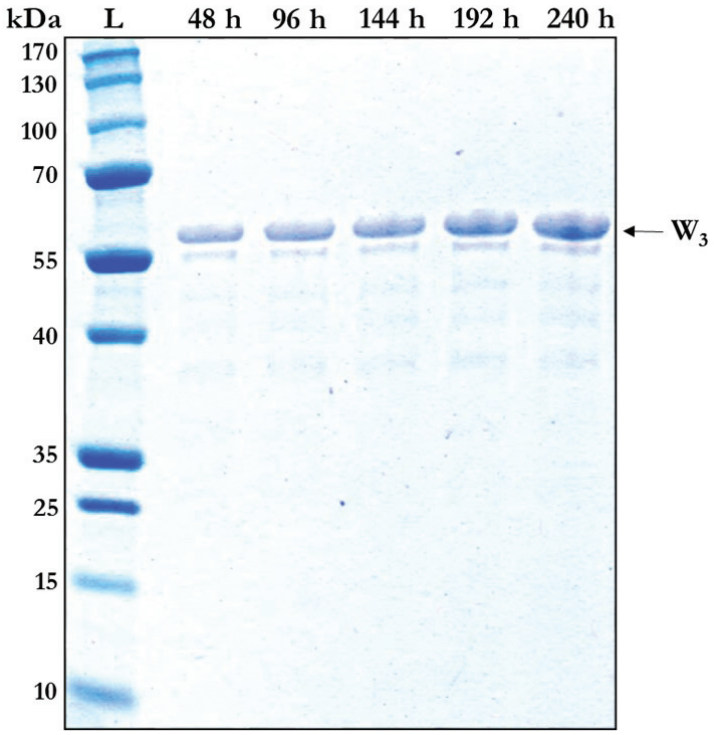

Figure 2.9 Solubilization of recombinant wrapping spider silk W_3 protein resolved by SDS-PAGE and visualized with Coomassie blue staining. The prestained protein ladder is shown in lane L. A series of aliquots was loaded in the subsequent lanes, taken from a spinning dope sample incubated at room temperature at the indicated time-point.

2.3.3 Wet-Spinning Can Be Applied on the W_3 Spinning Dope

Using the newly formulated spinning dope, various conditions were tested to see if this could be applied to a wet-spinning method. The most common dehydration solvents that have been reported for recombinant spider silk proteins are IPA and MeOH (Table 2.2). Because of this, these dehydrating solvents and others were tested with the W_3 spinning dope (Table 2.7). Acetone and dH_2O resulted in aggregate formation or poor fibre formation, respectively. Conversely, it was found that 100% IPA, 100% MeOH, and 95% EtOH all allowed for fibre formation. IPA appeared to be too potent of a coagulation agent, often resulting in aggregation of the spinning dope in the PEEK tubing itself, which made consistent production of fibre infeasible. Conversely, MeOH was not a robust coagulation agent, resulting in fibres that often broke during fibre collection and was, therefore, also not practical for consistent production (Table 2.7). Although these solvents were not efficacious for fibre production, it was found that 95% EtOH, a more environmentally friendly solvent, provided reliable and consistent formation of fibres with sufficient mechanical integrity to be handled throughout the wet-spinning process.

Table 2.7 Screening coagulation bath solvents on W_3[a] using automated wet-spinning.

Solvent	Fibre formation?	Observations
Acetone	No	Aggregate formation
dH_2O	Partially	Extremely thin fibres and breaks often
100% IPA	Yes	Immediate fibre formation
100% MeOH	Yes	Fibre formation, but breaks often
95% EtOH	Yes	Fibre formation

[a] These tests were initially done with ~5% W_3 (w/v) in 70% HFIP/30% H_2O.

Numerous ratios of EtOH and H_2O were tested to qualitatively observe what worked best, and also to examine how much dehydration was needed for fibre formation (Table 2.8). It was found that there was no discernible change in fibre production between

the ranges of 85-95% EtOH. However, when there was too much H_2O present, it was found that the fibres were extremely thin and broke often (Table 2.8). In addition to shearing forces initiated by the PEEK tube, it therefore appears that a range of 85-95% EtOH likely facilitates an appropriate structural transition and amalgamation of the protein molecules into a solid fibre. The resulting AS fibres using this optimized wet-spinning method were observed by light microscopy (Figure 2.10).

Table 2.8 Optimizing the coagulation bath alcohol/water solutions with W_3[a] using automated wet-spinning.

EtOH concentration (vol.%)	Fibre formation?	Observations
95	Yes	Fibre formation
90	Yes	Fibre formation
85	Yes	Fibre formation
80	Partially	Thin fibres and breaks
60	Partially	Extremely thin fibres and breaks often
0	Partially	Extremely thin fibres and breaks often

[a] These tests were done with ~8% W_3 (w/v) in 70% HFIP/30% H_2O.

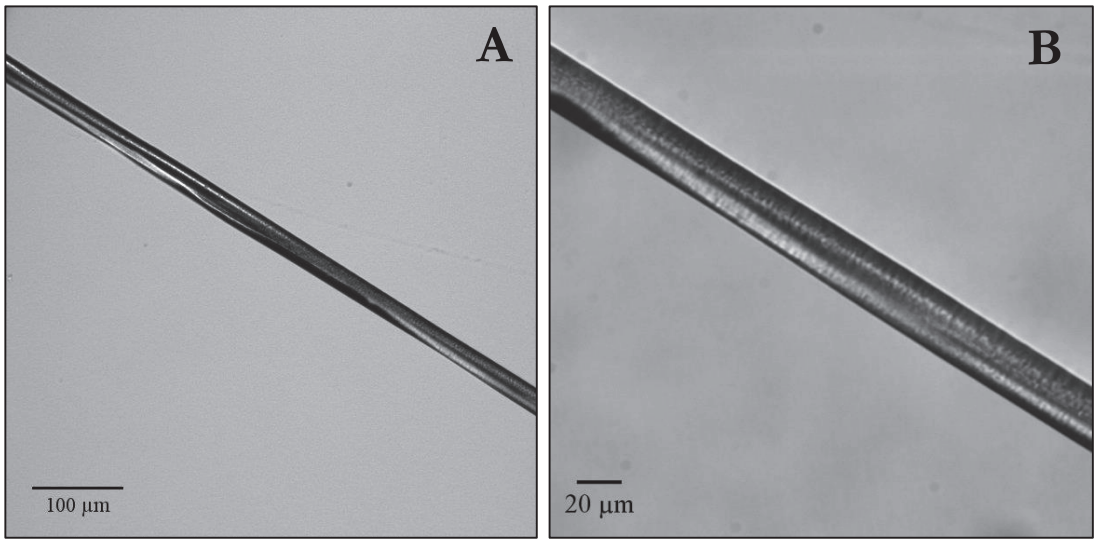

Figure 2.10 Light microscope images of representative AS fibres formed from wet-spinning. Images were taken at both (A) 100X magnification and (B) 400X magnification.

2.3.4 Post-Spin Stretching of AS W_3 Fibres to Promote an Increase in Molecular Alignment and Improvements in Mechanical Properties

A post-spin stretching step in dH_2O (Figure 2.6) was carried out in an attempt to promote favourable structural changes that typically give rise to improvements in mechanical properties, such as strength, extensibility, and toughness (68-70,73,90,103,104). Most studies on post-spin stretching silk-based fibres have reported doing this manually with the use of forceps or tweezers (53,68,69,72,74); however, in order to overcome errors associated with hand pulling, a straightforward post-spin stretching apparatus was used (Figure 2.6), making this process more reliable and consistent.

As mentioned before, in most cases, organic solvent is added because many other AS silk-based fibres cannot withstand H_2O penetration without being dissolved (Table 2.2). In order to address this issue, a two-step post-spin stretching procedure is often incorporated with the first step in an organic solvent/H_2O mixture followed by pure H_2O (Table 2.2). The rationale for employing the second step is that H_2O seems to be the major functional component that improves fibre mechanical properties (68-70,73,90,103,104). Interestingly, it was found that the W_3 AS fibres are not dissolved by H_2O and can, therefore, be directly stretched in an H_2O bath up to six times (6x) their original length with the majority (~80%) of fibres being readily stretched in H_2O without breaking. However, after optimization, it was found that fibres were more uniform in morphology and diameter following stretching to four times (4x) their original length. Notably, the post-spin stretching step results in fibres that are more uniform in morphology (Figure 2.11) when compared to AS fibres (Figure 2.10).

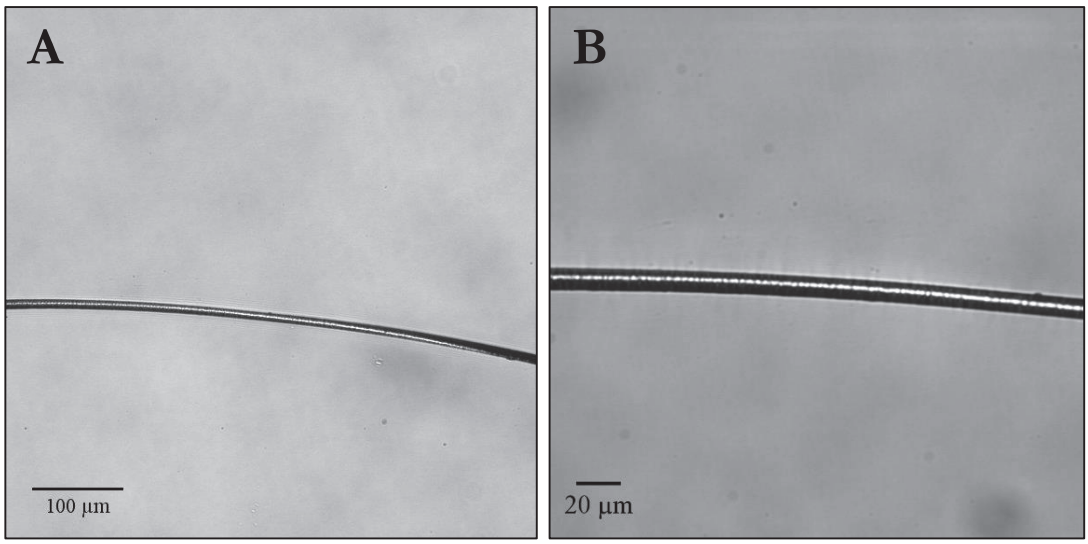

Figure 2.11 Light microscope images of representative PS 4x fibres formed from wet-spinning. Images were taken at both (A) 100X magnification and (B) 400X magnification.

2.4 Summary

Recombinantly produced wrapping silk W_3 proteins were successfully solubilized at ~8% (w/v) in 70% HFIP/30% H_2O and fibres were artificially produced using a wet-spinning method. The optimal solvent mixture found to solubilize the protein as a spinning dope (70% HFIP/30% H_2O), the coagulation bath (95% EtOH/5% H_2O), and the post-spin stretching bath (H_2O) all differ from the conditions previously reported for other recombinant spider silk proteins (Table 2.2). Mechanical properties, molecular alignment, and changes in structural conformations can only be determined through mechanical testing and biophysical characterization. In parallel with the work detailed above, Dr. Lingling Xu discovered another solvent mixture (60% trifluoroacetic acid (TFA)/20% 2,2,2-trifluoroethanol (TFE)/20% H_2O) that could solubilize W_3 at ~10% (w/v) and was amenable to artificial production of fibres using the same wet-spinning method. Comparative characterization of biophysical, mechanical, and morphological properties was carried out for both spinning dopes and fibres, as detailed in Chapter 3.

Chapter 3: Characterization of Biophysical, Mechanical, and Morphological Properties of New Protein-Based Nanomaterials from Recombinant Spider Wrapping Silk Fibres

3.1 Introduction

In Chapter 2, I explained the process and development of a wet-spinning method for the artificial fabrication of recombinant wrapping silk proteins into silk-like fibres. These fibres were then treated with a post-spin stretching method, resulting in thinner and more homogeneous fibres. Based upon literature precedents for other materials, my hypothesis was that this post-spin stretching treatment would facilitate additional molecular alignment of protein secondary structure within the fibres, resulting in improved mechanical properties. To test whether these anticipated changes and improvements occurred, I used various characterization techniques as detailed in this chapter. Prior to detailing the results, background required to understand each characterization technique is provided.

3.1.1 Circular Dichroism (CD) Spectroscopy

CD spectroscopy in the far-ultraviolet (far-UV) regime is a common technique used to evaluate the overall secondary structure of proteins. In almost all cases, spectra for proteins are acquired when they are in the solution-state compared to when they are in solid-state (112,113). Briefly put, this technique probes protein secondary structure by quantifying the difference in absorbance, ΔA, of left-handed vs. right-handed circularly polarized light. The peptide bonds in a polypeptide exhibit differences in this ΔA as a function of their

secondary structure (112,114,115). This is due to differences in dipolar interactions between neighbouring peptide bond chromophores for different secondary structuring, leading to characteristic far-UV CD spectra for each type of secondary structure (114,115). For example, it is known that CD spectra for proteins with α-helical structure results in three major bands, one positive band at 193 nm, and two negative bands at 222 nm and 208 nm (112). In contrast, CD spectra for proteins with predominantly β-stand/sheet structure show one positive band at 195 nm and one negative band at 218 nm (112). For proteins with random-coil or disordered structure, CD spectra show one positive band at 210 nm and one negative band near 195 nm (112). Because the total ΔA at each wavelength is given by the sum of contributions from each type of secondary structure as a function of relative proportion in the sample, in a linear combination, far-UV CD spectra provide quantitative information on the secondary structuring of proteins. In the case of recombinant spider silk, being able to readily characterize the overall protein secondary structure allows for rapid determination of whether the recombinant spider silk is similar in structure to its native counterpart. This also provides the means to rapidly test for perturbations as a function of conditions, such as changes to the spinning dope composition or protein concentration.

3.1.2 Mechanical Testing

Mechanical testing is an essential method for materials characterization. The behaviour of materials, such as ceramics, metals, or polymers, upon subjection to mechanical force (or load) is monitored, allowing determination of mechanical properties of a material in question (116). The mechanical behaviour of each material is related to its response to the applied force, which is known as deformation (116). Information on deformation can be represented in a stress-strain curve, revealing many mechanical features (Figure 3.1). The key features are stress, strain, toughness, and elastic modulus (Young's modulus). It should be

noted that, stress and strain are used interchangeably with strength and extensibility, respectively. Either true values or engineering values can be calculated on the basis of a stress-strain curve. True values take into account the actual change in cross-sectional area of the material as force is applied, whereas engineering values are based upon the cross-sectional area of the material before force is applied (116). For the purposes of this work, engineering values were obtained and will therefore be detailed further.

Engineering stress is the maximum level of stress (σ) a material can withstand before reaching its breaking point and is derived from the maximum applied force (F) over the original cross-sectional area of the material (A_o) (most often reported in MPa) (116). Engineering strain is the maximum level of strain (ε) a material can withstand before reaching its breaking point, which is the change in length until breaking (ΔL) over the original length (L_o) (expressed as mm/mm or %) (116). Toughness is the total amount of energy input required to reach the breaking point, and is represented by the area under the stress-strain curve (expressed as $MJ \cdot m^{-3}$) (116). Finally, the Young's modulus is the resistance to deformation, represented by the slope of the stress-strain curve before the yield point (Figure 3.1; the point where permanent deformation begins) (most often reported in GPa) (116).

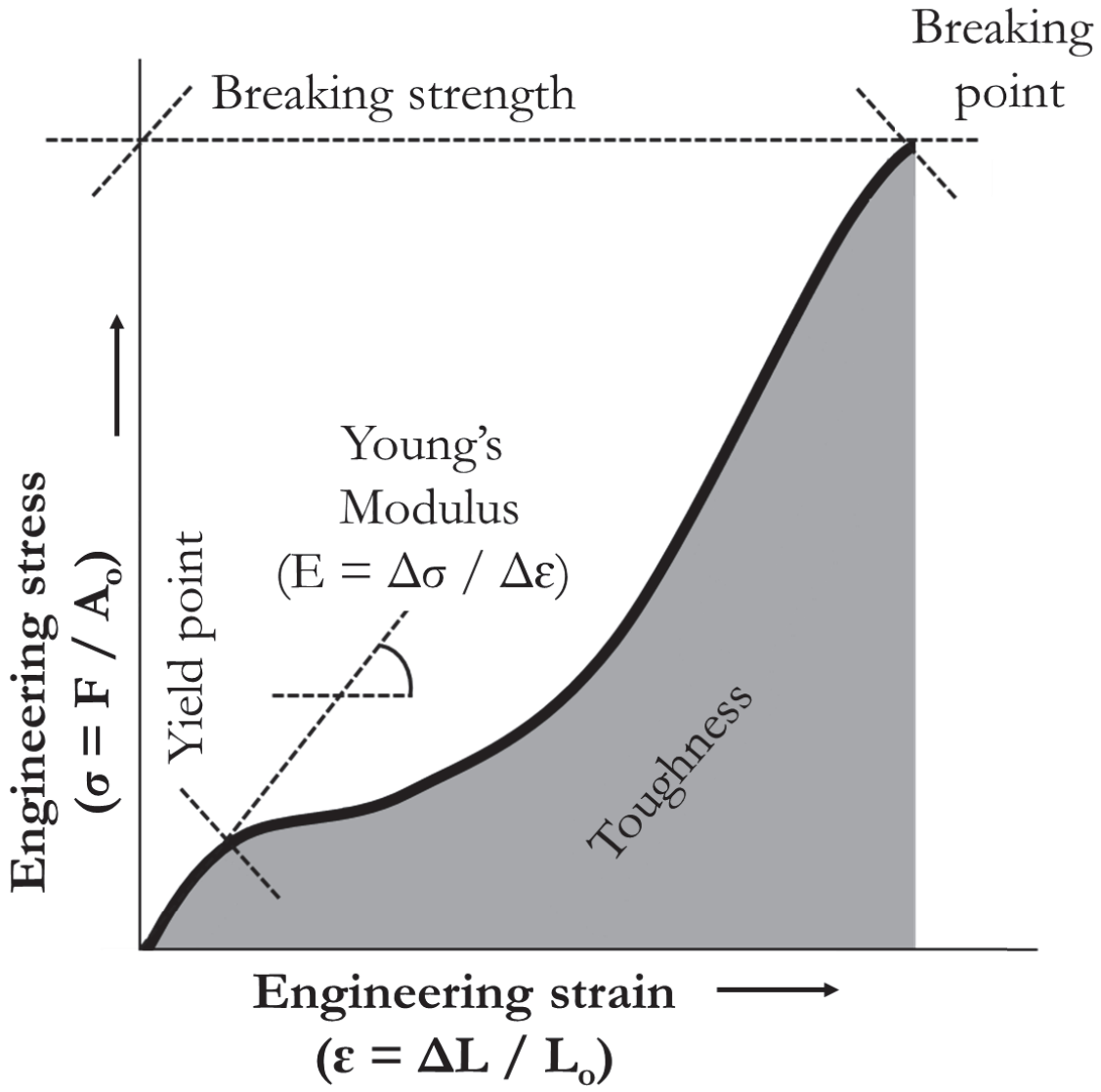

Figure 3.1 Typical stress-strain curve for silk-based materials showing mechanical properties determined for this work. The slope of the linear deformation before the yield point, the point where permanent deformation begins, is the Young's modulus. The breaking point allows for calculation of both breaking strength (stress) and extensibility (strain). Toughness is calculated as the total area under the stress-stain curve. This figure was adapted from Vollrath and Knight (9).

3.1.3 Polarized Light Microscopy

Polarized light microscopy can be used to both qualitatively observe and quantitatively measure birefringence in materials. Birefringent materials have some form of

molecular orientation and are thus optically anisotropic in nature (117). As a result, when observed using a polarizing microscope, these optically anisotropic samples appear illuminated because of their birefringence (117). In this instance, plane polarized light is employed. A pair of polarizing filters (or polarizers) can be used with a light microscope, with one polarizer being placed in the optical path to the sample and another, known as the analyzer, between the sample and the eyepiece (117). In principle, this method works by linearly polarizing light in one plane in the optical path to the sample; the light traveling from the sample is then filtered by a filter rotated at 90° (this is known as "crossing" of the polarizing filters), essentially resulting in a background with no light (117). The incident linearly polarized light can be considered as a linear combination of left and right circularly light with equal intensity and phase. In the case of an optically anisotropic sample, differences in interaction with the left vs. right circularly polarized components lead to elliptically polarized light. This, in turn, will have some component at 90° to the incident linearly polarization, allowing transmission of light through the orthogonal polarizer and, hence, observation of birefringence (117). On this basis, polarized light microscopy is a useful tool for measuring overall molecular orientation in silk-based materials (88,118-120).

3.1.4 Raman Spectroscopy

3.1.4.1 Raman Spectroscopy/Spectromicroscopy for Determining Conformational Changes in Protein Secondary Structure

Raman spectroscopy is a method with conformational-sensitivity to protein secondary structure. In particular, monitoring of Raman active vibrational stretching modes of peptide bonds is employed for this purpose (8,121,122). One of the first studies to examine conformational changes in silk microfilaments using Raman spectroscopy examined

silkworm silk from *B. mori* (123). Shortly afterward, Raman spectroscopy techniques began to evolve, with Gillespie and colleagues (124) employing the first polarized Raman spectra on silkworm silk from *B. mori* and MA silk from *N. clavipes*. Since that time, Raman spectroscopy has been used extensively to study conformational changes in secondary structure in both silkworm silk (88,103,122,124,125) and spider silk (87,99,104,124-126).

Moving beyond conventional Raman spectroscopy, spectromicroscopy may be carried out where this technique is coupled to an optical microscope through use of visible light laser(s) excitation source(s) to acquire spatially-dependent spectroscopic information. One key advantage of Raman vibrational spectromicroscopy over conventional Raman spectroscopy is that the signal-to-noise ratio of vibrational stretching within the protein is enhanced (121). Other advantages of this technique over conventional Raman spectroscopy include the ability to carry out non-invasive measurements, avoid deformational changes to the protein material during characterization, the need for less material for analysis (compared to infrared (IR) spectroscopy), and the ability to spectroscopically characterize relatively small protein materials (as small as ~1 μm in diameter and a few mm in length) (99,121,126).

3.1.4.2 Acquiring Orientation-Independent Spectra with Polarized Raman Spectroscopy for Qualitative and Quantitative Information

In 2003, a method to obtain a full isotropic spectrum independent of Raman scattered intensity (hereafter referred to as an orientation-independent spectrum) from polarized Raman spectroscopy was developed by Frisk and colleagues (127). Briefly, acquisition of an orientation-independent spectrum for a sample with uniaxial symmetry (such as a fibre) is made complex by the Raman scattering effect. This differs from the

related IR vibrational spectroscopy method, which allows for an orientation-independent spectrum using the equation:

$$A_0 = \frac{A||+2A\perp}{3} \quad (2)$$

where A_0 is the structural absorbance and $A||$ and $A\perp$ are the structural absorbances in the parallel and perpendicular directions to the fibre long axis, respectively (127). This formula cannot be accurately used for Raman spectroscopy, because the intensity of Raman spectra generated from oriented samples depend nontrivially on molecular conformation. Differences in molecular conformation give rise to Raman spectra with varying intensity, wherein the resulting band intensity due to the Raman scattering effect contains information on both the number of oscillators and their orientations (127,128). The consequent variation in band intensity means that the orientation of molecules cannot be accurately and reliably distinguished from molecular conformation itself, thereby resulting in an inability to acquire a spectrum independent of orientation and resulting in an inability to extract information on molecular conformation, such as protein secondary structure content. In other words, conventional Raman spectroscopy or spectromicroscopy cannot distinguish molecular orientation from molecular conformation, which results in only conformational-sensitive information about protein secondary structure. This is a specific limitation with the Raman spectromicroscopy experiments employed in this project, as will be detailed further in section 3.3.4.

Rousseau and colleagues (129) developed a method modified from that of Frisk and colleagues (127) to obtain an orientation-independent spectrum from four polarized Raman spectra using polarized Raman spectromicroscopy on silk monofilaments produced by *B. mori* and *Samia cynthia ricini* silkworms, as well as by spiders. This approach has proven to be effective in both qualitatively and quantitatively characterizing conformational changes in

protein secondary structure and content; molecular orientation; and aa composition (8,50,58,128-130). This approach would be ideal for the present work, but was not possible with the instrument configuration used at Dalhousie University.

3.1.4.3 Using Raman Vibrational Spectromicroscopy to Reveal Molecular Orientation and Secondary Structure Content

Of the many conformation-sensitive Raman scattering bands in silk fibres, the two most informative bands with respect to secondary structuring are the amide I band (1600-1700 cm^{-1}), resulting primarily from of C=O stretching, and the amide III band (1200-1300 cm^{-1}), resulting primarily from C-N stretching and H-N bending (8,121,122). These bands have been used to qualitatively and quantitatively compare conformation of both silkworm silk (88,103,122,125) and spider silk (87,99,104,125,126), with the amide I region being the most frequently characterized band for spider silk fibres to date (8,50,58,128-130). The amide I region has distinct components that have been directly attributed to different secondary structures, as characterized in detail for spider silks by Lefèvre and colleagues (8). In native wrapping silk fibres, Lefèvre and colleagues attribute the amide I band at ~1669 cm^{-1} to a β-sheet conformation and the amide I band at ~1657 cm^{-1} to an α-helical conformation (8).

Based upon the ability to reconstruct orientation-independent spectra, Rousseau and colleagues (129) went beyond qualitative analysis of Raman spectra and were the first to quantitatively characterize the orientation of β-sheets in silk (129). Decomposition of the amide I band by peak-fitting in the orientation-independent spectrum is a highly valuable procedure to obtain quantitative information on protein secondary structure content and aa composition (50,130). Using this procedure, Rousseau and colleagues found that wrapping silk is predominantly α-helical in solution and transitions into a fibre that is moderately

oriented with ~30% β-sheets and ~24% α-helices (58). Shortly after this finding, it was reported that the behaviour of recombinant aciniform W_4 silk-like fibres was very similar (21), with spectral decomposition of the amide I region showing a more intense band at ~1669 cm^{-1} (β-sheet) compared to the band at ~1657 cm^{-1} (α-helix).

3.1.5 AFM

AFM is a type of scanning probe microscopy that can used to characterize sample morphology at the nanoscale or even, in ideal cases, the atomic-level (131,132). AFM works by means of a cantilever (probe) with a sharp tip that is attached to a piezoelectric (PZT) actuator. The cantilever is key in allowing for measurement of force or potential energy between itself and the sample being scanned (131,132). When the cantilever is scanning a target sample, a continuous laser output is focused near its end which is reflected back to a position-sensitive photo detector allowing for measurement of cantilever deflection as a function of tip-sample interaction (131,132).

Three kinds of feedback loop modes are frequently employed in AFM imaging: contact mode, intermittent-contact mode (tapping mode), and non-contact mode. In contact mode, the cantilever tip remains in continuous contact with the sample, while monitoring the resulting interacting forces. This allows measurement of sample topology as a function of tip position. In tapping mode, the cantilever is vibrated at or near its natural resonance frequency, with a resulting loss of energy due to tip-sample interactions (131,132). This information is ultimately employed to monitor tip-sample interactions as a function of position in the controlling feedback loop (131,132). When the cantilever approaches high or low regions of the target sample, its vibrational amplitude will either decrease or increase, respectively, because of this controlled feedback mechanism (131,132). Differences in adhesion interactions from one region to another on a sample may also result in a phase-lag

of the cantilever vibration, allowing for position sensitive monitoring of surface properties even in the absence of topological differences (131,132). AFM is therefore useful to obtain high-resolution morphological feature characterization for fibrous samples such as their ultrastructural organization.

3.1.6 Scanning Electron Microscopy (SEM)

SEM is a form of microscopy that allows for determination of a wide variety of information about materials, including surface topography, chemical composition, and electrical properties (133). A variety of high resolution images may be acquired, such as secondary electron images, backscattered electron images, and voltage-contrast images. Acquisition of secondary electron images is the most common modality of SEM. Specifically, under vacuum conditions, an electron beam is focused on a sample, resulting in excitation of its atoms and escape of its secondary electrons. These secondary electrons are then collected by a secondary electron detector, providing high resolution (1 nm to 1 μm) images containing information on both morphology and surface topography (133).

3.2 Materials and Methods

3.2.1 Far-UV CD Spectroscopy

Spinning dope solutions containing solubilized W_3 at ~8% (w/v) in 70% HFIP/30% H_2O were prepared in the same manner as described in Chapter 2. Spinning dope solutions containing solubilized W_3 at ~10% (w/v) in 60% TFA/20% TFE/20% H_2O were prepared by suspending ~10% (w/v) lyophilized W_3 protein powder into 60% TFA/20% TFE/20% H_2O (v/v/v) in glass vials. TFA and TFE (details of purity/class) was obtained from Sigma-Aldrich (Oakville, ON), and H_2O was type I distilled. Suspensions were vortexed until homogeneous and then incubated for 30 min at room temperature. After incubation, the

suspensions were centrifuged and the spinning dope was recovered in the same manner as the HFIP/H_2O spinning dope solution. Concentrations of both spinning dopes were determined using the same method as described in Chapter 2. A 1/10 dilution was also prepared from each spinning dope, and CD spectra of these solutions were recorded at room temperature using a quartz cuvette with a path length of 0.001 cm (Hellma, Mulheim, Germany) and a J-810 spectropolarimeter (Jasco, Easton, MD). The sensitivity was set to 100 mdeg and data were collected continuously between 180 and 260 nm at room temperature with a 0.1 nm resolution and a scanning speed of 50 nm/min. At least three repetitions including blanks were performed for each spinning dope, and all spectra were averaged and blank subtracted. Once data were obtained, observed ellipticities (in mdeg) were converted to mean residue ellipticity [θ] in 10^3 degrees·cm^2·dmol·$residue^{-1}$.

3.2.2 Fibre Diameter Determination

Fibres were cut into 2 cm-long pieces and mounted on 3 x 2 cm rectangular testing cards with a 1 cm gap in the middle for mechanical testing. Prior to mechanical tests, mounted fibres were examined by optical microscopy and discarded if there were any apparent defects such as uneven thickness or damage. Utilizing an inverted optical microscope with a 10X ocular lens and a 10X objective lens (Axio Observer A_1, Carl Zeiss Canada, Toronto, ON), three micrographs were taken along the long axis of each fibre, one near the middle and two near each end of the fibre. Using ImageJ 1.48v (National Institutes of Health; USA), fibre diameters were estimated at six different places for each micrograph, and averaged to determine fibre diameter.

3.2.3 Mechanical Testing

Mechanical testing was carried out using two different methods. In the first method, tensile testing was performed at room temperature with 32±4% humidity using a Nano Bionix (MTS Nano Instruments) with a 10 mm gauge length. A strain rate of 0.1 mm/s was employed with a tension trigger of 10 μN. The data were transferred to the instrument software (MTS Testwork 4.09A) and exported to Microsoft Excel 2013. Engineering strain was provided, but force (mN; load on specimen) had to be converted into engineering stress in the basis of the fibre diameter estimates determined by optical microscopy. The data were plotted as stress-strain curves, allowing both Young's modulus and toughness to be calculated. Young's modulus was determined as the slope of the stress-strain curves before yield point, and toughness was calculated from the area under the stress-strain curves.

In the second method, tensile testing was achieved under similar conditions as before, but with 24±2% humidity. Again, through helpful discussions with Dr. Laurent Kreplak, a custom-designed mechanical testing set-up was designed and built, where a stainless steel clamp was fabricated at the Department of Physics and Atmospheric Science Machine Shop (Dalhousie University; Halifax, NS) and attached to a KD Scientific model 100 series syringe pump (Holliston, MA) to allow for constant pulling of the fibres at a strain rate of 0.1 mm/s. Once a fibre was mounted on the clamp and the pump, a Mettler Toledo X5105DU Analytical Balance (Greifensee, Switzerland) was employed to determine the weight change as a function of displacement of the syringe pump to determine the applied force. The data were transferred into the instrument software (LabX®) and exported to Microsoft excel 2013. The data were processed in the same manner as before, but with an additional step added in the beginning for both engineering strain and stress. Engineering strain values were obtained using the corresponding displacement values, and dividing these

values by the initial fibre length. For engineering stress, weight (W) or force (F) was calculated using Newton's second law of motion:

$$\mathbf{W} = \mathbf{F} = \boldsymbol{mg} \quad (3)$$

where m = is mass of the fibre (in g), and g = is the acceleration of gravity (9.81 ms^{-2}).

3.2.4 Polarized Light Microscopy

Fibres were visualized using a Nikon Eclipse 600 microscope (Nikon Corporation Instruments Company) equipped with cross polarizing filters and a quarter wave plate analyzer allowing passage of elliptically polarized light. A 10X ocular lens was used with a 40X objective lens to detect birefringence. Images were captured using an AmScope 10MP Microscope Digital Camera and a Nikon TV lens C-0.45x onto an Apple Macintosh iMac computer.

3.2.5 Raman Vibrational Spectromicroscopy

The diffraction limited Raman scattering setup (Figure 3.2) was modified from Gullekson and colleagues (134) and consisted of an inverted microscope (1X71; Olympus, Center Valley, PA) coupled with an iHR550 Raman Spectrometer (Horiba Jobin Yvon, Edison, NJ). Spectra were recorded at room temperature with 35±5% humidity using a 532-nm line (far-field) solid-state laser (Ventus Vis, Laser Quantum, Cheshire, UK) for excitation, and focused using a 60X objective lens to a diameter of approximately 1 μm. The exposure power was ~0.5 mW with an optical density of 0.4 and a confocal pinhole diameter of 200 μm. After passage through an edge filter, scattered light was collected over a spectral range of 400-1800 cm^{-1}, and resolved using the Raman spectrometer. For a given condition, average values from three to four independent fibres were obtained at three to four different positions along the long axis of the fibre at either a perpendicular or parallel (manual 90°

rotation) alignment relative to the incident polarized light. Fibres were routinely checked optically for structural deterioration from the laser, but no apparent damage occurred under these conditions.

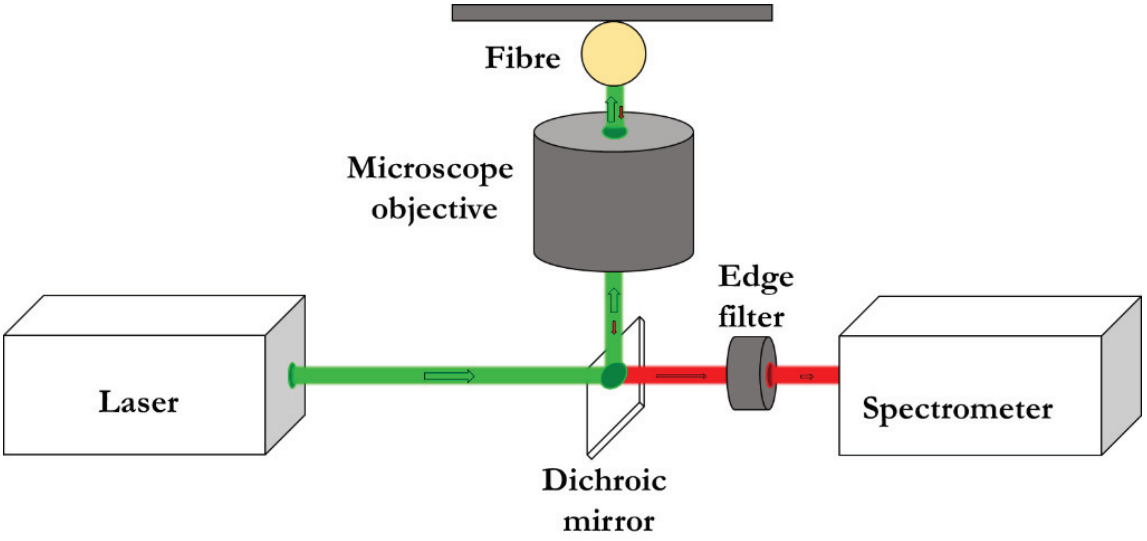

Figure 3.2 Schematic of the Raman vibrational spectromicroscopy instrument employed herein. This instrument consisted of a 532-nm solid-state laser that was polarized and focused onto the fibre samples. The resulting scattered light was passed through an edge pass filter and collected by a spectrometer for analysis.

Spectral manipulation and analysis were carried out with the software GRAMS/AI 9.0 (Thermo Scientific; Markham, ON). Peak correction was performed to eliminate any background fluorescence or cosmic spike interference that may have generated artifacts within the spectra. This was followed by baseline correction with a cubic function and 7-point spectral smoothing. A total average was then taken for each fibre condition for both the perpendicular and parallel alignment positions relative to the incident polarized scattered light. The conformation-sensitive spectra were then plotted for comparison purposes

between the two alignment positions for any given fibre condition. It should be noted that some degree of displacement could not be avoided during manual rotation of the samples. Orientation-independent spectra could not be acquired with this instrument, so quantification of β-sheet and α-helical content was not carried out. However, decomposition of the amide I region using Gaussian fitting, as described previously (50,130), was carried out for qualitative comparison purposes. The peak fitting of the amide I region was carried out in the manner described by Rousseau and colleagues (130) for each alignment. The boundaries for the bandwidth positions at ~1670 cm^{-1} and ~1657 cm^{-1} were ≤ 18.0 cm^{-1}, whereas for all other amide I components and side chain components they were ≤ 20.0 cm^{-1}. The centre points for each band were restrained to only be moved by +/- 1.0 cm^{-1}.

3.2.6 AFM

Fibres for AFM imaging were carefully placed on a glass slide (Fisher Scientific; Ottawa, ON) coated with a thin film of fresh LePage Epoxy glue (Henkel Canada Corporation, ON). The fibres were left to sit at room temperature for at least 60 min to allow the glue to dry. AFM images were acquired using a NanoWizard II Ultra (JPK, Berlin, Germany) mounted on an inverted optical microscope (Axio Observer A_1, Carl Zeiss Canada, Toronto, ON) operating in intermittent-contact mode (room temperature with relative humidity) with silicon cantilevers having a resonance frequency of ~300 kHz and a force constant of 40 N/m. AFM micrographs were then processed with v3.3.32 NanoWizard IP software (JPK) and exported as TIFF files.

3.2.7 SEM

The SEM imaging protocol was adapted from that employed by Xu and colleagues (21). Briefly, fibres for cross-sectional imaging were initially prepared as previously described

in section 3.2.2., but were mounted on a testing card with a 1 mm gap instead of a 1 cm gap. Mounted fibres were then immersed in liquid nitrogen for at least 15 seconds, followed by folding of both ends to break the fibres in the gap region. For each condition, testing cards with the broken fibre ends were fixed on an SEM stub at an angle of ~45°. Once fixed, fibres were coated with gold palladium particles using a Low Vacuum Coater Leica EM ACE200 (Leica Microsystems Inc., ON) prior to acquiring SEM micrographs in secondary electron collection mode using a Hitachi Cold Field Emission S-4700 Scanning Electron Microscope.

3.3 Results and Discussion

3.3.1 CD Spectroscopy Indicates That W_3 Protein Is predominantly α-Helical in Both Spinning Dopes

To evaluate the secondary structuring of W_3 protein in HFIP/H_2O and in TFA/TFE/H_2O, CD spectroscopy was used. Far-UV CD spectra of W_3 in each of the two spinning dopes are shown in Figure 3.3, and an overlay of normalized far-UV CD spectra of W_3 diluted in each of the two spinning dopes is shown in Figure 3.4. Spectra acquired for diluted samples of each spinning dope exhibit one positive band at 193 nm, and two negative bands at 208 nm and 222 nm, demonstrating that the solubilized form of W_3 in these conditions has prevalent α-helical content (Figure 3.3). This is consistent with native wrapping silk, where the natural dope contains a high soluble protein concentration in the gland is predominantly α-helical in structure (58). These spectra are also very similar to those previously observed when W_3 was solubilized at much lower concentration (~0.006% w/v), in 50 mM phosphate buffer, at pH 7.5 (21).

However, it is also clear that there are differences between the two spinning dope conditions when comparing spectra obtained at the actual concentrations employed for spinning, to those obtained after dilution. This is the consequence of insufficient light reaching the photomultiplier tube (PMT) of the CD instrument, due to overly intense absorption, scattering, or a combination of both factors. In turn, this increases voltage, making data unreliable due to a decrease in signal-to-noise ratio. This is even more problematic when samples are highly concentrated and measurements are made at lower wavelengths (112). This is evident when observing W_3 in each of the two spinning dopes, in particular at the higher energy regime (~205 nm and below), and leads to a characteristic shift in the spectra (Figure 3.3). This effect is more apparent in the HFIP/H_2O spinning dope, where a complete saturation occurs with no appreciable light reaching the PMT (Figure 3.3) and resulting in a more dramatic shift when compared to the TFA/TFE/H_2O spinning dope (Figure 3.3). Due to the volatile nature of the HFIP solvent, the HFIP/H_2O spinning dope is much more prone to evaporation than the TFA/TFE/H_2O dope, especially when working with extremely small volumes (~2.6 μL), which is an inherent limitation of using a small path length (0.001 cm) quartz cuvette. Evaporation was unavoidable with the HFIP/H_2O spinning dope, resulting in a more intense spectrum and an inaccurate protein concentration; therefore, greater saturation of absorbance was observed at the higher energy regime than for the TFA/TFE/H_2O spinning dope (Figure 3.3).

Although saturation of absorption did occur, dilution of the spinning dopes removed this effect and illustrated that W_3 was indeed in a native-like α-helical form in both spinning dopes. Additionally, when examining dilute spectra of diluted samples in Figure 3.3, it is apparent that the 208 nm band is more pronounced and the 222 nm band is less pronounced in the HFIP/H_2O spinning dope (Figure 3.3A) than in the TFA/TFE/H_2O spinning dope

(Figure 3.3B). This behavioural difference between the two spinning dopes at 208 nm and 222 nm is clearer when overlaying spectra normalized at 222 nm and 208 nm, respectively (Figures 3.4A and 3.4B).

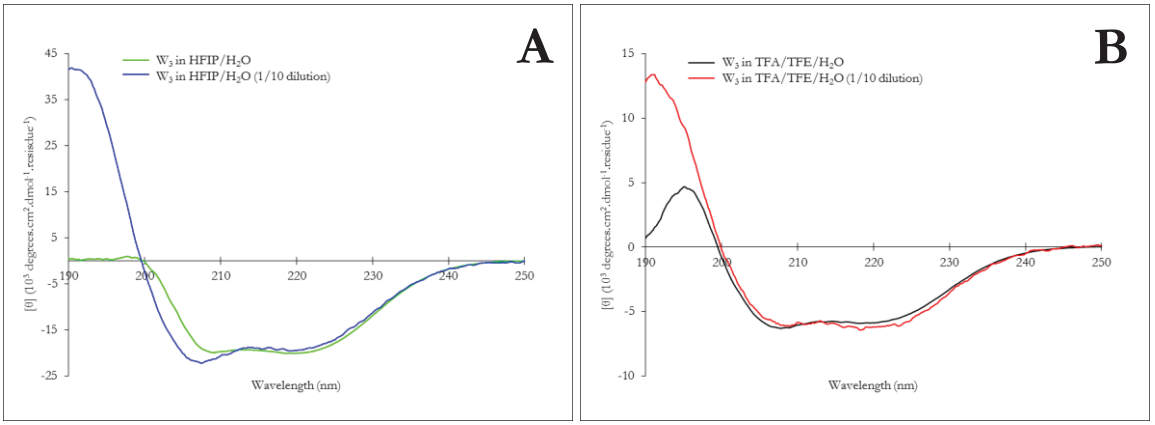

Figure 3.3 Far-UV CD spectra of W_3 in HFIP/H_2O or TFA/TFE/H_2O. Undiluted (~8% w/v) or diluted (~0.8% w/v) W_3 in HFIP/H_2O (A) or undiluted (~10% w/v) or diluted (~1% w/v) W_3 in TFA/TFE/H_2O (B).

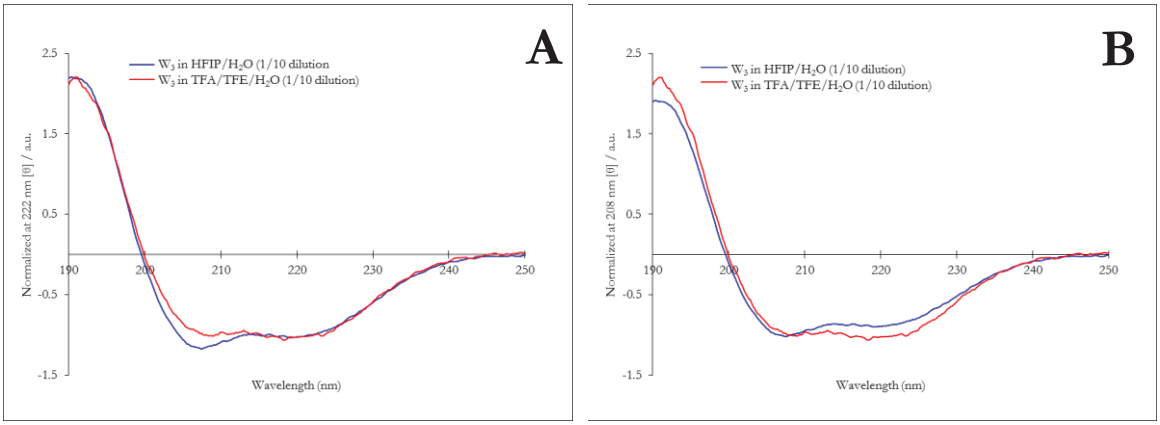

Figure 3.4 Overlay of normalized far-UV CD spectra of W_3 in HFIP/H_2O and TFA/TFE/H_2O. Diluted spectra were normalized either to 222 nm (A) or 208 nm (B).

3.3.2 Mechanical Properties of W_3 Fibres Are Improved Following Post-Spin Stretching and Are Different In Both Spinning Dopes

Tensile testing was carried out on AS and PS-stretched W_3 fibres from each of the two spinning dopes to generate stress-strain curves, allowing assessment of fibre mechanical properties. Representative stress-strain curves for AS and PS 4x W_3 fibres spun from either the HFIP/H_2O or the TFA/TFE/H_2O spinning dope are provided in Figure 3.5, with mechanical properties reported in Table 3.1. Fibre strength dramatically improved in PS 4x W_3 fibres relative to AS W_3 fibres, consistent with previous reports on the effects of inclusion of a post-spin stretching step upon mechanical properties of wet-spun silk-based fibres (Table 3.2). Based upon these precedents, this improvement in mechanical properties is likely the result of promoting further structural changes and molecular alignment within the fibre. In particular, it is likely that the AS W_3 fibre state results in a partial crystalline phase transition, without sufficient time to complete the transition into stacking/aggregation of crystalline β-sheets (20), and also alignment of α-helical components, the latter being a unique feature of both the native wrapping and pyriform silk fibres (8).

When W_3 fibres are subjected to a post-spin stretch, it is reasonable to speculate that this would allow for a more complete crystalline phase transition followed by a more complete alignment of α-helical components, both involving additional hydrogen bonding of their respective C=O and N-H groups. Specifically, post-spin stretching likely permits additional extension of the protein chains, thereby promoting further stacking/aggregation of β-sheets, which is attributed to an increase in strength (20,45). It also likely permits additional alignment of α-helical components, which may be attributed to mechanical features such as extensibility. Although these phenomena may be occurring, it must be taken with consideration that these structural changes as well as molecular alignment within the

fibre could behave differently depending on the behaviour of the W_3 protein in each spinning dope prior to fibre spinning. This is evident with the differences observed in CD spectra that were acquired between the two spinning dope conditions, as described in the previous section.

To clarify and support the idea of stacking/aggregation of crystalline β-sheets, a two-step mechanism has previously been proposed for the nucleation-dependent aggregation of β-sheets for the spinning process of *B. mori* cocoon silk (135). Briefly put, prior to fibre spinning, it has been suggested that there is a nucleation event that occurs beginning with a conversion from soluble random coil to insoluble β-sheet, termed β-sheet nuclei. These act as nucleation sites for stacking/aggregation of β-sheets once the fibres are spun. Additionally, the greater the number of β-sheet nuclei that are formed during this conversion, the more thermodynamically favourable growth becomes towards stacking/aggregation of crystalline β-sheets within the fibre (135). This mechanism has also been demonstrated in the spinning process of *N. clavipes* MA silk, where, from the soluble to fibrous form, there is a transformation from disordered and helical structures to highly oriented β-sheets, with formation of β-sheets preceding molecular alignment within the fibre (51). With this understanding, it is sensible to suggest that a similar phenomenon is occurring within wet-spun W_3 fibres.

As mentioned previously (section 3.1.4.3), wrapping silk is predominantly α-helical in solution and transforms into a fibre that contains a moderately oriented mixture of β-sheets and α-helices (58). In contrast to other silk types such as MA silk, it has been suggested that this unique combination of structures within the wrapping silk fibre means that the α-helical to β-sheet conversion is not complete; rather, the α-helical components likely become more aligned along the fibre long axis (8). This ties in nicely with the hypothesis that additional

alignment of the α-helical components may be occurring following post-spin stretching of the W_3 fibres. Although this phenomenon may be occurring, as stated previously, structural changes as well as molecular alignment within the fibre may behave differently depending on the behaviour of the W_3 protein in differing spinning dopes prior to fibre spinning.

This unique combination of structures within the native wrapping silk fibre, in particular with the distinct retention of significant α-helical content, may provide insight as to why the functional (i.e., mechanical) properties differ from other silk types (Table 1.1). It can be hypothesized that in the native wrapping silk fibre, a different class of stacking/aggregation of β-sheets is occurring within the fibre to permit adequate alignment of α-helices, which may account for the unique strength and extensibility, respectively. Following from a similar line of thinking, the specific orientation of these structures within the fibre is likely beneficial for both allowing for more adequate networking/geometry of hydrogen bonding in β-sheet regions, contributing to strength, and more adequate networking/geometry of hydrogen bonding in α-helical regions, contributing to extensibility. The α-helical regions may in fact serve as a reversible "spring" for the fibre, where the benefits of orientation/alignment would allow for a stronger spring, promoting greater extensibility. This spring function may be exemplified in W_3 fibres spun from the TFA/TFE/H_2O spinning dope, where it is absent in the AS W_3 fibres, but present in these fibres after being subjected to a post-spin stretch.

Keeping this in mind, although strength improved following post-spin stretching of wet-spun fibres from each dope, mechanical properties were drastically different for the two spinning dopes (Figure 3.5). Compared to the TFA/TFE/H_2O spinning dope, PS 4x W_3 fibres spun from the HFIP/H_2O spinning dope were weaker with an engineering stress of 92±8 MPa, were more brittle with an engineering strain of 3±1%, and were less tough with a

toughness of 1±0.3 MJ·m^{-3} (Table 3.1). Conversely, PS 4x W_3 fibres spun from the TFA/TFE/H_2O spinning dope were stronger, more extensible, and tougher with an engineering stress of 139±27 MPa, engineering strain of 47±21%, and toughness of 59±33 MJ·m^{-3} (Table 3.1). Additionally, it should be noted that the mechanical properties of these fibres are better than W_3 fibres manually drawn from a low-concentration (~0.04% w/v) buffered aqueous solution (Table 3.2).

Hence, with the same W_3 construct, it is clear that spinning dope solvent composition plays a major role in the final mechanical properties of the fibres produced through a wet-spinning/post-spin stretching method. A similar result was observed by Heidebrecht and colleagues (20), who postulated on the basis of their observation that spinning dope solvent composition used for wet-spinning of MA-based proteins was critical for pre-structuring of the terminal and/or core domains, thereby allowing for appropriate pre-assembly needed for fibre formation and improved mechanical properties. In principle, the same phenomenon is likely occurring with the repetitive domains of the W_3 construct, where different pre-structuring and the resulting effects upon pre-assembly of protein units within the two spinning dopes is giving rise to different mechanical properties. This is also reflected by the notable differences observed in the CD spectra (Figures 3.3 and 3.4).

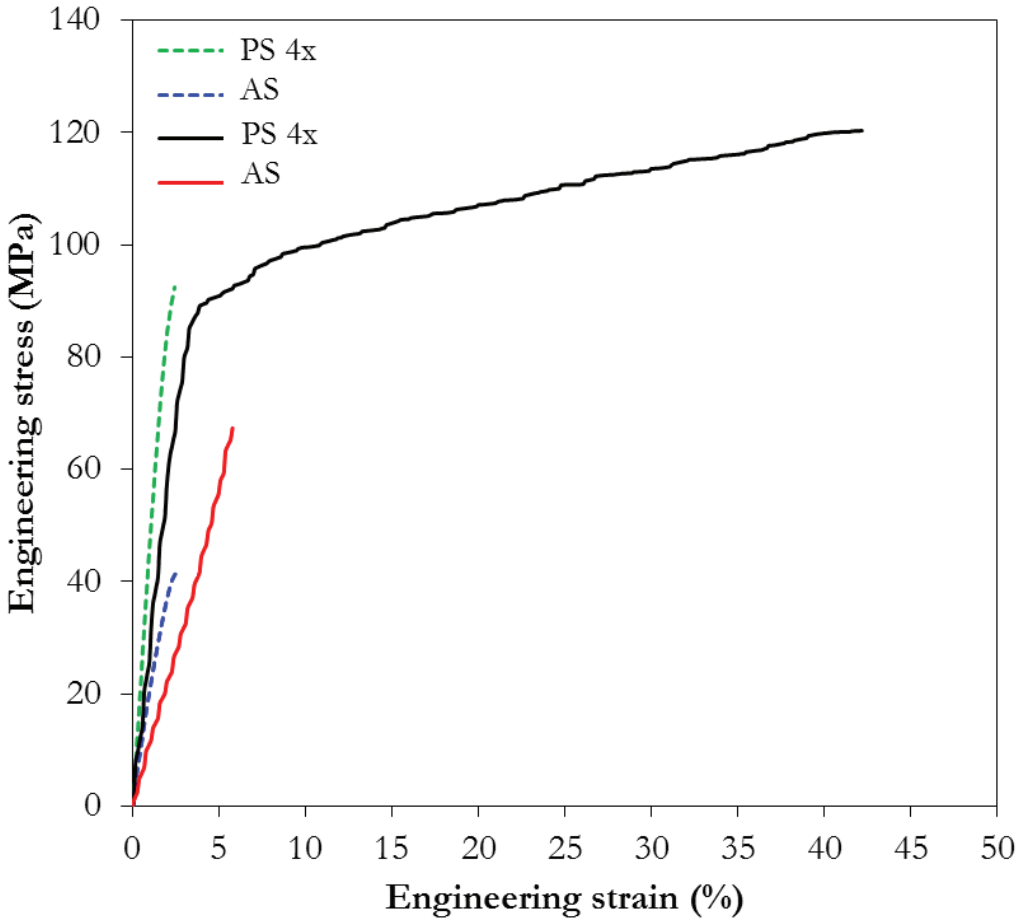

Figure 3.5 Representative stress-strain curves for W_3 fibres. AS and PS 4x W_3 fibres spun from the HFIP/H_2O spinning dope (represented as dotted lines), and AS and PS 4x W_3 fibres spun from the TFA/TFE/H_2O spinning dope (represented as solid lines).

Table 3.1 Mechanical properties of W_3 fibres spun from the indicated dope.

Protein origin	Recombinant protein	Spinning dope concentration (w/v %)	Spinning dope content	Engineering stress (MPa)	Engineering strain (%)	Young's modulus (GPa)	Toughness ($MJ \cdot m^{-3}$)	Diameter (μm)
AcSp1	W_3	~10[a]	Protein dissolved in 60% TFA/20% TFE/20% H_2O	AS: 61±7 PS 4x: 139±27	AS: 6±4 PS 4x: 47±21	AS: 2±1 PS 4x: 3±1	AS: 2±2 PS 4x: 59±33	AS: 20±4 PS 4x: 9±1
		~8[b]	Protein dissolved in 70% HFIP/30% H_2O	AS: 36±12 PS 4x: 92±8	AS: 3±1 PS 4x: 3±1	AS: 1±1 PS 4x: 5±1	AS: 1±0.2 PS 4x: 1±0.3	AS: 23±1 PS 4x: 9±1

[a] Mechanical data for AS and PS 4x are based on 6 fibres and 10 fibres, respectively.
[b] Mechanical data for AS and PS 4x are based on 15 fibres and 12 fibres, respectively.

Table 3.2 Mechanical properties of previously characterized wet-spun recombinant spider silk protein fibres. The spinning dopes employed are HFIP, unless otherwise specified in the footnotes.

Protein origin (reference)	Recombinant protein	Spinning dope concentration (w/v %)	Engineering stress (MPa)	Engineering strain (%)	Young's modulus (GPa)	Toughness ($MJ \cdot m^{-3}$)	Diameter (μm)
AcSp1 (21)[a]	W_3	0.04	67±16	31±11	2±1	18±10	1.5±0.1
MaSp2 (68)	1E (GPG-rich)1Ala8	56	AS: 10±4 PS 4x: 29±14	AS: 2±1 PS 4x: 27±14	AS: 0.9±0.2 PS 4x: 2±0.6	AS: 0.1±0.1 PS 4x: 7±5	AS: 106±4 PS 4x: 51±5
	2E (GPG-rich)2Ala8	56	AS: 7±3 PS 3-4x: 14±7	AS: 2±2 PS 3-4x: 72±82	AS: 1±0.4 PS 3-4x: 1±1	AS: 0.1±0.2 PS 3-4x: 9±11	AS: 106±11 PS 3-4x: 51±9
	3E (GPG rich)3Ala8	56	AS: 14±7 PS 4x: 39±7	AS: 1±01 PS 4x: 181±104	AS: 2±2 PS 4x: 2±0.4	AS: 0.1±0.1 PS 4x: 59±37	AS: 62±3 PS 4x: 36±6
MaSp and Flag (53)	G (GGX-rich)	15	PS 3x: 56±16	PS 3x: 133±76	n.d.	PS 3x: 62±48	PS 3x: 13±2
	GY (GGX and GPGGX-rich)	15	PS 3x: 47±25	PS 3x: 45±44	n.d.	PS 3x: 18±23	PS 3x: 22±5
	GF (GGX-rich and spacer motifs)	15	AS: 19±5 PS 3x: 136±60	AS: 1±1 PS 3x: 37±13	n.d.	AS: 0.1±0.1 PS 3x: 36±15	AS: 37±1 PS 3x: 20±4
	GFY (GGX and GPGGX-rich with spacer motifs)	15	AS: 26±18 PS 3x: 151±31	AS: 1±0.4 PS 3x: 85±38	n.d.	AS: 0.1±0.1 PS 3x: 89±24	AS: 27±1 PS 3x: 15±1
MaSp1 (74)	16 mer	20	PS 5x: ~81	PS 5x: ~3	PS 5x: ~3.8	n.d.	n.d.
	32 mer	20	PS 5x: ~202	PS 5x: ~3	PS 5x: ~8.3	n.d.	n.d.
	48 mer	20	n.d.	n.d.	n.d.	n.d.	n.d.
	64 mer	20	PS 5x: ~253	PS 5x: ~4	PS 5x: ~10	n.d.	n.d.
	80 mer	20	n.d.	n.d.	n.d.	n.d.	n.d.
	96 mer	20	PS 5x: 508±108	PS 5x: 15±5	PS 5x: 21±4	n.d.	n.d.
TuSp1 and ECP (Thioredoxin and H_6-tag) (70)	1XC	20	PS 3.5x: 95±3 PS 6x: 159±8	PS 3.5x: 25±4 PS 6x: 13±1	n.d.	PS 3.5x: 21±4 PS 6x: 12±2	PS 3.5x: 31±1 PS 6x: 25±0.3
	1X	20	PS 3.5x: 80±12	PS 3.5x: 9±3	n.d.	PS 3.5x: 7 ±2	PS 3.5x: 61±3
	ECP-2C	20	PS 3.5x: 122±5	PS 3.5x: 18±1	n.d.	PS 3.5x: 17±1	PS 3.5x: 47±1
MaSp and Flag (72)	(A1S8)20	26–27	Step 1: 28±25 Step 2: 102±33 Step 3: 128±23	Step 1: 2±1 Step 2: 19±18 Step 3: 52±24	Step 1: 1±1 Step 2: 3±1 Step 3: 4±1	Step 1: 0.3±0.4 Step 2: 19±21 Step 3: 55±24	Step 1: 68±25 Step 2: 34±6 Step 3: 28±3
	(Y1S8)20	26–27	AS fibres were too brittle to be handled, only hand pulled fibres were tested				

Protein origin (reference)	Recombinant protein	Spinning dope concentration (w/v %)	Engineering stress (MPa)	Engineering strain (%)	Young's modulus (GPa)	Toughness ($MJ \cdot m^{-3}$)	Diameter (μm)
TuSp (RP) and MiSp (CTD) (71)	11RPC	8-10	AS: <100 PS 5x: 308±57	AS: n.d. PS 5x: ~10	AS: n.d. PS 5x: 9±3	n.d.	AS: n.d. PS 5x: 6–14
MaSp2 Analogue (ADF3) (66)[b]	ADF3	10-28 (>23 is better	2 gpd native: 7-11 gpd	43-60	43-111 gpd native: 38-76 gpd	1 gpd native: 0.6-1.3 gpd	10-40
MaSp1 (69)	(MaSp1)16	30	AS: 16±7 PS 3x: 54±10	AS: 5±0.4 PS 3x: 5±4	AS: 1±1 PS 3x: 3.1±1	AS: 0.1±0.1 PS 3x: 2±2	AS: 41±3 PS 3x: 24±5
	(MaSp1)24	30	AS: 36±8 PS 3x: 133±49	AS: 3±1 PS 3x: 23±19	AS: 3±1 PS 3x: 6±2	AS: 1±1 PS 3x: 24±9	AS: 41±4 PS 3x: 17±5
MaSp2 Analogue (eADF3 variants) (20)[c]	$(AQ)_{12}$	CSD: 10-17	AS: 10±2 PS 4x: 66±22	AS: 17±9 PS 4x: 38±16	AS: 1±0.4 PS 4x: 2±1	AS: 1±0.4 PS 4x: 20±12	AS: 35±7 PS 4x: 15±5
	$(AQ)_{24}$	CSD: 10-17	AS: 22±4 PS 6x: 280±48	AS: 22±3 PS 6x: 65±6	AS: 0.4±0.1 PS 6x: 4±1	AS: 4±1 PS 6x: 110±24	AS: 70±7 PS 6x: 22±2
	$(AQ)_{12}$NR3	CSD: 10-17	AS: 32±12 PS 6x: 244±23	AS: 10±3 PS 6x: 64±11	AS: 2±1 PS 6x: 4±0.4	AS: 2±2 PS 6x: 83±10	AS: 59±8 PS 6x: 23±3
		BSD: 10-15	AS: 54±16 PS 6x: 383±113	AS: 7±2 PS 6x: 95±24	AS: 2±1 PS 6x: 3±2	AS: 2±1 PS 6x: 172±52	AS: 39±6 PS 6x: 26±6
	$(AQ)_{24}$NR3	CSD: 10-17	AS: 29±2 PS 6x: 161±65	AS: 5±1 PS 6x: 50±12	AS: 1±0.2 PS 6x: 3±1	AS: 1±0.1 PS 6x: 49±26	AS: 57±0.1 PS 6x: 30±5
		BSD: 10-15	AS: 23±4 PS 6x: 355±92	AS: 7±3 PS 6x: 44±13	AS: 1±0.3 PS 6x: 5±2	AS: 1±1 PS 6x: 83±18	AS: 56±1 PS 6x: 21±5
	N1L$(AQ)_{12}$	CSD: 10-17	AS: 19±3 PS 4x: 212±53	AS: 8±1 PS 4x: 51±17	AS: 1±0.1 PS 4x: 4±1	AS: 1±0.4 PS 4x: 72±33	AS: 42±6 PS 4x: 15±2
	N1L$(AQ)_{24}$	CSD: 10-17	AS: 15±3 PS 3x: 24±7	AS: 6±2 PS 3x: 10±6	AS: 1±0.2 PS 3x: 1±0.3	AS: 0.4±0.2 PS 3x: 2±1	AS: 78±21 PS 3x: 55±9
	N1L$(AQ)_{12}$ NR3	CSD: 10-17	AS: 21±8 PS 6x: 251±57	AS: 4±2 PS 6x: 82±13	AS: 1±0.4 PS 6x: 3±1	AS: 0.4±0.1 PS 6x: 111±33	AS: 57±3 PS 6x: 24±7
		BSD: 10-15	AS: 13±2 PS 6x: 370±59	AS: 6±1 PS 6x: 110±25	AS: 1±0.1 PS 6x: 4±1	AS: 0.3±0.1 PS 6x: 189±33	AS: 155±8 PS 6x: 27±10
	N1L$(AQ)_{24}$ NR3	CSD: 10-17	AS: 22±3 PS 6x: 180±50	AS: 8±2 PS 6x: 47±14	AS: 1±0.2 PS 6x: 4±1	AS: 1±0.4 PS 6x: 50±13	AS: 62±8 PS 6x: 27±4
	N1L$(AQ)_{24}$ NR3	BSD: 10-15	AS: 25±5 PS 6x: 308±131	AS: 7±2 PS 6x: 54±15	AS: 1±0.2 PS 6x: 5±2	AS: 1±0.4 PS 6x: 90±29	AS: 75±14 PS 6x: 20±6

Protein origin (reference)	Recombinant protein	Spinning dope concentration (w/v %)	Engineering stress (MPa)	Engineering strain (%)	Young's modulus (GPa)	Toughness ($MJ \cdot m^{-3}$)	Diameter (μm)
MaSp1 and MaSp2 (81)[d]	rMaSp1 and rMaSp2	12	192±52	28±26	n.d.	34±34	n.d.

[a] Hand-pulled from 10 mM Tris HCl, pH 8.0.
[b] Phosphate buffered saline.
[c] 6 M guanidinium thiocyanate and dialyzed.
[d] Not disclosed.

3.3.3 Birefringence Suggests Increased Molecular Alignment Following Post-Spin Stretching

Since mechanical behaviour dramatically improved in PS 4x W_3 fibres relative to AS W_3 fibres, the presence of an overall increase in molecular orientation following post-spin stretching appeared likely. To test for this property, the degree of birefringence was characterized in each fibre type using polarized light microscopy, which permitted qualitative and correlative analysis of overall molecular orientation. Polarized light micrographs of AS and PS 4x W_3 fibres spun from either the HFIP/H_2O or the TFA/TFE/H_2O spinning dope are provided in Figures 3.6 and 3.7, respectively. Notable differences can be observed between AS W_3 fibres from the two spinning dopes (Figures 3.6A and 3.7A). Also notably, in both conditions, birefringence increased following post-spin stretching, suggesting an increase in alignment of protein molecules within PS fibres (Figures 3.6B and 3.7B). This implies that there is an overall preferential molecular orientation and uniformity within these fibres, which is correlated to improved mechanical properties (Table 3.1). These results agree with previous reports of post-spin stretching of wet-spun silk-based fibres, where it was observed that there was an increase in birefringence, which was correlated to an improvement in mechanical properties (88,119). Although this correlation appears clear, since polarized light microscopy is only detecting the overall molecular orientation,

crystalline and amorphous regions within silk fibres cannot be distinguished (88,118-120). Because of this, it is unclear what proportion of crystallinity and amorphicity are attributable to the differing mechanical properties of W_3 fibres.

However, based on the fact that stacking/aggregation of crystalline β-sheets is typically attributed to an improvement in strength, it can be postulated that the same behaviour may be occurring in both fibre conditions following post-spin stretching, but in different proportions or phases. Specifically, there may be a more complete crystalline phase transition in PS 4x W_3 fibres spun from the TFA/TFE/H_2O spinning dope relative to PS 4x W_3 fibres spun from the HFIP/H_2O spinning dope, which may explain why the former are stronger (Table 3.1). With a possibly more complete crystalline phase transition and, therefore, more compact stacking/aggregation of crystalline β-sheets, this may permit a higher proportion of amorphicity and alignment of α-helical components, thereby being attributed to properties of greater extensibility. This rationale ties in nicely with what is already known about the so-called amorphous regions in other silk types, where an increased proportion of amorphous character surrounding the crystalline β-sheets regions is attributed to greater extensibility (47,48,53). These structural hypotheses were tested using Raman spectromicroscopy, and will be discussed in more detail in the next section. As detailed in Chapter 1, in MA and Flag spidroins, the amorphous regions are correlated to GGX motifs (47,48,53). In contrast, W_3 does not contain this motif (13,21), so it is unclear if there are particular motifs, or other conditions, that are promoting increased amorphous content and/or extensibility in W_3 fibres spun from the TFA/TFE/H_2O spinning dope.

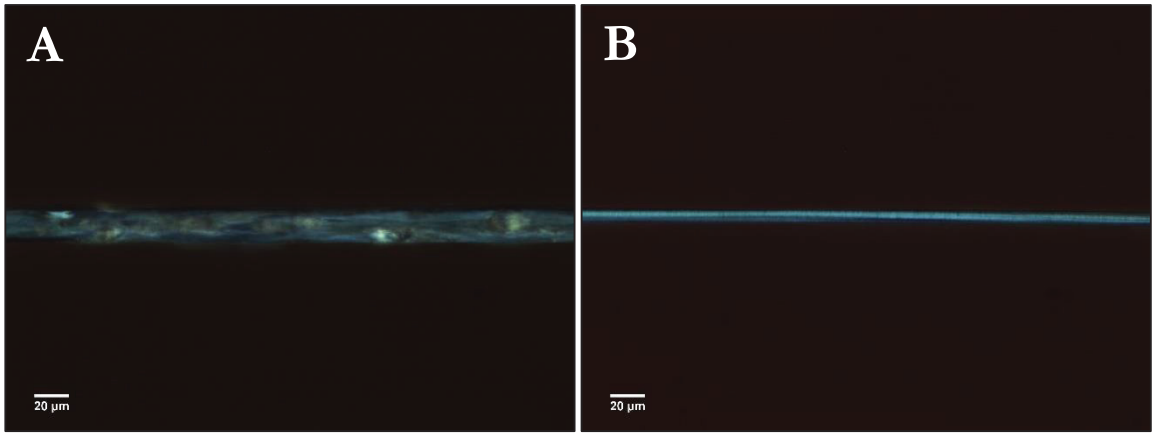

Figure 3.6 Birefringence of W_3 fibres spun from the HFIP/H_2O spinning dope visualized by polarized light microscopy. AS fibres (A) and PS 4x fibres (B).

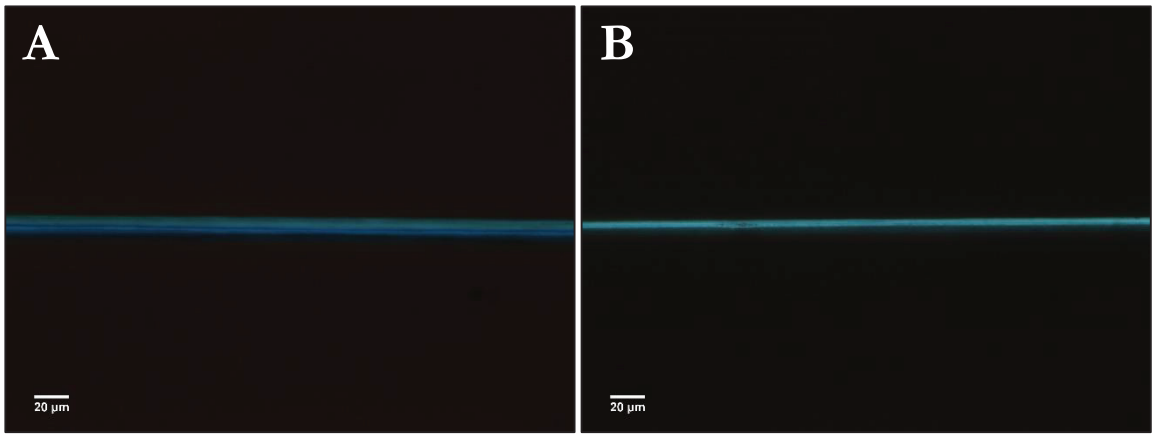

Figure 3.7 Birefringence of W_3 fibres spun from the TFA/TFE/H_2O spinning dope visualized by polarized light microscopy. AS fibres (A) and PS 4x fibres (B).

3.3.4 W_3 Fibres Undergo Conformational Changes upon Post-Spin Stretching

Having observed both an improvement in mechanical properties and an increase in birefringence following post-spin stretching of AS W_3 fibres, the next step was to investigate if any conformational changes in protein secondary structure were occurring. This was achieved using Raman spectromicroscopy. Representative Raman spectra and amide I band

decompositions of AS and PS 4x W_3 fibres spun from either the HFIP/H_2O or the TFA/TFE/H_2O spinning dope are shown in Figures 3.8-3.11. Additionally, Raman bands within the representative Raman spectra were linked to the position and assignment of the main Raman bands present in native spider silks (Table 3.3), as characterized in detail by Lefèvre and colleagues (8). Since the method employed in this work is conformationally-sensitivite to protein secondary structure, interpretation of changes in protein secondary structure from these spectral data are reliable. However, as previously mentioned, orientation-independent spectra could not be determined. Because of this, interpretation of the degree and directionality of orientation of secondary structural units could not be accurately carried out using these experiments, and will therefore not be described. Additionally, interpretation must be considered with the caveat that the perpendicular and parallel alignment were not absolute relative to the fibre.

With that being said, a conformational change in protein secondary structure is clear in the W_3 fibres spun from the HFIP/H_2O spinning dope between the AS and PS 4x states (Figure 3.8). Specifically, in the amide I region, it can be observed that AS W_3 fibres spun from the HFIP/H_2O spinning dope exhibit a mix of α-helical and β-sheet conformations, which shifts to a more predominant β-sheet conformation in the PS 4x W_3 fibres (Figure 3.9). This change to a β-sheet-enriched structure reinforces the idea that a more complete crystalline phase transition is occurring of the already oriented β-sheets, whereas the molecular alignment of the α-helical component may also be improving. Specifically, with regard to the former, this could reflect an enrichment of β-sheet microcrystal formation, therefore promoting greater mechanical strength (Table 3.1). Additionally, the differences in Raman spectra for each orientation are consistent with anisotropy in both AS and PS 4x W_3 fibres (Figure 3.8), consistent with the observed birefringence (Figure 3.6).

As with the W_3 fibres spun from the HFIP/H_2O spinning dope, following post-spin stretching, a conformational change in protein secondary structure also occurs in the W_3 fibres spun from the TFA/TFE/H_2O spinning dope (Figure 3.10). However, there are differences in conformational behaviour of fibres spun from this dope. Specifically, in the amide I region, W_3 fibres spun from the TFA/TFE/H_2O spinning dope already exhibit a more pronounced β-sheet conformation compared to the W_3 fibres spun from the HFIP/H_2O spinning dope (Figure 3.11). Following post-spin stretching, the β-sheet conformation is even more prominent (Figure 3.11) relative to the PS 4x W_3 fibres spun from the HFIP/H_2O spinning dope (Figure 3.9). It is evident that both AS and PS 4x W_3 fibres spun from the TFA/TFE/H_2O spinning dope exhibit anisotropy in secondary structuring (Figure 3.10). This is consistent with the fact that the W_3 fibres spun from the TFA/TFE/H_2O spinning dope exhibit greater birefringence (Figure 3.7A) than W_3 fibres spun from the HFIP/H_2O spinning dope (Figure 3.6A). The anisotropy is a clear indication that there is a preferential alignment of molecules relative to the fibre long axis.

In summary, it can be postulated that the α-helical component becomes even more oriented within the W_3 fibres spun from the TFA/TFE/H_2O spinning dope following post-spin stretching, since an enrichment of β-sheet microcrystal formation may imply that the β-sheet component is already oriented within the AS W_3 fibres. This is supported by the fact that there is both a more intense anisotropic effect in secondary structuring as demonstrated in Figure 3.10, as well as greater birefringence within these fibres (Figure 3.7). This correlates well with the differing mechanical properties, especially with the dramatic improvement in extensibility in the PS 4x W_3 spun from TFA/TFE/H_2O spinning dope relative to the PS 4x W_3 fibres spun from the HFIP/H_2O spinning dope.

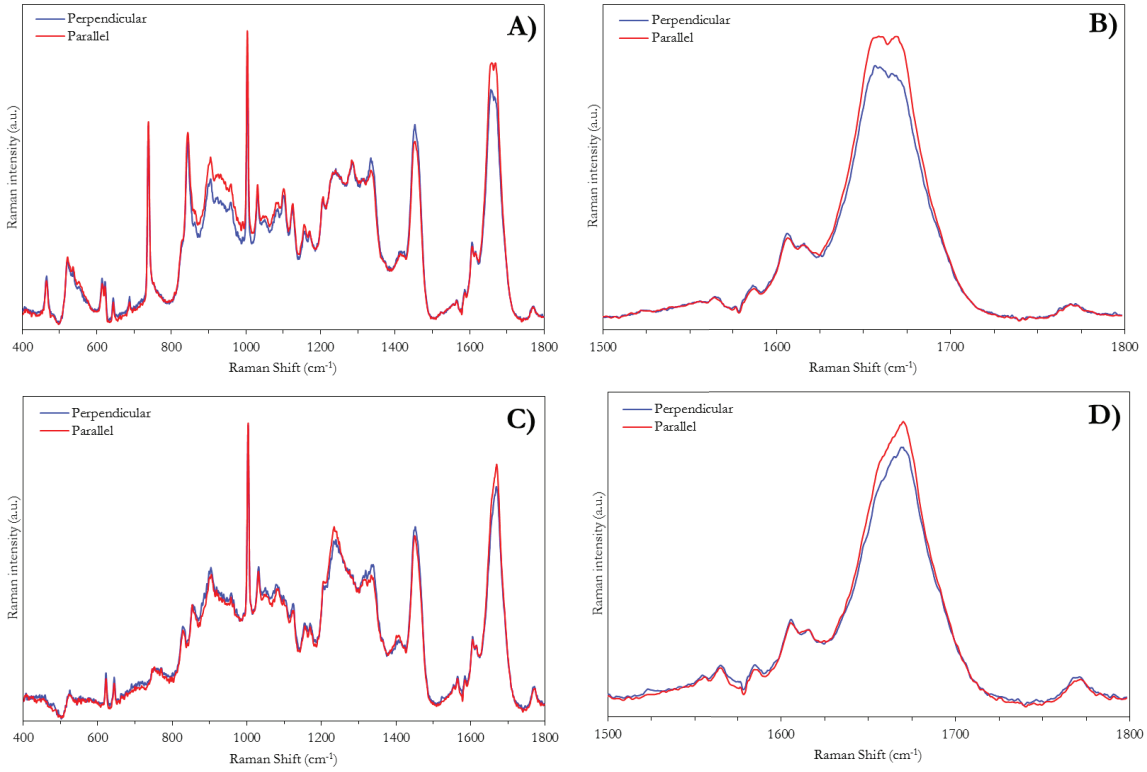

Figure 3.8 Raman spectra of W_3 fibres spun from the HFIP/H_2O spinning dope in perpendicular (blue) or parallel (red) alignment relative to the incident polarized scattered light. Full spectra range of AS fibres (A), amide I region of AS fibres (B), full spectra range of PS 4x fibres (C), and amide I region of PS 4x fibres (D).

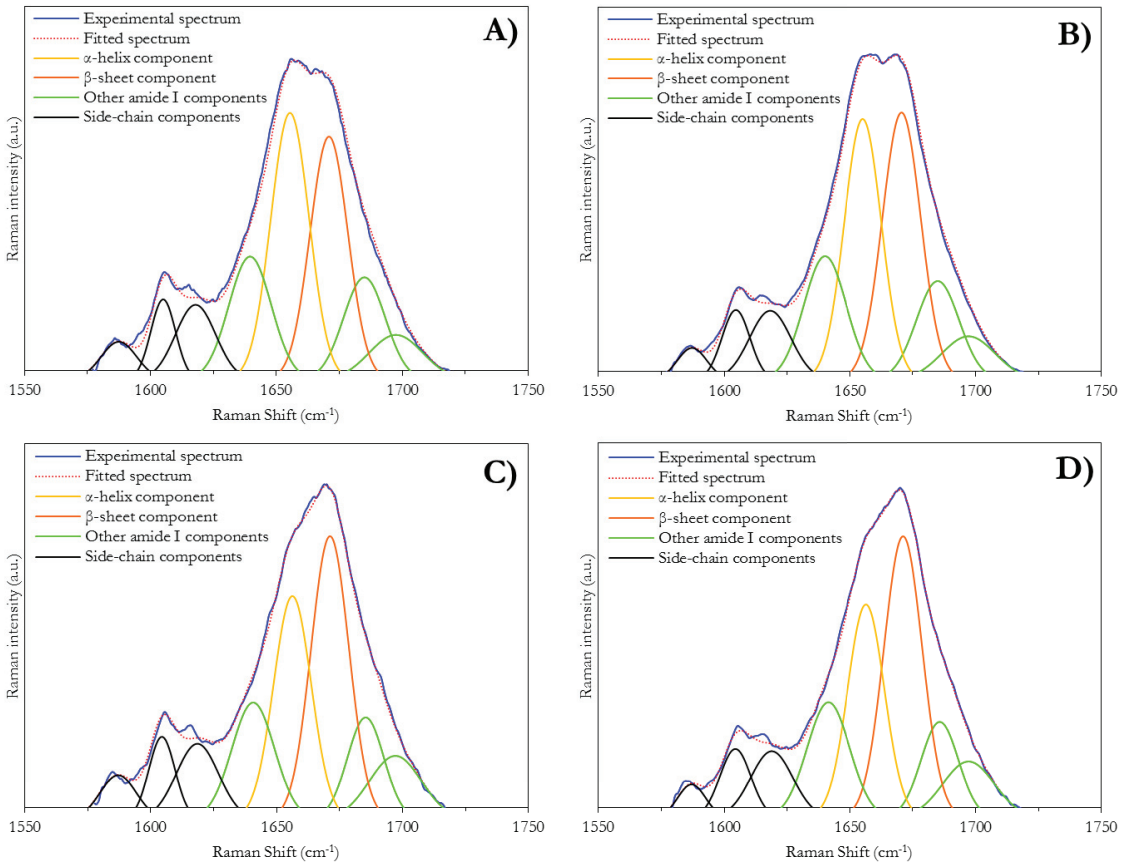

Figure 3.9 Decomposition of the amide I region of W_3 fibres spun from the HFIP/H_2O spinning dope. Perpendicular orientation of AS fibres (A), parallel orientation of AS fibres (B), perpendicular orientation of PS 4x fibres (B), and parallel orientation of PS 4x fibres (D).

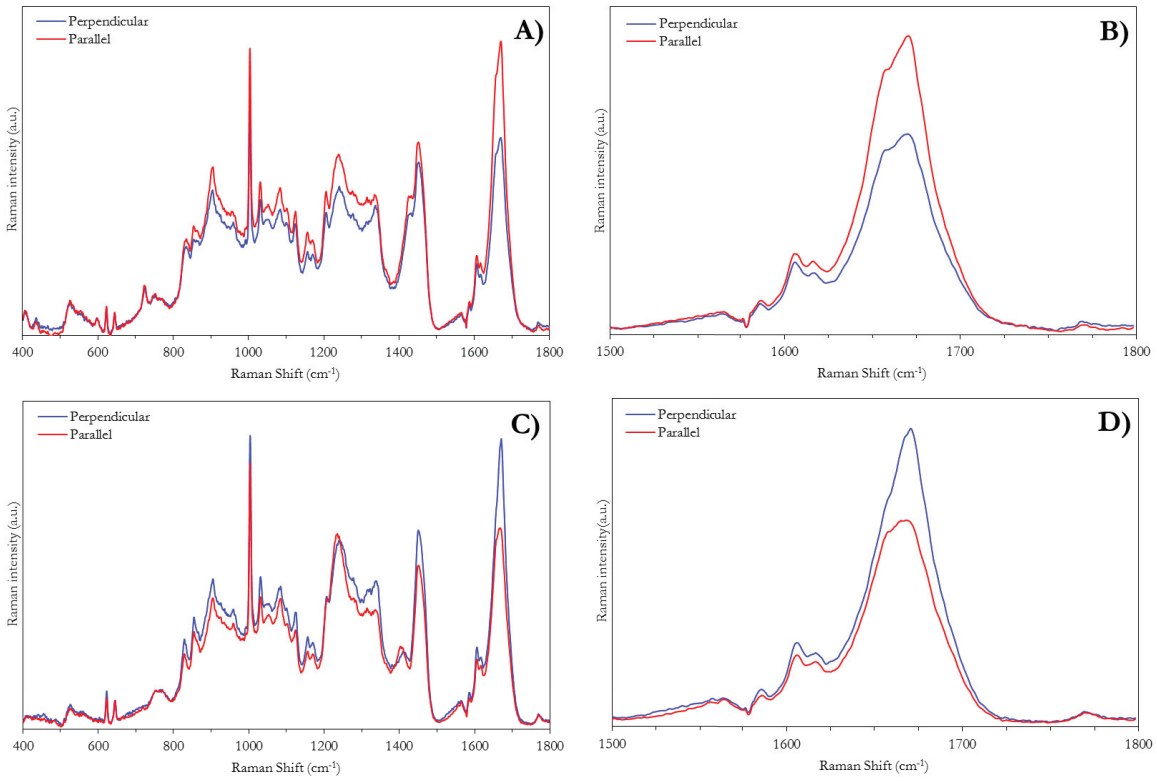

Figure 3.10 Raman spectra of W_3 fibres spun from the TFA/TFE/H_2O spinning dope in perpendicular (blue) or parallel (red) alignment relative to the incident polarized scattered light. Full spectra range of AS fibres (A), amide I region of AS fibres (B), full spectra range of PS 4x fibres (C), and amide I region of PS 4x fibres (D).

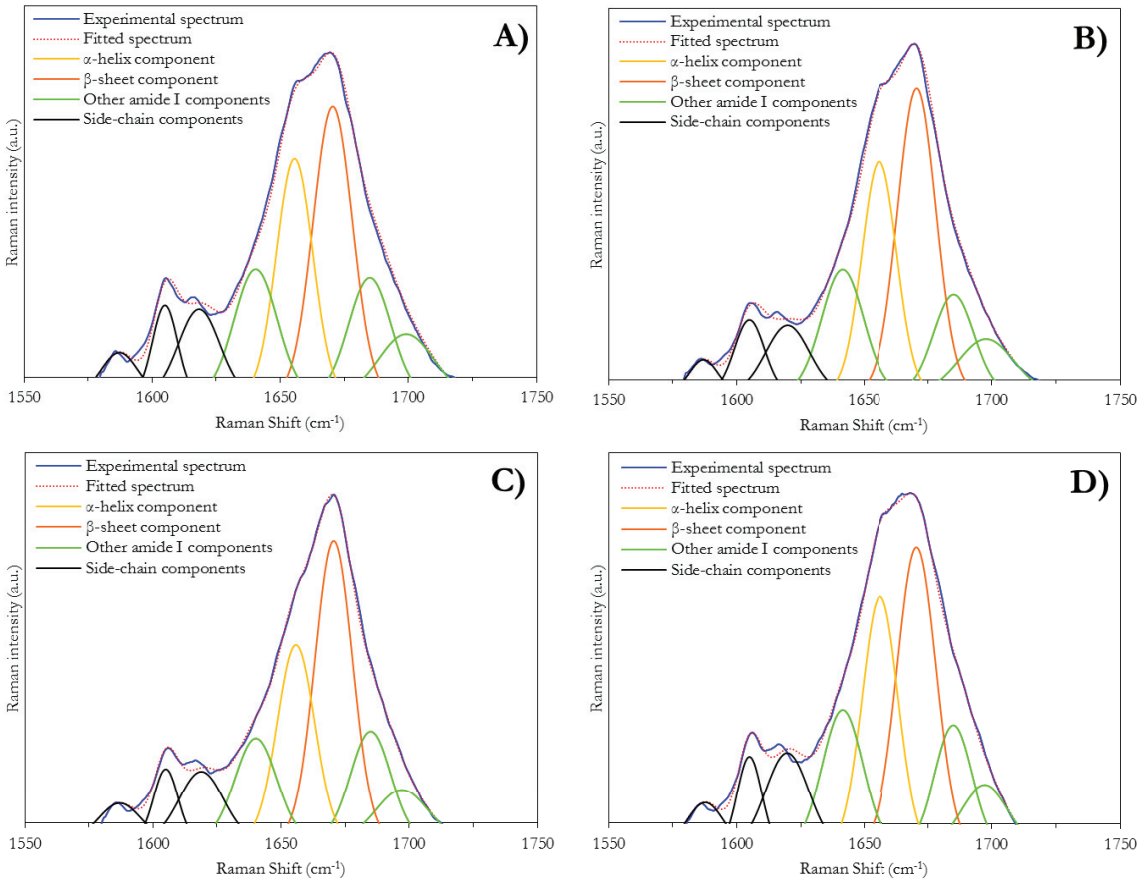

Figure 3.11 Decomposition of the amide I region of W_3 fibres spun from the TFA/TFE/H_2O spinning dope. Perpendicular orientation of AS fibres (A), parallel orientation of AS fibres (B), perpendicular orientation of PS 4x fibres (C), and parallel orientation of PS 4x fibres (D).

Table 3.3 Linking the position and assignment of the main Raman bands of native spider silks to W_3 fibres. Raman bands were identified (indicated by an "x") from Raman spectra generated for AS and PS 4x W_3 fibres spun from the HFIP/H_2O spinning dope (Figures 3.8A and 3.8C) or the TFA/TFE/H_2O spinning dope (Figures 3.10A and 3.10C).

Band position ($\pm$1 cm^{-1})[a]	**Assignment**	**HFIP/H_2O spinning dope**		**TFA/TFE/H_2O spinning dope**	
		AS fibres	PS 4x fibres	AS fibres	PS 4x fibres
525	Ala (α-helix)	x	x	x	x
621	Phe	x	x	x	x
642	Tyr	x	x	x	x
739	HFIP?[b]	x	-	-	-
748	Trp	?	-	-	-
829 and 851	Tyr	?	x	x	x
875	Pro	x[c]	x[c]	x[c]	x[c]
904	Polyalanine	x	x	x	x
922	Pro	x[c]	x[c]	x[c]	x[c]
939	α-helix	x[c]	x[c]	x[c]	x[c]
1003	Phe	x	x	x	x
1028	Phe	x	x	x	x
1045	Pro	x[c]	x[c]	x[c]	x[c]
1055	Ser	x[c]	x[c]	x[c]	x[c]
1083	Ser	x	x	x	x
1102 or 1105 (1094 and 1068)[d]	Skeletal C^{α}–C^{β} stretching	x	x	x	x
1126	Leu	x	x	x	x
1175	Tyr	x[c]	x[c]	x[c]	x[c]
1207	Tyr, Phe	x	x	x	x
1260 or 1273 (1242 and 1228)[d]	Amide III	x	x	x	x
1305 (1315)[d]	Ala	x[c]	x[c]	x[c]	x[c]
1335 (1339)[d]	Ala	x	x	x	x
1416	Gly	x[c]	x[c]	x[c]	x[c]
1452	CH_3 asymmetric bend, CH_2 bending	x	x	x	x
1550	Trp	-	-	-	-
1587	Phe	x	x	x	x
1603	Phe, Tyr-protonated form	x	x	x	x
1615	Tyr	x	x	x	x
1658 (1670)[d]	Amide I	x	x	x	x

[a] May vary depending on the type of spider silk and condition (native or artificial).
[b] No appropriate literature sources were available to confirm this assignment.
[c] Raman band is present, but not clearly resolved from neighbouring bands.
[d] Values in parenthesis correspond to a β-sheet conformation.

3.3.5 Surface Morphology Is Similar in Both PS Fibre Types

To observe morphological features of the surfaces of PS-stretched W_3 fibres, intermittent-contact AFM was employed. AFM micrographs of PS 4x W_3 fibres spun from each of the two spinning dopes can be seen in Figures 3.12 and 3.13, respectively. In both fibre types, the surface morphology at the nm-scale reveals a structural organization comprising spheroids (previously described in section 2.1.3.2) aligned in a fibrillar manner (Figures 3.12 and 3.13). Particularly when examining surface features of W_3 fibres spun from the HFIP/H_2O spinning dope (Figure 3.12), fibrillar structures are clear at the nm-scale level running parallel to fibre long axis. This morphology is not as apparent in the W_3 fibres spun from the TFA/TFE/H_2O spinning dope (Figure 3.13), which will be discussed in more detail shortly (section 3.3.7).

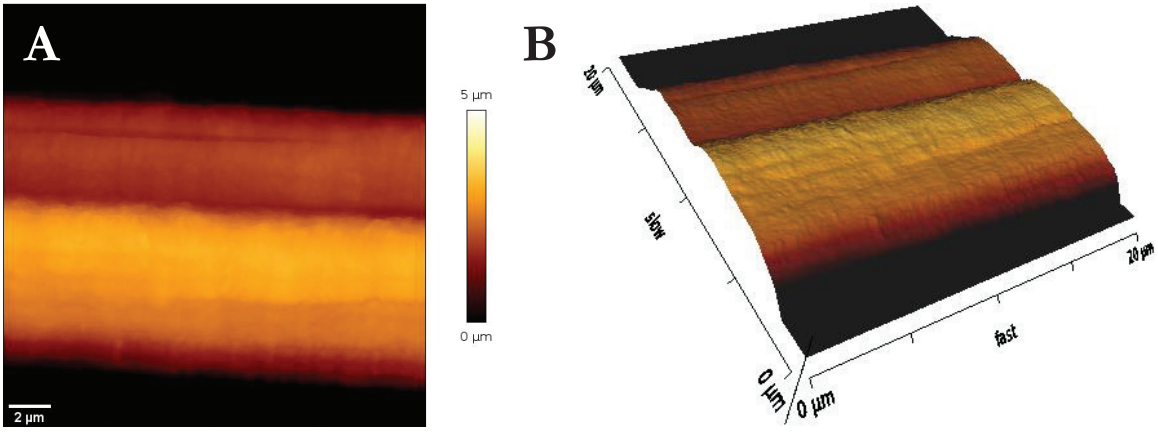

Figure 3.12 Representative AFM micrograph of W_3 fibres spun from the HFIP/H_2O spinning dope, observed by intermittent-contact mode. PS 4x fibre (colour scale for height is shown on the right) (A) and three-dimensional image with a 5 µm height trace shown for the same micrograph (B).

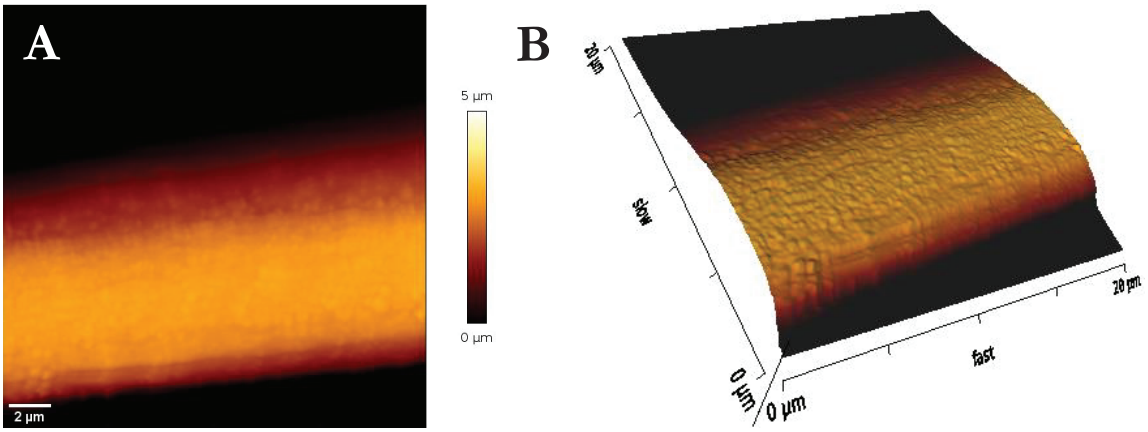

Figure 3.13 Representative AFM micrograph of W_3 fibres spun from the TFA/TFE/H_2O spinning dope, observed by intermittent-contact mode. PS 4x fibre (colour scale for height is shown on the right) (A) and three-dimensional image with a 5 µm height trace shown for the same micrograph (B).

3.3.6 Cross-Sections of W_3 Fibres Demonstrate That They Are Solid and Are Composed of Spheroids

In order to determine the internal morphology of AS and PS-stretched W_3 fibres, fibres were immersed in liquid nitrogen and broken to generate ends representative of a cross-section of the fibre. The resulting fibre ends were then examined by SEM, as shown in representative SEM micrographs AS and PS 4x W_3 fibres spun from either the HFIP/H_2O or the TFA/TFE/H_2O spinning dope in Figures 3.14 and 3.15, respectively. As with AFM, SEM clearly demonstrates that the W_3 fibres are solid in structure, primarily consisting of spheroids. In addition, it is apparent that, at least on the surface of PS 4x W_3 fibres spun from the TFA/TFE/H_2O spinning dope (Figure 3.15B), fibrils are formed from the W_3 protein along the fibre long axis.

In contrast to W_3 fibres spun from the TFA/TFE/H_2O spinning dope, small pores (typically ~1 µm in diameter) are visible on the surface of AS W_3 fibres spun from the HFIP/H_2O spinning dope (Figure 3.14A). Pores are also visible in the cross-section of these

fibres, but are less abundant. These pores may arise from residual solvent being retained in the fibre following wet-spinning, which could explain the presence of a distinct Raman band at ~739 cm^{-1} (Table 3.3) found only in Raman spectra of these fibres (Figure 3.8A). From these observations, it can be suggested that the pores may be due to degradation within the spinning dope. However, it is more likely that the pores may be a naturally occurring feature with wet-spinning W_3 fibres from the HFIP/H_2O spinning dope. Interestingly, in all cases, these pores were absent in PS 4x W_3 fibres (Figure 3.14B), which may be the result of both removal of residual solvent and/or additional compacting/assembly of spheroids, thereby displacing the holes. This will be discussed in more detail in the next section.

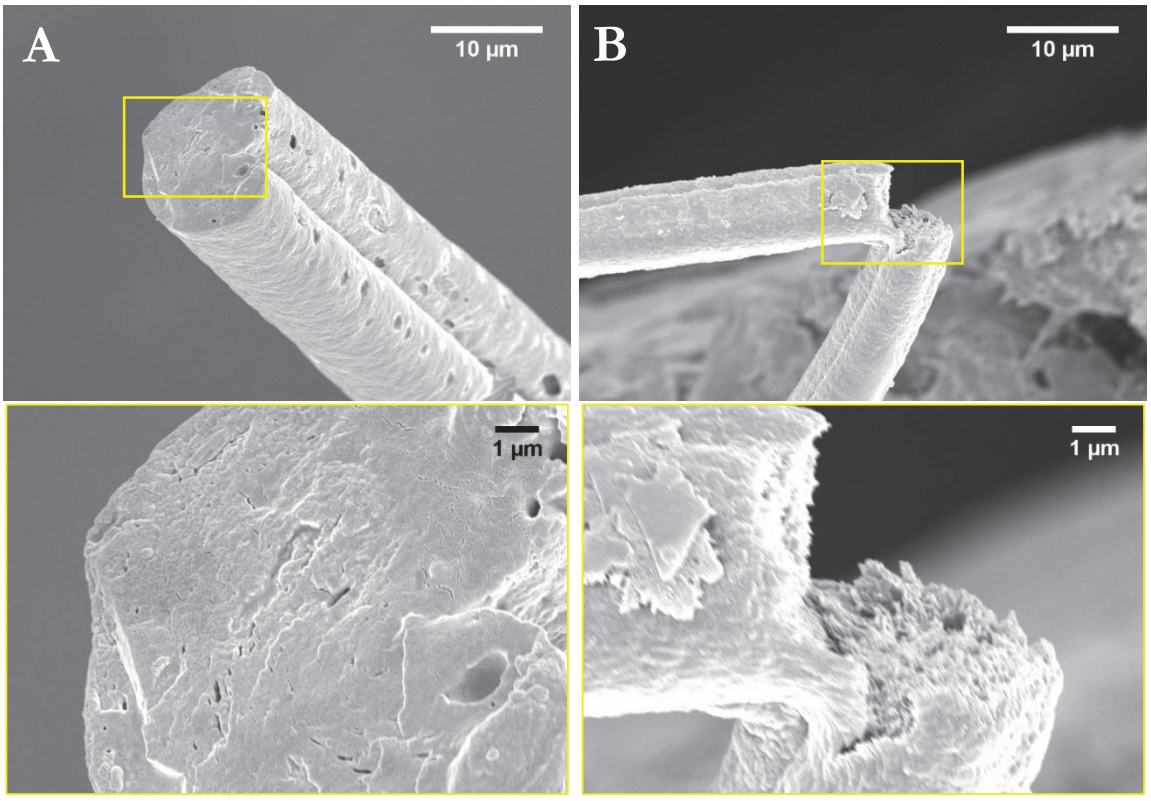

Figure 3.14 Representative SEM micrographs of W_3 fibres spun from the HFIP/H_2O spinning dope. All images represented are cross-sections of fibres following breakage in liquid nitrogen, where boxed regions in the bottom-left and the bottom-right correspond to increased magnifications of AS (A) and PS 4x fibres (B), respectively.

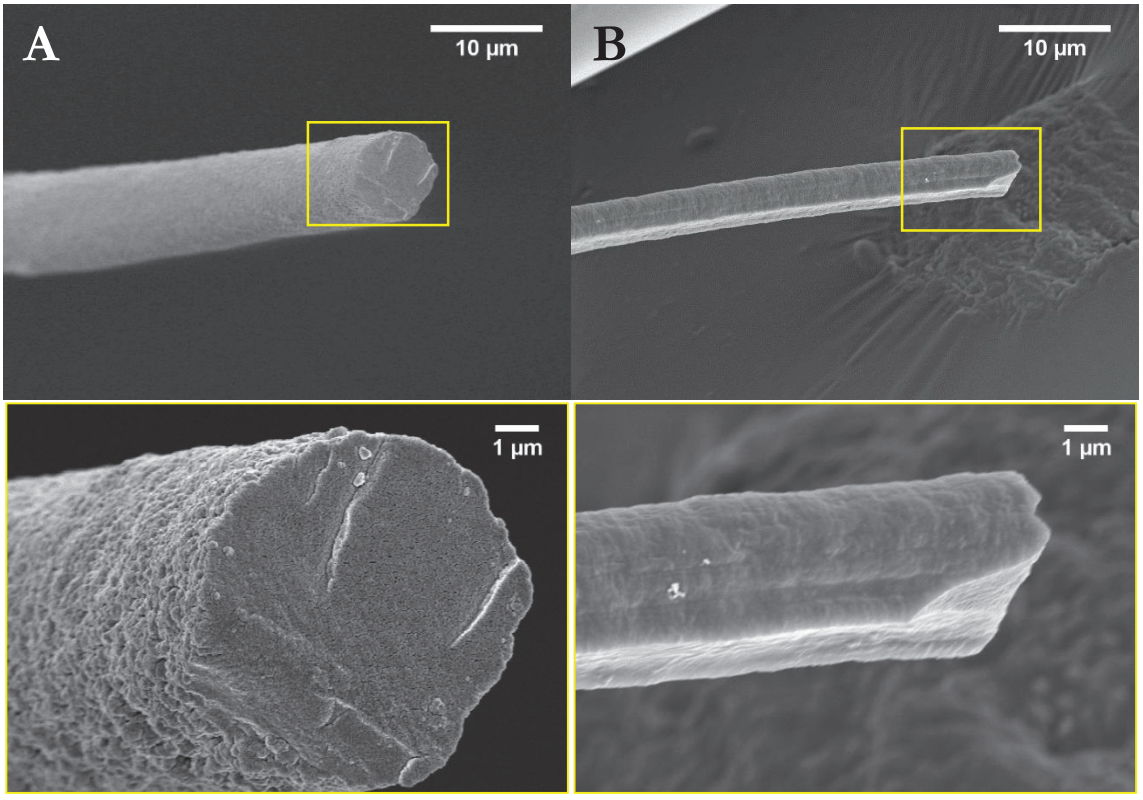

Figure 3.15 Representative SEM micrographs of the W_3 fibres spun from the TFA/TFE/H_2O spinning dope. All images represented are cross-sections of fibres following breakage in liquid nitrogen, where boxed regions in the bottom left and the bottom right correspond to increased magnifications of AS (A) and PS 4x fibres (B), respectively.

3.3.7 Correlating Fibre Morphology and Mechanical Properties

Having observed morphological features of the W_3 fibres, potential correlations between fibre morphology and mechanical properties will now be discussed. As mentioned previously, wet-spinning of fibres promotes shear flow rather than elongational flow. Because of this, it is likely that unfolding of the spheroids during fibre formation was partially hindered, resulting in more aggregation than self-assembly of the spheroids (102). Following post-spin stretching, it is likely that more unfolding and, possibly, self-assembly of spheroids could occur, resulting in the fibrillar structural features that were observed by AFM on the surface of the PS 4x W_3 fibres (Figures 3.12 and 3.13). If wet-spinning of these

fibres could promote elongational flow rather than shearing flow, then a more complete unfolding of the spheroids could occur, allowing for a different class of self-assembly and thereby resulting in more well-defined fibrillar structures, as seen in mechanically-drawn (21) and also in native silk fibres (105-107).

Before going further, it should be noted that, in contrast to the AFM micrographs, SEM micrographs revealed more apparent fibril features in the PS 4x W_3 fibres spun from the TFA/TFE/H_2O spinning dope (Figure 3.15B) compared to PS 4x W_3 fibres spun from the HFIP/H_2O spinning dope (Figure 3.14B). A possible explanation for this variation in surface features between both forms of microscopy may be due to environmental factors affecting image resolution. Specifically, it is known that humidity can have detrimental effects in the resolution of micrographs acquired by AFM, mainly because of its influence on the probe and its interaction with the sample (136). Alternatively, fibre morphology itself may change as a response to variations in humidity. These factors do not occur in SEM, since micrographs acquired using this method are under vacuum conditions (previously described in section 3.1.6). This may in part explain why surface features such fibrillar structures along the long axis of W_3 fibres spun from the TFA/TFE/H_2O spinning dope were more apparent in SEM micrographs (Figure 3.15B), but not as apparent in the AFM micrographs (Figure 3.13).

With that being said, when examined by SEM, there were differences observed in the internal morphology of AS and PS-stretched W_3 fibres spun from each of the two spinning dopes. Beyond the evident pore features visible on the surface of AS W_3 fibres spun from the HFIP/H_2O spinning dope (Figure 3.14A), they were also present within the ends representative of the cross-section. This may be the consequence of inadequate compacting/assembly of spheroids in the initial AS W_3 fibres. On the other hand, pores are

clearly not evident in W_3 fibres spun from the TFA/TFE/H_2O spinning dope. Rather, AS W_3 fibres from this particular spinning dope seem to begin with an already more uniform and compact structure of spheroids, which is likely favouring fibril assembly along the fibre long axis following a post-spin stretching treatment.

These observations may provide an explanation as to why the mechanical properties of these fibres are better than those of fibres formed from the HFIP/H_2O spinning dope. It can be speculated that the more compact spheroid structure in the initial AS W_3 fibres spun from the TFA/TFE/H_2O spinning dope implies that a more complete crystalline phase transition and alignment of α-helical components is occurring. By having a more complete transition in the initial AS fibre, this would require not only less energy to complete the stacking/aggregation of the already oriented crystalline β-sheets, but also promote a higher proportion of amorphicity around these regions, alongside additional alignment of the α-helical components. Both an increased stacking/aggregation of β-sheets and alignment of α-helical components correlates well to an increase in strength and to an increase in extensibility observed in the PS 4x W_3 fibres spun from the TFA/TFE/H_2O spinning dope relative to PS 4x W_3 fibres spun from the HFIP/H_2O spinning dope (Table 3.1).

3.4 Summary

Solubilization of W_3 protein in either HFIP/H_2O or TFA/TFE/H_2O produced spinning dopes that exhibited α-helical behaviour with minor spectral differences. Following wet-spinning, the mechanical strength of both fibre types was dramatically improved when subjected to a post-spin stretching treatment, which was correlated to an enrichment in β-sheet conformation alongside an increase in birefringence. The improved strength therefore seems likely to be attributable to increased hydrogen bonding that would be associated with stacking/aggregation of crystalline β-sheets within the W_3 fibres. In general, W_3 fibres spun

from the TFA/TFE/H_2O spinning dope were stronger, more extensible, and tougher than W_3 fibres spun from the HFIP/H_2O spinning dope. These differences likely result from changes in the protein behaviour in each spinning dope, with differences in compacting/assembly of spheroids when wet-spun into fibres. The overall improvement in mechanical properties seen in the W_3 fibres spun from the TFA/TFE/H_2O spinning dope was correlated to a more intense anisotropic effect in secondary structuring and greater birefringence relative to the W_3 fibres spun from the HFIP/H_2O spinning dope. This anisotropy is a clear indication that there is a preferential alignment of molecules relative to the fibre long axis. Increased extensibility in the PS 4x W_3 fibres spun from the TFA/TFE/H_2O spinning dope therefore appears to be correlated with an increased alignment of secondary structuring, possibly being attributable to the increased hydrogen bonding associated with aligned α-helical components within these fibres. Based upon the method developed in Chapter 2, coupled with characterization results reported in this chapter, extension of the wet-spinning method was carried out to incorporate an automated post-spin stretching step, as detailed in Chapter 4.

Chapter 4: Optimization of the Wet-Spinning Method by Incorporation of an Automated Post-Spin Stretching Step and Characterization of Fibres Spun From This Optimized Method

4.1 Introduction

This chapter builds upon the method development and materials characterization results reported in Chapters 2 and 3, respectively. In Chapter 2, I explained the process and development of a wet-spinning method for the artificial production of recombinant wrapping silk proteins into silk-like fibres. Chapter 3 detailed the characterization using a series of techniques to probe biophysical, mechanical, and morphological properties of these newly fabricated silk-like fibres. From these experimental results, I confirmed my hypothesis that a post-spin stretching treatment facilitates additional molecular alignment of protein secondary structure within the fibres, resulting in improved mechanical properties. In addition, after comparative characterization of both spinning dopes and fibres, it was observed that W_3 fibres spun from a TFA/TFE/H_2O spinning dope were stronger, more extensible, and tougher than W_3 fibres spun from an HFIP/H_2O spinning dope. Based upon this understanding, I report in this chapter my extension of the wet-spinning method to incorporate an automated post-spin stretching step. I then move on to demonstrate that the TFA/TFE/H_2O spinning dope can be successfully applied with the optimized wet-spinning method to spin W_3 fibres. Following this, I detail both the mechanical and morphological properties of these fibres.

4.2 Materials and Methods

4.2.1 Protein Expression, Purification, and Solubilization

Protein expression of H_6-SUMO-W_3, cleavage of H_6-SUMO, and purification of W_3 was carried out as described in Chapter 2 (section 2.2.1). Spinning dope solutions containing solubilized W_3 at ~10% (w/v) in 60% TFA/20% TFE/20% H_2O were prepared in the same manner as explained in Chapter 3 (section 3.2.1).

4.2.2 Fibre Formation Using Wet-Spinning Combined with Automated Post-Spin Stretching of AS Fibres

In order to allow for automated post-spin stretching of AS fibres, a new apparatus was designed and built (Figures 4.1 and 4.2) at the Department of Physics and Atmospheric Science Machine Shop (Dalhousie University; Halifax, NS). This was loosely based upon a device shown by R. Lewis and coworkers at Utah State University (online video no longer available), but employs significantly different components and design features. Fibre formation using the TFA/TFE/H_2O spinning dope for wet-spinning follows the protocol described in section 2.2.3, with two modifications. First, the dope was extruded at a constant speed of 10 μL/min instead of 16 μL/min. Second, the collector (referred to as roller #1 from this stage forward) was changed to a planar cylindrical aluminum roller and driven rotationally by a motor, rather than a pump, which was set at a constant speed equivalent to the extrusion rate. The wet-spinning method was combined with an automated post-spin stretching step (Figures 4.1 and 4.2). All rollers as shown in Figure 4.1A are driven rotationally by individual stepper motors (NEMA 17 Stepper Motor (Hong Kong); Figure 4.1B) so as to guide a given W_3 fibre circumferentially across a portion of their surface.

After the coagulated spinning dope forms the AS W_3 fibre in the coagulation bath, the AS fibre must be picked up by tweezers and guided onto the first set of rollers, and then onto the second set of rollers, with final collection on roller #6 (referred to as the collector at this point) to commence automated production/collection of PS-stretched W_3 fibres (step-by-step depiction in Figure 4.3). In this process, the AS W_3 fibre follows the path indicated in Figure 4.3 around the first set of rollers (rollers #1-3). After the AS W_3 fibre travels across the second roller, and as it travels across the third roller, it is soaked in a post-spin stretching bath (H_2O), contained within a vessel made from poly(methyl methacrylate). The post-spin stretching occurs while the fibre is in the post-spin stretching bath, between roller #3 and roller #4. This is achieved by controlling the speed of the second set of rollers, so that they rotate at a faster rate than the first set of rollers. The speed of the second set of rollers has been optimized to stretch the fibres to ~4x their original length, with a speed ratio of 4:1 (second set of rollers:first set of rollers). Following post-spin stretching, the PS-stretched W_3 fibre (now referred to as PS 4x W_3 fibre at this stage) travels around the fourth roller, across the fifth, and onto the collector. Collection of the PS 4x W_3 fibres occurs by continuously winding the fibre around the full circumference of the collector.

Rollers #1-2, and rollers #5-6 are planar cylindrical rollers, whereas rollers #3-4 are grooved (Figures 4.1A and 4.2). The planar cylindrical rollers have diameters of 6 cm, and lengths of 8 cm. The grooved rollers have a diameter of 6 cm in the middle of the grooved portion and 9 cm on the ends, with a length of 7 cm. As seen in Figures 4.1A and 4.2, rollers #1-6 are mounted in a configuration that allows the fibre to travel across the rollers in a zig-zag path. Although a simpler path could be imagined, zig-zagging allows for maintenance of tension in the fibre at all times and for greater surface contact of the fibre with the rollers.

As mentioned above, each roller is driven rotationally by an individual stepper motors. Both sets of stepper motors (i.e., motors #1-3 and motors #4-6 in sets) are separately controlled by a stepper motor driver (EasyDriver – Stepper Motor Driver A3967) interfaced through a SainSmart MEGA 2560 Board with an attached keypad (SainSmart LCD Keypad) and powered by an independent power supply (Super Power Supply® AC / DC Adapter Charger Cord; Output: 12V 3A) connected to a power source. Each keypad is used to control the corresponding set of stepper motors. A schematic of the stepper motor control system and roller locations is provided in Figure 4.1.

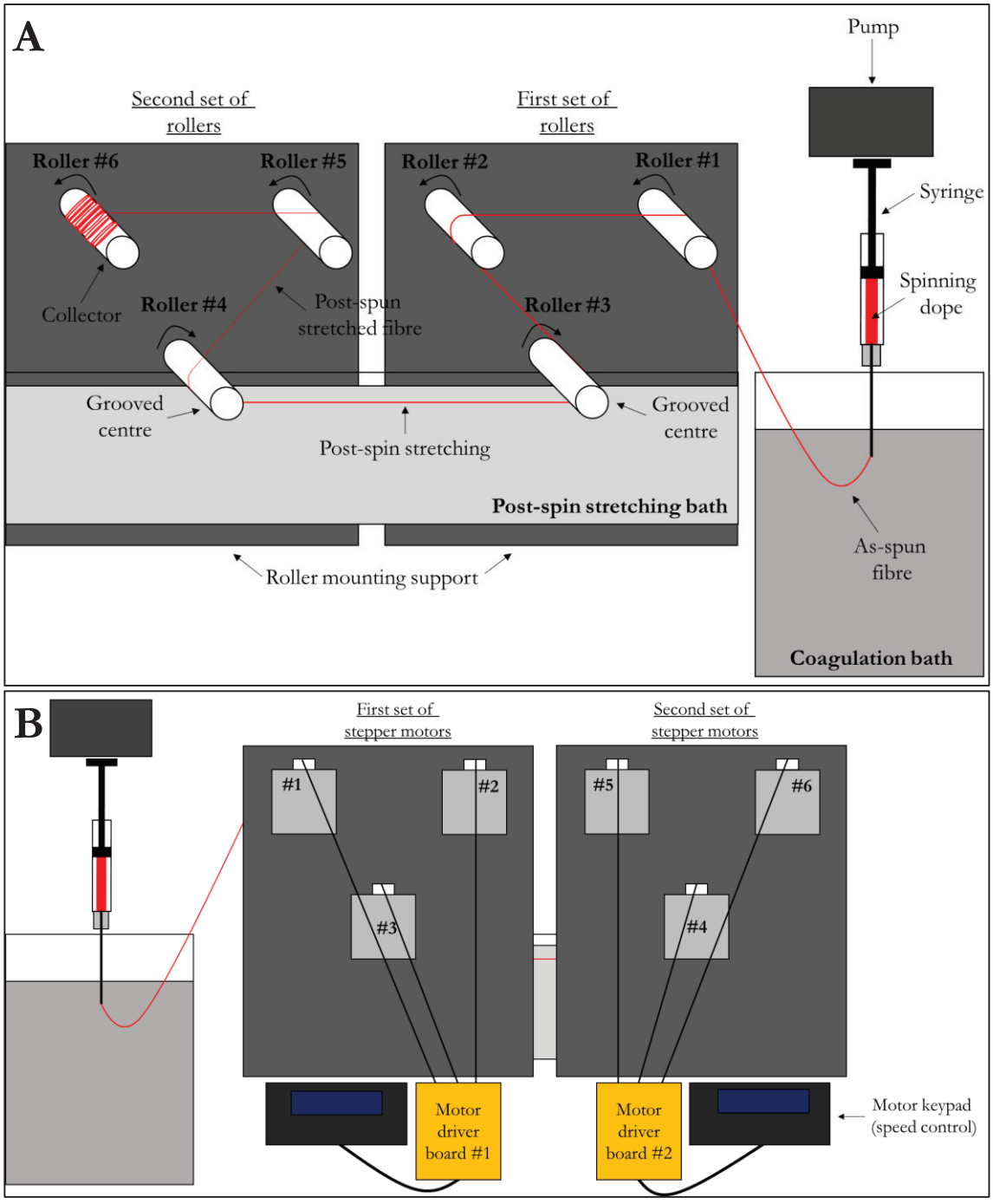

Figure 4.1 Schematic diagram of the optimized wet-spinning apparatus incorporating an automated post-spin stretching step. Front perspective view (A) and back perspective view (B) of the fibre spinning apparatus.

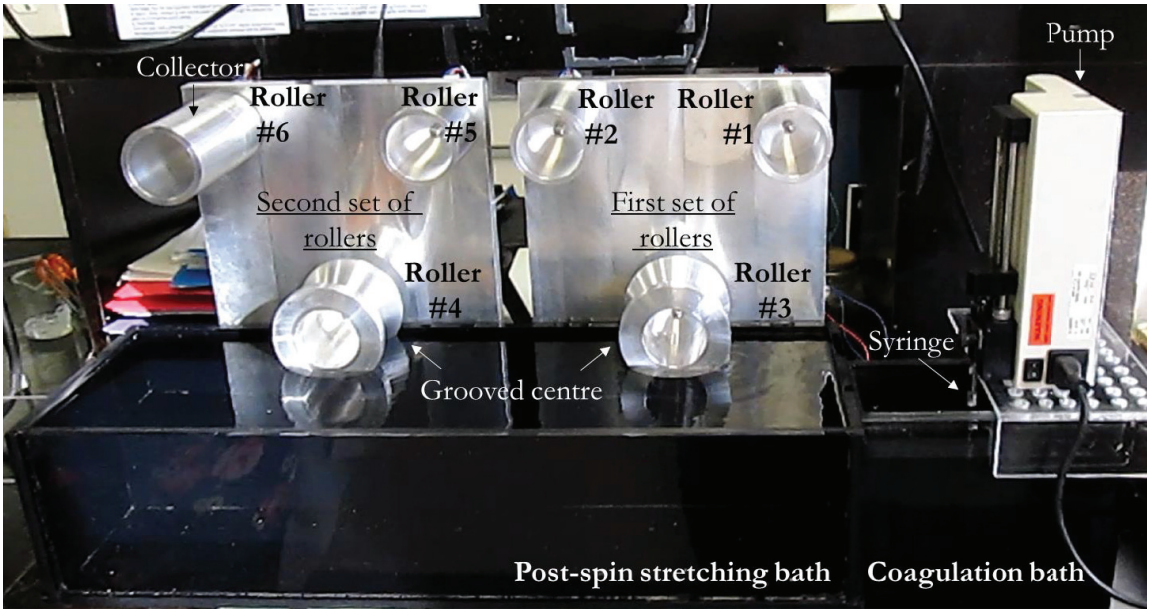

Figure 4.2 Photograph of the optimized wet-spinning apparatus incorporating an automated post-spin stretching step. This set-up consists of the same components used in the original wet-spinning fibre production method (section 2.2.3) in tandem with an automated post-spin stretching treatment. The first set of rollers guide the AS fibre into a post-spin stretching bath; the second set of rollers rotates at a faster speed, leading to fibre stretching in the bath with a smooth transition of the PS fibre onto the collector. Rollers #3 and #4 have a grooved centre in the post-spin stretching bath to promote proper alignment of the fibre when being stretched; all other rollers are cylindrical.

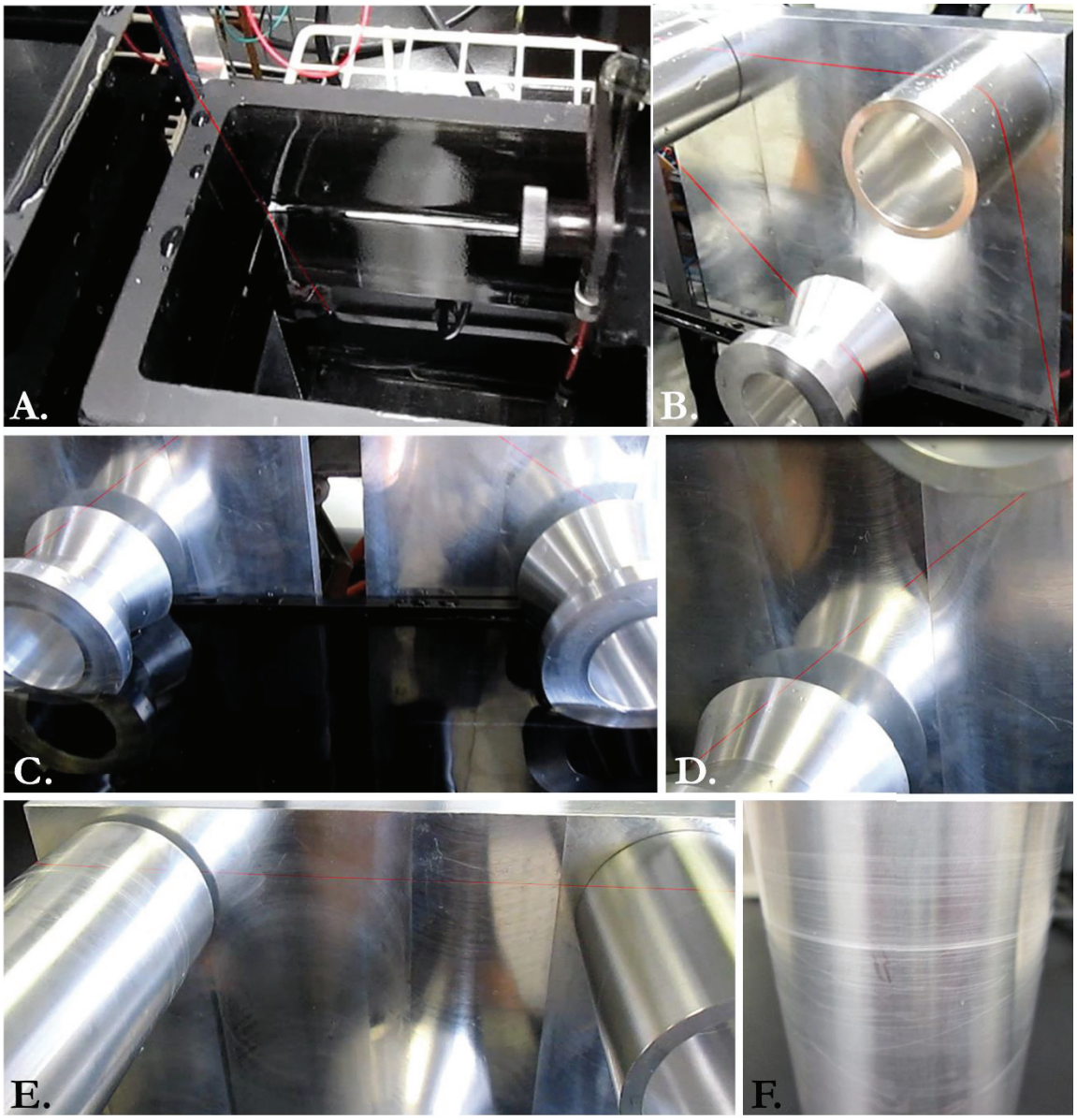

Figure 4.3 Step-by-step depiction of the process of recombinant spider wrapping silk protein fibre production using the optimized wet-spinning apparatus incorporating an automated post-spin stretching step. The initial transformation from the spinning dope into a fibre (represented in red) by shear extrusion into a coagulation bath (A) is followed by the guiding of the fibre onto the first set of rollers and into the post-spin stretching bath (B) leading to a smooth transition of the stretched fibre onto the second set of rollers (C), and continuous collection of the PS fibre at a constant speed (D & E) onto the final collector (F).

4.2.3 Characterization Techniques

Characterization was carried out with the same techniques used in Chapter 3. Fibre diameters were determined in the same manner (section 3.2.2), with mechanical testing of these fibres being performed using the second method (section 3.2.3). Birefringence was detected using polarized light microscopy, as described in section 3.2.4. Additionally, AFM and SEM imaging of fibres followed the same protocols as before (sections 3.2.6 and 3.2.7, respectively).

4.3 Results and Discussion

4.3.1 Mechanical Properties of W_3 Fibres Are Improved by Automated Post-Spin Stretching

Tensile testing was carried out on the automated PS-stretched W_3 fibres spun from the TFA/TFE/H_2O spinning dope allowing stress-strain curves to be produced and fibre mechanical properties to be determined. A representative stress-strain curve for fibres spun from this condition is provided in Figure 4.4, with mechanical properties reported in Table 4.1. As anticipated, mechanical behaviour of these fibres followed a similar trend relative to the manual PS-stretched W_3 fibres spun from the same spinning dope (Figure 3.5). Surprisingly, although these fibres followed this trend, strength improved almost two-fold, alongside an improvement in extensibility, which resulted in a more than two-fold increase in toughness. Specifically, an engineering stress of 250±31 MPa (vs. 139±27 MPa), engineering strain of 63±20% (vs. 47±21%), and toughness of 121±29 $MJ \cdot m^{-3}$ (vs. 59±33 $MJ \cdot m^{-3}$) (Tables 4.1 and 3.1) were found for the automated PS-stretched W_3 fibres (vs. manually PS-stretched W_3 fibres). Notably, the mechanical properties of the PS-stretched W_3 fibres

produced using this optimized method are closer to those of their native counterparts (Table 4.1).

There are many possible reasons as to why this dramatic improvement in mechanical properties of these fibres occurs. However, based on the findings observed and discussed in Chapter 3, it can be proposed that following wet-spinning and subsequent automated post-spin stretching of the AS fibre, perhaps a "smoother" structural transition is occurring within the fibre. Additionally, manual post-spin stretching is applied to a very short fibre, as opposed to automated post-spin stretching, which is applied to a long and continuous fibre. Beyond smooth and continuous extension of the fibre, water may provide the required hydrogen bond donor and acceptor functionality to stabilize the protein as it is being extended within the fibre. In turn, optimization of hydrogen bonding networks/geometry of the proteins would promote not only more compact stacking/aggregation of β-sheets, but also more complete alignment of α-helical components, following a similar line of thinking described in section 3.3.3. These phenomena may explain why there was an improvement in both strength and extensibility in PS-stretched W_3 fibres spun from the same spinning dope.

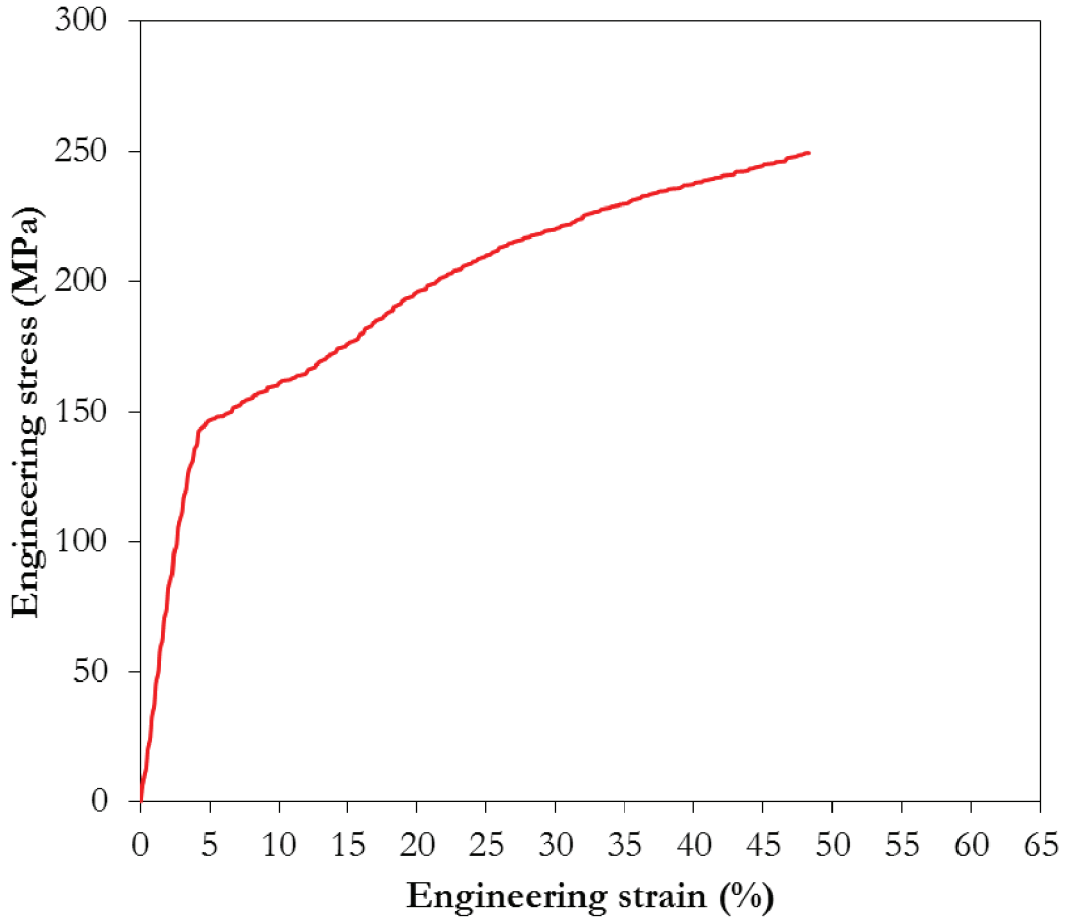

Figure 4.4 Representative stress-strain curve for PS 4x W_3 fibre spun from the optimized wet-spinning method. Stress-strain curve is shown for PS 4x W_3 fibres spun from TFA/TFE/H_2O spinning dope using the optimized wet-spinning method incorporating an automated post-spin stretching step.

Table 4.1 Mechanical properties of W_3 fibres spun from the TFA/TFE/H_2O spinning dope. Mechanical properties are also compared to the native full-length AcSp1 protein.

Protein origin	Recombinant protein or native protein	Spinning dope concentration (w/v %)	Engineering stress (MPa)	Engineering strain (%)	Young's modulus (GPa)	Toughness ($MJ \cdot m^{-3}$)	Diameter (μm)
AcSp1	W_3	~10[a]	250±31	63±20	4±1	121±29	9±1
AcSp1	W_3	~10[b]	AS: 61±7 PS 4x: 139±27	AS: 6±4 PS 4x: 47±21	AS: 2±1 PS 4x: 3±1	AS: 2±2 PS 4x: 59±33	AS: 20±4 PS 4x: 9±1
AcSp1 (13)	Native	N/A	687±56	86±3	10±1	376±39	0.4±0.01

[a] Spun using the optimized wet-spinning method, as detailed in the current chapter. Mechanical data are based on 10 fibres.

[b] Spun using the original wet spinning method, as detailed in Chapter 2. Mechanical data for AS and PS 4x are based on 6 fibres and 10 fibres, respectively.

4.3.2 Birefringence Suggests Improved Molecular Alignment by Automated Post-Spin Stretching

Given the drastic improvement in mechanical behaviour of the automated PS-stretched W_3 fibres spun from the TFA/TFE/H_2O spinning dope, it was essential to determine the degree of birefringence in these fibres. Polarized light micrographs of automated PS 4x W_3 fibres spun from the TFA/TFE/H_2O spinning dope are provided in Figure 4.5. As expected, these fibres did indeed exhibit birefringence. Notably, these produce a birefringent signal of larger magnitude relative to that observed for manual PS-stretched W_3 fibres spun from the same spinning dope. This implies that there is a higher degree of overall preferential molecular orientation and uniformity within these fibres, which correlates to the observed improvement in mechanical properties of these fibres.

Following from the previous discussion regarding the effects of manual PS-stretching of W_3 fibres (section 3.3.3), it is possible that automated PS-stretched W_3 fibres spun from the same spinning dope undergo a more complete crystalline phase transition. Following this rationale, the almost two-fold improvement in strength could be attributable to an increased β-sheet hydrogen bonding networks and more optimal β-sheet crystallite orientation within automated PS 4x W_3 fibres. The improvement in extensibility also seems likely to be correlated with an increased alignment of secondary structuring, which could be attributable to a higher degree of hydrogen bonding associated with an increased alignment of α-helical components within these fibres.

However, as described in the previous section, within this particular fibre condition it is clear that the improvement in strength is much higher than the improvement in extensibility. From this observation, it can be hypothesized that a mechanism may be occurring with simultaneous stacking/aggregation of crystalline β-sheets and alignment of

secondary structuring, particularly with alignment of the α-helical components. That is, from the soluble to fibrous state, enrichment of β-sheet microcrystal formation may be more energetically favourable and/or less complete in its initial transition compared to the alignment of α-helical components within the fibre. As was mentioned previously in section 3.3.2, in contrast to other silk types such as MA silk, which contains predominantly highly oriented β-sheets within the fibre (51), we know that the native wrapping silk fibre is moderately oriented with a mixture of β-sheets and α-helices (58). It has been suggested that the α-helical to β-sheet conversion from the soluble to fibrous state is not complete, thereby resulting in alignment of α-helical components along the fibre long axis (8). With this understanding, it is reasonable to suggest the previously mentioned simultaneous mechanism, where within these automated PS-stretched W_3 fibres a more complete transition may be occurring with stacking/aggregation of crystalline β-sheets. Following a similar line of thought from Chapter 3, an even more enriched environment of β-sheets within the fibre would correlate to improvement in mechanical strength whereas a less energetically favourable and/or an already more complete alignment of α-helical components within the fibre would correlate to the less dramatic improvement in extensibility of these fibres.

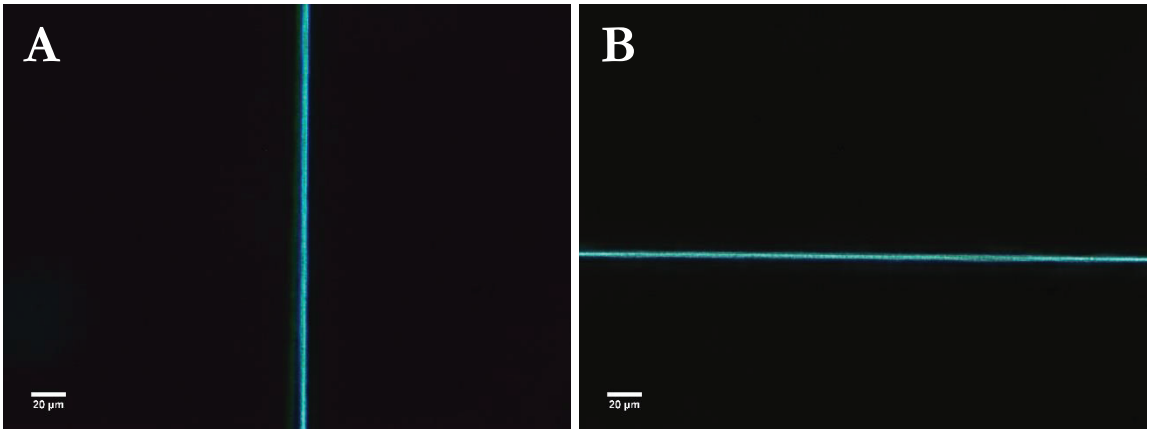

Figure 4.5 Birefringence of PS 4x W_3 fibres spun from the TFA/TFE/H_2O spinning dope using the optimized wet-spinning method. Birefringence was visualized by polarized light microscopy in both a vertical direction (A) and a horizontal direction (B).

4.3.3 Surface Morphology and Cross-Sections of W_3 Fibres Demonstrate Well-Defined Fibril Structural Features Along the Fibre

To observe morphological features of the surface of automated PS-stretched W_3 fibres spun from the TFA/TFE/H_2O spinning dope, both intermittent-contact AFM and SEM were employed. Representative AFM and SEM micrographs of these fibres can be seen in Figures 4.6 and 4.7, respectively. Additionally, surface and internal morphology alongside cross-sectional images at fibre ends were observed after either being broken (Figure 4.7A) or after mechanical rupturing by tensile testing (Figure 4.7B).

As with manual PS-stretched W_3 fibres spun from the same spinning dope, these fibres are solid in structure, consisting of spheroids within the fibre formed from the W_3 protein. Furthermore, there is no evidence of pores in these fibres. However, compared to the manual PS-stretched W_3 fibres, it is evident that in the automated PS-stretched W_3 fibres, they have better-defined fibril structures at the nm-scale level running parallel to the fibre axis, as observed by AFM (Figure 4.6) and SEM (Figure 4.7A). After being mechanically ruptured, the observable fibril substructure on the surface of these fibres remains intact, with

an apparently increased dispersion of spheroids at the ruptured fibre end (Figure 4.7B). The latter may be a typical morphological feature along the fibre axis after being mechanically ruptured, or it may be localized only to that particular region. Specifically, when subjected to mechanical stress, mechanical rupture at a given point along the fibre may introduce heat into the system, thereby disfiguring the spheroids at the region that is ruptured.

Having observed these morphological features for automated PS-stretched W_3 fibres, it is apparent that the distinguishing feature of these fibres is a well-defined fibrillar structure running parallel to the fibre axis with obvious presence of spheroidal components. The better defined fibrillar substructuring relative to manual post-spin stretching is likely the result of adding an automated post-spin stretching step, permitting a smoother and more uniform structural transition within the fibre, as described in section 4.3.1. In turn, this may promote additional unfolding and entangling of spheroids, thereby allowing for a different class of self-assembly than is seen manually stretched W_3 fibres from the same spinning dope. Subsequently, the different class of self-assembly may provide more potential energy for the system, resulting in a more complete crystalline phase transition by more complete stacking/aggregation of crystalline β-sheets, as well as alignment of secondary structuring, including the α-helical components. This may also explain the dramatic improvement in mechanical properties such as strength, extensibility, and toughness in these fibres.

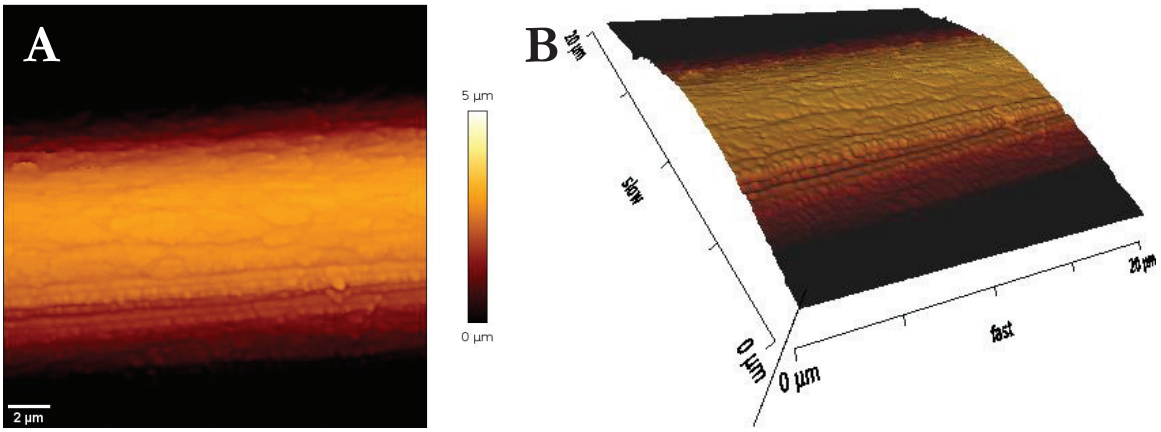

Figure 4.6 Representative AFM micrograph of PS 4x W_3 fibres spun from the TFA/TFE/H_2O spinning dope using the optimized wet-spinning method, observed by intermittent-contact mode. Fibre (colour scale for height is shown on the right) (A) and three dimensional image with a 5 um height trace shown for the same micrograph (B).

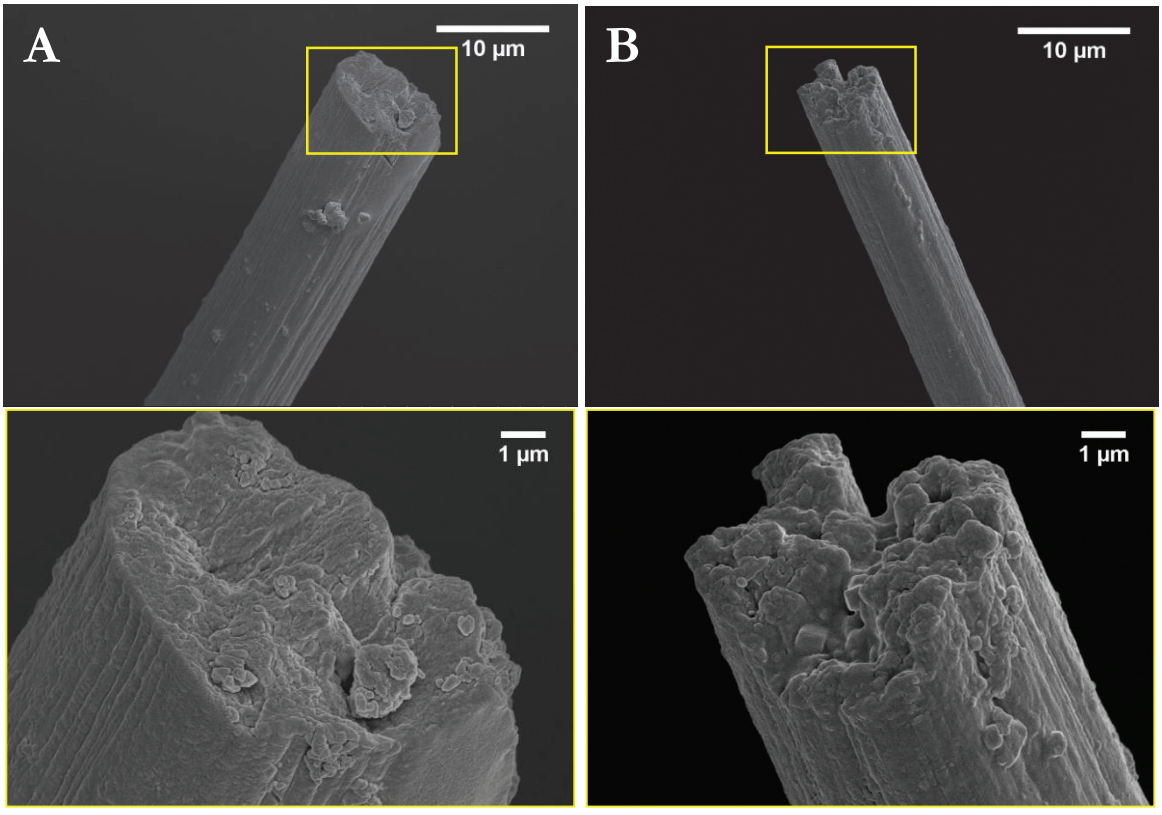

Figure 4.7 Representative SEM micrographs of PS 4x W_3 fibres spun from the TFA/TFE/H_2O spinning dope using the optimized wet-spinning method. Fibre cross-sections were examined either following breakage in liquid nitrogen (A) or following mechanical rupture (B). Boxed regions of fibres in panels A and B are shown at higher magnifications in the bottom left and bottom right, respectively.

4.4 Summary

After confirming my hypothesis in Chapter 3 that a post-spin stretching treatment would improve mechanical properties of W_3 fibres, the wet-spinning method developed in Chapter 2 was optimized to incorporate an automated post-spin stretching step. Utilizing this optimized wet-spinning method, W_3 fibres were successfully spun from the TFA/TFE/H_2O spinning dope. Surprisingly, these fibres were stronger, more extensible, and tougher than the manual PS-stretched W_3 fibres spun from the same spinning dope. These dramatic improvements in mechanical properties are likely the result of incorporating an automated post-spin stretching step, thereby permitting more water retention within the fibre and allowing for a smoother structural transition to take place. The overall improvement in mechanical properties observed in the automated PS-stretched W_3 fibres was correlated to greater birefringence relative to the manual PS-stretched W_3 fibres spun from the same spinning dope. The resulting increase in optical anisotropy is a clear indication that there is a higher degree of preferential molecular orientation and uniformity within these fibres. Additionally, morphological characterization of these fibres demonstrated a better-defined fibrillar substructure running parallel to the fibre long axis. The observed improvement in mechanical properties, greater birefringence, and well-defined fibrillar substructure may be correlated to a different class of self-assembly of the spheroids within these W_3 fibres. This in turn may have resulted in a more complete stacking/aggregation of crystalline β-sheets, as well as improved alignment of secondary structuring. Therefore, the improved strength and extensibility seems likely to be attributable to increased hydrogen bonding that would be associated with stacking/aggregation of crystalline β-sheets and alignment of α-helical components within the automated PS-stretched W_3 fibres spun from the TFA/TFE/H_2O spinning dope.

Chapter 5: Conclusion

The aim of this work was to develop and optimize an automated fibre production method for recombinant spider wrapping silk. This was followed by characterization of the biophysical, mechanical, and morphological properties of fibres produced using this method. With the results generated and presented in the previous chapters, I have provided new knowledge of wrapping silk fibre formation and structure, and have allowed for automated production of fibres for future study using solid-state nuclear magnetic resonance spectroscopy, which will make possible the first atomic-level characterization of a spider wrapping silk fibre.

5.1 Future Directions

Although information was provided about the overall secondary structure of W_3 in each spinning dope prior to spinning fibres, other aspects of the spinning dopes can be studied to gain a better understanding of how W_3 may behave differently in each spinning dope prior to fibre spinning. One approach would be to characterize the aggregation state of W_3 in each spinning dope through dynamic light scattering. Another approach would be to observe the morphology of W_3 spidroins within each spinning dope by SEM and/or AFM, which would provide more information about the spidroin state preceding wrapping silk fibre formation and improved understanding of the differences between dope environments.

Beyond the spinning dope, while information was provided on conformational changes in protein secondary structure and overall molecular orientation within these fibres, it would be valuable to obtain quantitative information about protein secondary structure content and molecular orientation. Two methods that could be used to address this are polarized Raman spectromicroscopy and IR vibrational spectroscopy/spectromicroscopy. Additionally, X-ray

diffraction could be used to examine crystalline content and orientation. If employed, these methods would not only allow for more accurate information on β-sheet and α-helical content of W_3 fibres, but they would allow for a more accurate interpretation of the degree and directionality of orientation of secondary structural units within these fibres. With these methods in mind, it would also be worthwhile to observe what structural and orientational changes may occur within these fibres after being mechanically ruptured upon subjection to mechanical load.

Beyond structural characterization, another potential direction for this work would be to further improve the mechanical behaviour of these fibres. Many approaches can be taken to address this, including modifying the spinning dope solvent mixture or increasing the spinning dope concentration. As well, new components could be incorporated into the spinning dope, for instance, metal ions such as aluminum (Al^{3+}), titanium (Ti^{3+} or Ti^{4+}), iron (Fe^{2+} or Fe^{3+}), or zinc (Zn^{2+}). Larger protein constructs or modifications of the W_3 construct could be attempted, but with the caveat that the spinning dopes optimized and detailed in this work may need to be further modified to appropriately solubilize and spin fibres from these proteins. Besides modifying spinning dope content and utilizing different protein constructs, attempting different post-spin stretching ratios may also be worthwhile.

Bibliography

1. Vollrath, F. (1992) Spider Webs and Silks. *Sci Am 266*, 70-76.

2. Lewis, R. V. (2006) Spider Silk: Ancient Ideas for New Biomaterials. *Chem Rev 106*, 3762-3774.

3. Borkner, C. B., Elsner, M. B., and Scheibel, T. (2014) Coatings and Films Made of Silk Proteins. *ACS Appl Mater Interfaces 6*, 15611-15625.

4. Fu, C., Shao, Z., and Fritz, V. (2009) Animal Silks: Their Structures, Properties and Artificial Production. *Chem Commun (Camb)*, 6515-6529.

5. Rising, A., and Johansson, J. (2015) Toward Spinning Artificial Spider Silk. *Nat Chem Biol 11*, 309-315.

6. Omenetto, F. G., and Kaplan, D. L. (2010) New Opportunities for an Ancient Material. *Science 329*, 528-531.

7. Hayashi, C. Y., and Lewis, R. V. (1998) Evidence from Flagelliform Silk cDNA for the Structural Basis of Elasticity and Modular Nature of Spider Silks. *J Mol Biol 275*, 773-784.

8. Lefèvre, T., Boudreault, S., Cloutier, C., and Pezolet, M. (2011) Diversity of Molecular Transformations Involved in the Formation of Spider Silks. *J Mol Biol 405*, 238-253.

9. Vollrath, F., and Knight, D. P. (2001) Liquid Crystalline Spinning of Spider Silk. *Nature 410*, 541-548.

10. Moon, M. J. (2012) Organization of the Spinnerets and Spigots in the Orb Web Spider, Argiope Bruennichi (Araneae: Araneidae). *Entomol Res 42*, 85-93.

11. Andersson, M., Holm, L., Ridderstrale, Y., Johansson, J., and Rising, A. (2013) Morphology and Composition of the Spider Major Ampullate Gland and Dragline Silk. *Biomacromolecules 14*, 2945-2952.

12. Ayoub, N. A., Garb, J. E., Tinghitella, R. M., Collin, M. A., and Hayashi, C. Y. (2007) Blueprint for a High-Performance Biomaterial: Full-Length Spider Dragline Silk Genes. *PLoS One 2*, e514.

13. Hayashi, C. Y., Blackledge, T. A., and Lewis, R. V. (2004) Molecular and Mechanical Characterization of Aciniform Silk: Uniformity of Iterated Sequence Modules in a Novel Member of the Spider Silk Fibroin Gene Family. *Mol Biol Evol 21*, 1950-1959.

14. Andersson, M., Chen, G., Otikovs, M., Landreh, M., Nordling, K., Kronqvist, N., Westermark, P., Jornvall, H., Knight, S., Ridderstrale, Y., Holm, L., Meng, Q., Jaudzems, K., Chesler, M., Johansson, J., and Rising, A. (2014) Carbonic Anhydrase Generates CO_2 and H^+

That Drive Spider Silk Formation Via Opposite Effects on the Terminal Domains. *PLoS Biol 12*, e1001921.

15. Rising, A. (2014) Controlled Assembly: A Prerequisite for the Use of Recombinant Spider Silk in Regenerative Medicine? *Acta Biomater 10*, 1627-1631.

16. Hijirida, D. H., Do, K. G., Michal, C., Wong, S., Zax, D., and Jelinski, L. W. (1996) ^{13}C NMR of Nephila Clavipes Major Ampullate Silk Gland. *Biophys J 71*, 3442-3447.

17. Chen, X., Knight, D. P., and Vollrath, F. (2002) Rheological Characterization of Nephila Spidroin Solution. *Biomacromolecules 3*, 644-648.

18. Jin, H. J., and Kaplan, D. L. (2003) Mechanism of Silk Processing in Insects and Spiders. *Nature 424*, 1057-1061.

19. Eisoldt, L., Hardy, J. G., Heim, M., and Scheibel, T. R. (2010) The Role of Salt and Shear on the Storage and Assembly of Spider Silk Proteins. *J Struct Biol 170*, 413-419.

20. Heidebrecht, A., Eisoldt, L., Diehl, J., Schmidt, A., Geffers, M., Lang, G., and Scheibel, T. (2015) Biomimetic Fibers Made of Recombinant Spidroins with the Same Toughness as Natural Spider Silk. *Adv Mater 27*, 2189-2194.

21. Xu, L., Rainey, J. K., Meng, Q., and Liu, X. Q. (2012) Recombinant Minimalist Spider Wrapping Silk Proteins Capable of Native-Like Fiber Formation. *PLoS One 7*, e50227.

22. Askarieh, G., Hedhammar, M., Nordling, K., Saenz, A., Casals, C., Rising, A., Johansson, J., and Knight, S. D. (2010) Self-Assembly of Spider Silk Proteins Is Controlled by a pH-Sensitive Relay. *Nature 465*, 236-238.

23. Hagn, F., Eisoldt, L., Hardy, J. G., Vendrely, C., Coles, M., Scheibel, T., and Kessler, H. (2010) A Conserved Spider Silk Domain Acts as a Molecular Switch That Controls Fibre Assembly. *Nature 465*, 239-242.

24. Hayashi, C. Y., Shipley, N. H., and Lewis, R. V. (1999) Hypotheses That Correlate the Sequence, Structure, and Mechanical Properties of Spider Silk Proteins. *Int J Biol Macromol 24*, 271-275.

25. Römer, L., and Scheibel, T. (2008) The Elaborate Structure of Spider Silk: Structure and Function of a Natural High Performance Fiber. *Prion 2*, 154-161.

26. Gosline, J. M., Guerette, P. A., Ortlepp, C. S., and Savage, K. N. (1999) The Mechanical Design of Spider Silks: From Fibroin Sequence to Mechanical Function. *J Exp Biol 202*, 3295-3303.

27. Blackledge, T. A., and Hayashi, C. Y. (2006) Silken Toolkits: Biomechanics of Silk Fibers Spun by the Orb Web Spider Argiope Argentata (Fabricius 1775). *J Exp Biol 209*, 2452-2461.

28. Denny, M. (1976) Physical-Properties of Spiders Silk and Their Role in Design of Orb-Webs. *J Exp Biol 65*, 483-506.

29. Kohler, T., and Vollrath, F. (1995) Thread Biomechanics in the 2 Orb-Weaving Spiders Araneus-Diadematus (Araneae, Araneidae) and Uloborus-Walckenaerius (Araneae, Uloboridae). *J Exp Zool 271*, 1-17.

30. Stauffer, S. L., Coguill, S. L., and Lewis, R. V. (1994) Comparison of Physical-Properties of 3 Silks from Nephila-Clavipes and Araneus-Gemmoides. *J Arachnol 22*, 5-11.

31. Perez-Riguero, J., Elices, M., Llorca, J., and Viney, C. (2001) Tensile Properties of Argiope Trifasciata Drag Line Silk Obtained from the Spider's Web. *J Appl Polym Sci 82*, 2245-2251.

32. Work, R. W. (1977) Dimensions, Birefringences, and Force-Elongation Behavior of Major and Minor Ampullate Silk Fibers from Orb-Web-Spinning Spiders - Effects of Wetting on These Properties. *Text Res J 47*, 650-662.

33. Xu, M., and Lewis, R. V. (1990) Structure of a Protein Superfiber: Spider Dragline Silk. *Proc. Natl. Acad. Sci. 87*, 7120-7124.

34. Hinman, M. B., and Lewis, R. V. (1992) Isolation of a Clone Encoding a Second Dragline Silk Fibroin. Nephila Clavipes Dragline Silk Is a Two-Protein Fiber. *J. Biol. Chem 267*, 19320-19324.

35. Guerette, P. A., Ginzinger, D. G., Weber, B. H. F., and Gosline, J. M. (1996) Silk Properties Determined by Gland-Specific Expression of a Spider Fibroin Gene Family. *Science 272*, 112-115.

36. Beckwitt, R., and Arcidiacono, S. (1994) Sequence Conservation in the C-Terminal Region of Spider Silk Proteins (Spidroin) from Nephila-Clavipes (Tetragnathiadae) and Araneus Bicentenarius (Araneidae). *J. Biol. Chem 269*, 6661-6663.

37. Gaines, W. A. I., and Marcotte, W. R., Jr. (2008) Identification and Characterization of Multiple Spidroin 1 Genes Encoding Major Ampullate Silk Proteins in Nephila Clavipes. *Insect Molecular Biology 17*, 465-474.

38. Rising, A., Hjälm, G., Engström, W., and Johansson, J. (2006) N-Terminal Nonrepetitive Domain Common to Dragline, Flagelliform, and Cylindriform Spider Silk Proteins. *Biomacromolecules 7*, 3120-3124.

39. Motriuk-Smith, D., Smith, A., Hayashi, C. Y., and Lewis, R. V. (2005) Analysis of the Conserved N-Terminal Domains in Major Ampullate Spider Silk Proteins. *Biomacromolecules 6*, 3152-3159.

40. Hinman, M., Dong, Z., Xu, M., and Lewis, R. V. (1992) Spider Silk: A Mystery Starting to Unravel. *Results Probl Cell Differ 19*, 227-254.

41. Ittah, S., Michaeli, A., Goldblum, A., and Gat, U. (2007) A Model for the Structure of the C-Terminal Domain of Dragline Spider Silk and the Role of Its Conserved Cysteine. *Biomacromolecules 8*, 2768-2773.

42. Rising, A., Hjalm, G., Engstrom, W., and Johansson, J. (2006) N-Terminal Nonrepetitive Domain Common to Dragline, Flagelliform, and Cylindriform Spider Silk Proteins. *Biomacromolecules 7*, 3120-3124.

43. Blackledge, T. A., Kuntner, M., Marhabaie, M., Leeper, T. C., and Agnarsson, I. (2012) Biomaterial Evolution Parallels Behavioral Innovation in the Origin of Orb-Like Spider Webs. *Sci Rep 2*, 833.

44. Andersen, S. O. (1970) Amino Acid Composition of Spider Silks. *Comp Biochem Physiol 35*, 705-710.

45. Thiel, B. L., and Viney, C. (1996) Beta Sheets and Spider Silk. *Science 273*, 1480-1481.

46. Simmons, A. H., Michal, C. A., and Jelinski, L. W. (1996) Molecular Orientation and Two-Component Nature of the Crystalline Fraction of Spider Dragline Silk. *Science 271*, 84-87.

47. Perez-Rigueiro, J., Elices, M., Plaza, G. R., and Guinea, G. V. (2007) Similarities and Differences in the Supramolecular Organization of Silkworm and Spider Silk. *Macromolecules 40*, 5360-5365.

48. Sponner, A., Vater, W., Monajembashi, S., Unger, E., Grosse, F., and Weisshart, K. (2007) Composition and Hierarchical Organisation of a Spider Silk. *PLoS One 2*, e998.

49. Simmons, A., Ray, E., and Jelinski, L. W. (1994) Solid-State ^{13}C NMR of Nephila-Clavipes Dragline Silk Establishes Structure and Identity of Crystalline Regions. *Macromolecules 27*, 5235-5237.

50. Lefèvre, T., Rousseau, M. E., and Pezolet, M. (2007) Protein Secondary Structure and Orientation in Silk as Revealed by Raman Spectromicroscopy. *Biophys J 92*, 2885-2895.

51. Lefèvre, T., Boudreault, S., Cloutier, C., and Pezolet, M. (2008) Conformational and Orientational Transformation of Silk Proteins in the Major Ampullate Gland of Nephila Clavipes Spiders. *Biomacromolecules 9*, 2399-2407.

52. Hayashi, C. Y., and Lewis, R. V. (2000) Molecular Architecture and Evolution of a Modular Spider Silk Protein Gene. *Science 287*, 1477-1479.

53. Adrianos, S. L., Teulé, F., Hinman, M. B., Jones, J. A., Weber, W. S., Yarger, J. L., and Lewis, R. V. (2013) Nephila Clavipes Flagelliform Silk-Like GGX Motifs Contribute to Extensibility and Spacer Motifs Contribute to Strength in Synthetic Spider Silk Fibers. *Biomacromolecules 14*, 1751-1760.

54. Vasanthavada, K., Hu, X., Falick, A. M., La Mattina, C., Moore, A. M., Jones, P. R., Yee, R., Reza, R., Tuton, T., and Vierra, C. (2007) Aciniform Spidroin, a Constituent of Egg Case Sacs and Wrapping Silk Fibers from the Black Widow Spider Latrodectus Hesperus. *J Biol Chem 282*, 35088-35097.

55. Garb, J. E., Ayoub, N. A., and Hayashi, C. Y. (2010) Untangling Spider Silk Evolution with Spidroin Terminal Domains. *BMC Evol Biol 10*, 243.

56. Wang, S., Huang, W., and Yang, D. (2014) Structure and Function of C-Terminal Domain of Aciniform Spidroin. *Biomacromolecules 15*, 468-477.

57. Tremblay, M. L., Xu, L., Lefèvre, T., Sarker, M., Orrell, K. E., Leclerc, J., Meng, Q., Pezolet, M., Auger, M., Liu, X. Q., and Rainey, J. K. (2015) Spider Wrapping Silk Fibre Architecture Arising from Its Modular Soluble Protein Precursor. *Sci Rep 5*, 11502.

58. Rousseau, M. E., Lefèvre, T., and Pezolet, M. (2009) Conformation and Orientation of Proteins in Various Types of Silk Fibers Produced by Nephila Clavipes Spiders. *Biomacromolecules 10*, 2945-2953.

59. Bratzel, G., and Buehler, M. J. (2012) Sequence-Structure Correlations in Silk: Poly-Ala Repeat of N. Clavipes MaSp1 Is Naturally Optimized at a Critical Length Scale. *J Mech Behav Biomed Mater 7*, 30-40.

60. Zeplin, P. H., Maksimovikj, N. C., Jordan, M. C., Nickel, J., Lang, G., Leimer, A. H., Roemer, L., and Scheibel, T. (2014) Spider Silk Coatings as a Bioshield to Reduce Periprosthetic Fibrous Capsule Formation. *Adv Funct Mater 24*, 2658-2666.

61. An, B., Tang-Schomer, M. D., Huang, W., He, J., Jones, J. A., Lewis, R. V., and Kaplan, D. L. (2015) Physical and Biological Regulation of Neuron Regenerative Growth and Network Formation on Recombinant Dragline Silks. *Biomaterials 48*, 137-146.

62. Madsen, B., Shao, Z. Z., and Vollrath, F. (1999) Variability in the Mechanical Properties of Spider Silks on Three Levels: Interspecific, Intraspecific and Intraindividual. *Int J Biol Macromol 24*, 301-306.

63. Vollrath, F. (1999) Biology of Spider Silk. *Int J Biol Macromol 24*, 81-88.

64. Fahnestock, S. R., and Bedzyk, L. A. (1997) Production of Synthetic Spider Dragline Silk Protein in Pichia Pastoris. *Appl Microbiol Biotechnol 47*, 33-39.

65. Grip, S., Rising, A., Nimmervoll, H., Storckenfeldt, E., McQueen-Mason, S. J., Pouchkina-Stantcheva, N., Vollrath, F., Engstrom, W., and Fernandez-Arias, A. (2006) Transient Expression of a Major Ampullate Spidroin 1 Gene Fragment from Euprosthenops Sp in Mammalian Cells. *Cancer Genomics & Proteomics 3*, 83-87.

66. Lazaris, A., Arcidiacono, S., Huang, Y., Zhou, J. F., Duguay, F., Chretien, N., Welsh, E. A., Soares, J. W., and Karatzas, C. N. (2002) Spider Silk Fibers Spun from Soluble Recombinant Silk Produced in Mammalian Cells. *Science 295*, 472-476.

67. Huemmerich, D., Scheibel, T., Vollrath, F., Cohen, S., Gat, U., and Ittah, S. (2004) Novel Assembly Properties of Recombinant Spider Dragline Silk Proteins. *Curr Biol 14*, 2070-2074.

68. Albertson, A. E., Teulé, F., Weber, W., Yarger, J. L., and Lewis, R. V. (2014) Effects of Different Post-Spin Stretching Conditions on the Mechanical Properties of Synthetic Spider Silk Fibers. *J Mech Behav Biomed Mater 29*, 225-234.

69. An, B., Hinman, M. B., Holland, G. P., Yarger, J. L., and Lewis, R. V. (2011) Inducing Beta-Sheets Formation in Synthetic Spider Silk Fibers by Aqueous Post-Spin Stretching. *Biomacromolecules 12*, 2375-2381.

70. Gnesa, E., Hsia, Y., Yarger, J. L., Weber, W., Lin-Cereghino, J., Lin-Cereghino, G., Tang, S., Agari, K., and Vierra, C. (2012) Conserved C-Terminal Domain of Spider Tubuliform Spidroin 1 Contributes to Extensibility in Synthetic Fibers. *Biomacromolecules 13*, 304-312.

71. Lin, Z., Deng, Q., Liu, X. Y., and Yang, D. (2013) Engineered Large Spider Eggcase Silk Protein for Strong Artificial Fibers. *Adv Mater 25*, 1216-1220.

72. Teulé, F., Addison, B., Cooper, A. R., Ayon, J., Henning, R. W., Benmore, C. J., Holland, G. P., Yarger, J. L., and Lewis, R. V. (2012) Combining Flagelliform and Dragline Spider Silk Motifs to Produce Tunable Synthetic Biopolymer Fibers. *Biopolymers 97*, 418-431.

73. Teulé, F., Cooper, A. R., Furin, W. A., Bittencourt, D., Rech, E. L., Brooks, A., and Lewis, R. V. (2009) A Protocol for the Production of Recombinant Spider Silk-Like Proteins for Artificial Fiber Spinning. *Nat Protoc 4*, 341-355.

74. Xia, X. X., Qian, Z. G., Ki, C. S., Park, Y. H., Kaplan, D. L., and Lee, S. Y. (2010) Native-Sized Recombinant Spider Silk Protein Produced in Metabolically Engineered Escherichia Coli Results in a Strong Fiber. *Proc Natl Acad Sci U S A 107*, 14059-14063.

75. Menassa, R., Zhu, H., Karatzas, C. N., Lazaris, A., Richman, A., and Brandle, J. (2004) Spider Dragline Silk Proteins in Transgenic Tobacco Leaves: Accumulation and Field Production. *Plant Biotechnol J 2*, 431-438.

76. Scheller, J., Guhrs, K. H., Grosse, F., and Conrad, U. (2001) Production of Spider Silk Proteins in Tobacco and Potato. *Nat Biotechnol 19*, 573-577.

77. Zhang, Y., Hu, J., Miao, Y., Zhao, A., Zhao, T., Wu, D., Liang, L., Miikura, A., Shiomi, K., Kajiura, Z., and Nakagaki, M. (2008) Expression of EGFP-Spider Dragline Silk Fusion Protein in BmN Cells and Larvae of Silkworm Showed the Solubility Is Primary Limit for Dragline Proteins Yield. *Mol Biol Rep 35*, 329-335.

78. Teulé, F., Miao, Y. G., Sohn, B. H., Kim, Y. S., Hull, J. J., Fraser, M. J., Jr., Lewis, R. V., and Jarvis, D. L. (2012) Silkworms Transformed with Chimeric Silkworm/Spider Silk Genes Spin Composite Silk Fibers with Improved Mechanical Properties. *Proc Natl Acad Sci U S A 109*, 923-928.

79. Wen, H., Lan, X., Zhang, Y., Zhao, T., Wang, Y., Kajiura, Z., and Nakagaki, M. (2010) Transgenic Silkworms (Bombyx Mori) Produce Recombinant Spider Dragline Silk in Cocoons. *Mol Biol Rep 37*, 1815-1821.

80. Xu, H. T., Fan, B. L., Yu, S. Y., Huang, Y. H., Zhao, Z. H., Lian, Z. X., Dai, Y. P., Wang, L. L., Liu, Z. L., Fei, J., and Li, N. (2007) Construct Synthetic Gene Encoding Artificial Spider Dragline Silk Protein and Its Expression in Milk of Transgenic Mice. *Anim Biotechnol 18*, 1-12.

81. Jones, J. A., Harris, T. I., Tucker, C. L., Berg, K. R., Christy, S. Y., Day, B. A., Gaztambide, D. A., Needham, N. J., Ruben, A. L., Oliveira, P. F., Decker, R. E., and Lewis, R. V. (2015) More Than Just Fibers: An Aqueous Method for the Production of Innovative Recombinant Spider Silk Protein Materials. *Biomacromolecules 16*, 1418-1425.

82. Xu, L., Tremblay, M. L., Meng, Q., Liu, X. Q., and Rainey, J. K. (2012) 1h, 13c and 15n Nmr Assignments of the Aciniform Spidroin (AcSp1) Repetitive Domain of Argiope Trifasciata Wrapping Silk. *Biomol NMR Assign 6*, 147-151.

83. Arcidiacono, S., Mello, C. M., Butler, M., Welsh, E., Soares, J. W., Allen, A., Ziegler, D., Laue, T., and Chase, S. (2002) Aqueous Processing and Fiber Spinning of Recombinant Spider Silks. *Macromolecules 35*, 1262-1266.

84. Teulé, F., Furin, W. A., Cooper, A. R., Duncan, J. R., and Lewis, R. V. (2007) Modifications of Spider Silk Sequences in an Attempt to Control the Mechanical Properties of the Synthetic Fibers. *J Mater Sci 42*, 8974-8985.

85. Xu, L., Tremblay, M.-L., Orrell, K. E., Leclerc, J., Meng, Q., Liu, X.-Q., and Rainey, J. K. (2013) Nanoparticle Self-Assembly by a Highly Stable Recombinant Spider Wrapping Silk Protein Subunit. *FEBS Letters 587*, 3273-3280.

86. Panavas, T., Sanders, C., and Butt, T. R. (2009) Sumo Fusion Technology for Enhanced Protein Production in Prokaryotic and Eukaryotic Expression Systems. *Methods Mol Biol 497*, 303-317.

87. Tucker, C. L., Jones, J. A., Bringhurst, H. N., Copeland, C. G., Addison, J. B., Weber, W. S., Mou, Q., Yarger, J. L., and Lewis, R. V. (2014) Mechanical and Physical Properties of Recombinant Spider Silk Films Using Organic and Aqueous Solvents. *Biomacromolecules 15*, 3158-3170.

88. Wei, W., Zhang, Y. P., Zhao, Y. M., Shao, H. L., and Hu, X. C. (2012) Studies on the Post-Treatment of the Dry-Spun Fibers from Regenerated Silk Fibroin Solution: Post-Treatment Agent and Method. *Mater Design 36*, 816-822.

89. Ishizaka, H., Watanabe, Y., Ishida, K., and Fukumoto, O. (1989) Regenerated Silk Prepared from Ortho Phosphoric Acid Solution of Fibroin. *J Seric Sci Jpn 58*, 87-95.

90. Ki, C. S., Lee, K. H., Baek, D. H., Hattori, M., Urn, I. C., Ihm, D. W., and Park, Y. H. (2007) Dissolution and Wet Spinning of Silk Fibroin Using Phosphoric Acid/Formic Acid Mixture Solvent System. *Journal of Applied Polymer Science 105*, 1605-1610.

91. Yao, J. M., Masuda, H., Zhao, C. H., and Asakura, T. (2002) Artificial Spinning and Characterization of Silk Fiber from Bombyx Mori Silk Fibroin in Hexafluoroacetone Hydrate. *Macromolecules 35*, 6-9.

92. Altman, G. H., Diaz, F., Jakuba, C., Calabro, T., Horan, R. L., Chen, J., Lu, H., Richmond, J., and Kaplan, D. L. (2003) Silk-Based Biomaterials. *Biomaterials 24*, 401-416.

93. Rising, A., Widhe, M., Johansson, J., and Hedhammar, M. (2011) Spider Silk Proteins: Recent Advances in Recombinant Production, Structure-Function Relationships and Biomedical Applications. *Cell Mol Life Sci 68*, 169-184.

94. Sashina, E. S., Novoselov, N. P., and Heinemann, K. (2003) Dissolution of Silk Fibroin in N-Methylmorpholine-N-Oxide and Its Mixtures with Organic Solvents. *Russ J Appl Chem 76*, 128-131.

95. Ki, C. S., Lee, K. H., Baek, D. H., Hattori, M., Um, I. C., Ihm, D. W., and Park, Y. H. (2007) Dissolution and Wet Spinning of Silk Fibroin Using Phosphoric Acid/Formic Acid Mixture Solvent System. *J Appl Polym Sci 105*, 1605-1610.

96. Yu, Q., and Sun, C. (2015) A Three-Dimensional Multiporous Fibrous Scaffold Fabricated with Regenerated Spider Silk Protein/Poly(L-Lactic Acid) for Tissue Engineering. *J Biomed Mater Res A 103*, 721-729.

97. Yu, Q., Xu, S., Zhang, H., Gu, L., Xu, Y., and Ko, F. (2014) Structure-Property Relationship of Regenerated Spider Silk Protein Nano/Microfibrous Scaffold Fabricated by Electrospinning. *J Biomed Mater Res A 102*, 3828-3837.

98. Lang, G., Jokisch, S., and Scheibel, T. (2013) Air Filter Devices Including Nonwoven Meshes of Electrospun Recombinant Spider Silk Proteins. *J Vis Exp*, e50492.

99. Stephens, J. S., Fahnestock, S. R., Farmer, R. S., Kiick, K. L., Chase, D. B., and Rabolt, J. F. (2005) Effects of Electrospinning and Solution Casting Protocols on the Secondary Structure of a Genetically Engineered Dragline Spider Silk Analogue Investigated Via Fourier Transform Raman Spectroscopy. *Biomacromolecules 6*, 1405-1413.

100. Zhu, B., Li, W., Lewis, R. V., Segre, C. U., and Wang, R. (2015) E-Spun Composite Fibers of Collagen and Dragline Silk Protein: Fiber Mechanics, Biocompatibility, and Application in Stem Cell Differentiation. *Biomacromolecules 16*, 202-213.

101. Rammensee, S., Slotta, U., Scheibel, T., and Bausch, A. R. (2008) Assembly Mechanism of Recombinant Spider Silk Proteins. *Proc Natl Acad Sci U S A 105*, 6590-6595.

102. Heim, M., Keerl, D., and Scheibel, T. (2009) Spider Silk: From Soluble Protein to Extraordinary Fiber. *Angew Chem Int Ed Engl 48*, 3584-3596.

103. Zhang, F., Lu, Q., Yue, X., Zuo, B., Qin, M., Li, F., Kaplan, D. L., and Zhang, X. (2015) Regeneration of High-Quality Silk Fibroin Fiber by Wet Spinning from $CaCl_2$-Formic Acid Solvent. *Acta Biomater 12*, 139-145.

104. Shao, Z. Z., Vollrath, F., Yang, Y., and Thogersen, H. C. (2003) Structure and Behavior of Regenerated Spider Silk. *Macromolecules 36*, 1157-1161.

105. Miller, L. D., Putthanarat, S., Eby, R. K., and Adams, W. W. (1999) Investigation of the Nanofibrillar Morphology in Silk Fibers by Small Angle X-Ray Scattering and Atomic Force Microscopy. *Int J Biol Macromol 24*, 159-165.

106. Kane, D. M., Naidoo, N., and Staib, G. R. (2010) Atomic Force Microscopy of Orb-Spider-Web-Silks to Measure Surface Nanostructuring and Evaluate Silk Fibers Per Strand. *J Appl Phys 108*

107. Gould, S. A., Tran, K. T., Spagna, J. C., Moore, A. M., and Shulman, J. B. (1999) Short and Long Range Order of the Morphology of Silk from Latrodectus Hesperus (Black Widow) as Characterized by Atomic Force Microscopy. *Int J Biol Macromol 24*, 151-157.

108. Augsten, K., Muhlig, P., and Herrmann, C. (2000) Glycoproteins and Skin-Core Structure in Nephila Clavipes Spider Silk Observed by Light and Electron Microscopy. *Scanning 22*, 12-15.

109. van Beek, J. D., Hess, S., Vollrath, F., and Meier, B. H. (2002) The Molecular Structure of Spider Dragline Silk: Folding and Orientation of the Protein Backbone. *Proc Natl Acad Sci U S A 99*, 10266-10271.

110. Kuipers, B. J. H., and Gruppen, H. (2007) Prediction of Molar Extinction Coefficients of Proteins and Peptides Using Uv Absorption of the Constituent Amino Acids at 214 nm to Enable Quantitative Reverse Phase High-Performance Liquid Chromatography−Mass Spectrometry Analysis. *Journal of Agricultural and Food Chemistry 55*, 5445-5451.

111. Neuhoff, V., Stamm, R., Pardowitz, I., Arold, N., Ehrhardt, W., and Taube, D. (1990) Essential Problems in Quantification of Proteins Following Colloidal Staining with Coomassie Brilliant Blue Dyes in Polyacrylamide Gels, and Their Solution. *Electrophoresis 11*, 101-117.

112. Greenfield, N. J. (2006) Using Circular Dichroism Spectra to Estimate Protein Secondary Structure. *Nat Protoc 1*, 2876-2890.

113. Castiglioni, E., Biscarini, P., and Abbate, S. (2009) Experimental Aspects of Solid State Circular Dichroism. *Chirality 21* 28-36.

114. Kenney, J. M., Knight, D. P., Dicko, C., and Vollrath, F. (2002) *Linear and Circular Dichroism Can Help Us to Understand the Molecular Nature of Spider Silk*, Aarhus University Press

115. Sreerama, N., and Woody, R. W. (2004) Computation and Analysis of Protein Circular Dichroism Spectra. *Methods Enzymol 383*, 318-351.

116. Callister, W. D., and Rethwisch, D. G. (2014) *Materials Science and Engineering: An Introduction*, Wiley; 9th edition, Toronto

117. Howie, A. J., Brewer, D. B., Howell, D., and Jones, A. P. (2007) Physical Basis of Colors Seen in Congo Red-Stained Amyloid in Polarized Light. *Lab Invest 88*, 232-242.

118. Um, I. C., Kweon, H., Lee, K. G., Ihm, D. W., Lee, J. H., and Park, Y. H. (2004) Wet Spinning of Silk Polymer I. Effect of Coagulation Conditions on the Morphological Feature of Filament. *Int J Biol Macromol 34*, 89-105.

119. Sun, M. J., Zhang, Y. P., Zhao, Y. M., Shao, H. L., and Hu, X. C. (2012) The Structure-Property Relationships of Artificial Silk Fabricated by Dry-Spinning Process. *J Mater Chem 22*, 18372-18379.

120. Cronin-Golomb, M., Murphy, A. R., Mondia, J. P., Kaplan, D. L., and Omenetto, F. G. (2012) Optically Induced Birefringence and Holography in Silk. *Journal of Polymer Science Part B-Polymer Physics 50*, 257-262.

121. Lefèvre, T., Paquet-Mercier, F., Rioux-Dube, J. F., and Pezolet, M. (2012) Review Structure of Silk by Raman Spectromicroscopy: From the Spinning Glands to the Fibers. *Biopolymers 97*, 322-336.

122. Zhou, P., Xie, X., Knight, D. P., Zong, X. H., Deng, F., and Yao, W. H. (2004) Effects of pH and Calcium Ions on the Conformational Transitions in Silk Fibroin Using 2D Raman Correlation Spectroscopy and ^{13}C Solid-State NMR. *Biochemistry 43*, 11302-11311.

123. Zheng, S. D., Li, G. X., Yao, W. H., and Yu, T. Y. (1989) Raman-Spectroscopic Investigation of the Denaturation Process of Silk Fibroin. *Appl Spectrosc 43*, 1269-1272.

124. Gillespie, D. B., Viney, C., and Yager, P. (1994) Raman-Spectroscopic Analysis of the Secondary Structure of Spider Silk Fiber. in *Silk Polymers: Materials Science and Biotechnology* (Kaplan, D., Adams, W. W., Farmer, B., and Viney, C. eds.), Amer Chemical Soc, Washington. pp 155-167

125. Sirichaisit, J., Brookes, V. L., Young, R. J., and Vollrath, F. (2003) Analyis of Structure/Property Relationships in Silkworm (Bombyx Mori) and Spider Dragline (Nephila Edulis) Silks Using Raman Spectroscopy. *Biomacromolecules 4*, 387-394.

126. Shao, Z., Young, R. J., and Vollrath, F. (1999) The Effect of Solvents on Spider Silk Studied by Mechanical Testing and Single-Fibre Raman Spectroscopy. *Int J Biol Macromol 24*, 295-300.

127. Frisk, S., Ikeda, R. M., Chase, D. B., and Rabolt, J. F. (2003) Rotational Invariants for Polarized Raman Spectroscopy. *Appl Spectrosc 57*, 1053-1057.

128. Lefèvre, T., Rousseau, M. E., and Pezolet, M. (2006) Orientation-Insensitive Spectra for Raman Microspectroscopy. *Appl Spectrosc 60*, 841-846.

129. Rousseau, M. E., Lefèvre, T., Beaulieu, L., Asakura, T., and Pezolet, M. (2004) Study of Protein Conformation and Orientation in Silkworm and Spider Silk Fibers Using Raman Microspectroscopy. *Biomacromolecules 5*, 2247-2257.

130. Rousseau, M. E., Beaulieu, L., Lefèvre, T., Paradis, J., Asakura, T., and Pezolet, M. (2006) Characterization by Raman Microspectroscopy of the Strain-Induced Conformational Transition in Fibroin Fibers from the Silkworm Samia Cynthia Ricini. *Biomacromolecules 7*, 2512-2521.

131. Jalili, N., and Laxminarayana, K. (2004) A Review of Atomic Force Microscopy Imaging Systems: Application to Molecular Metrology and Biological Sciences. *Mechatronics 14*, 907-945.

132. Seo, Y., and Jhe, W. (2008) Atomic Force Microscopy and Spectroscopy. *Rep Prog Phys 71*, 1-23.

133. Vernon-Parry, K. D. (2000) Scanning Electron Microscopy: An Introduction. *III-Vs Review 13*, 40-44.

134. Gullekson, C., Lucas, L., Hewitt, K., and Kreplak, L. (2011) Surface-Sensitive Raman Spectroscopy of Collagen I Fibrils. *Biophys J 100*, 1837-1845.

135. Li, G., Zhou, P., Shao, Z., Xie, X., Chen, X., Wang, H., Chunyu, L., and Yu, T. (2001) The Natural Silk Spinning Process. A Nucleation-Dependent Aggregation Mechanism? *Eur J Biochem 268*, 6600-6606.

136. Chen, L., Gu, X., Fasolka, M. J., Martin, J. W., and Nguyen, T. (2009) Effects of Humidity and Sample Surface Free Energy on AFM Probe-Sample Interactions and Lateral Force Microscopy Image Contrast. *Langmuir 25*, 3494-3503.

Appendix: Copyright Permission Letter

JOHN WILEY AND SONS LICENSE TERMS AND CONDITIONS

Jan 27, 2016

This Agreement between Nathan Weatherbee ("You") and John Wiley and Sons ("John Wiley and Sons") consists of your license details and the terms and conditions provided by John Wiley and Sons and Copyright Clearance Center.

License Number	3797140445073
License date	Jan 27, 2016
Licensed Content Publisher	John Wiley and Sons
Licensed Content Publication	Entomological Research
Licensed Content Title	Organization of the spinnerets and spigots in the orb web spider, Argiope bruennichi (Araneae: Araneidae)
Licensed Content Author	Myung-Jin Moon
Licensed Content Date	Feb 1, 2012
Pages	9
Type of use	Dissertation/Thesis
Requestor type	University/Academic
Format	Print and electronic
Portion	Figure/table
Number of figures/tables	1
Original Wiley figure/table number(s)	Figure 2. Scanning electron micrographs of the spinnerets in adult (a–c) and subadult (d–f) female spiders. (a,d) The spinnerets are located at the posterior end of the ventral surface on the abdomen as a complex spinning apparatus. Of the three pairs of spinnerets, the anterior spinnerets (AS) are the biggest, and the median spinnerets (MS) are the smallest. (b,e) One pair of ampullate spigots (arrows) and more than 200 pairs of pyriform spools (Py) are compactly distributed on the anterior spinnerets. (c,f) The spigot of the major ampullate gland (Am) is the most prominent on the anterior spinneret and lies in a depressed area separated from the spools of the pyrifoms. MS, median spinneret. Scale bars indicate 500 mm (a), 250 mm (b,d,e), and 100 mm (c,f), respectively.
Will you be translating?	No
Title of your thesis / dissertation	Development and optimization of automated fibre production for recombinant spider wrapping silk
Expected completion date	Apr 2016
Expected size (number of pages)	150
Requestor Location	Nathan Weatherbee-Martin 5850 College St., Room 9-B1 Halifax, NS B3H 4R2 Canada

	Attn: Nathan Weatherbee-Martin
Billing Type	Invoice
Billing Address	Nathan Weatherbee-Martin 5850 College St., Room 9-B1 Halifax, NS B3H 4R2 Canada Attn: Nathan Weatherbee-Martin
Total	0.00 CAD

Terms and Conditions

TERMS AND CONDITIONS

This copyrighted material is owned by or exclusively licensed to John Wiley & Sons, Inc. or one of its group companies (each a"Wiley Company") or handled on behalf of a society with which a Wiley Company has exclusive publishing rights in relation to a particular work (collectively "WILEY"). By clicking "accept" in connection with completing this licensing transaction, you agree that the following terms and conditions apply to this transaction (along with the billing and payment terms and conditions established by the Copyright Clearance Center Inc., ("CCC's Billing and Payment terms and conditions"), at the time that you opened your RightsLink account (these are available at any time at http://myaccount.copyright.com).

Terms and Conditions

- The materials you have requested permission to reproduce or reuse (the "Wiley Materials") are protected by copyright.
- You are hereby granted a personal, non-exclusive, non-sub licensable (on a stand-alone basis), non-transferable, worldwide, limited license to reproduce the Wiley Materials for the purpose specified in the licensing process. This license, **and any CONTENT (PDF or image file) purchased as part of your order,** is for a one-time use only and limited to any maximum distribution number specified in the license. The first instance of republication or reuse granted by this license must be completed within two years of the date of the grant of this license (although copies prepared before the end date may be distributed thereafter). The Wiley Materials shall not be used in any other manner or for any other purpose, beyond what is granted in the license. Permission is granted subject to an appropriate acknowledgement given to the author, title of the material/book/journal and the publisher. You shall also duplicate the copyright notice that appears in the Wiley publication in your use of the Wiley Material. Permission is also granted on the understanding that nowhere in the text is a previously published source acknowledged for all or part of this Wiley Material. Any third party content is expressly excluded from this permission.
- With respect to the Wiley Materials, all rights are reserved. Except as expressly granted by the terms of the license, no part of the Wiley Materials may be copied, modified, adapted (except for minor reformatting required by the new Publication), translated, reproduced, transferred or distributed, in any form or by any means, and no derivative works may be made based on the Wiley Materials without the prior permission of the respective copyright owner.**For STM Signatory Publishers clearing permission under the terms of the STM Permissions Guidelines only, the**

terms of the license are extended to include subsequent editions and for editions in other languages, provided such editions are for the work as a whole in situ and does not involve the separate exploitation of the permitted figures or extracts, You may not alter, remove or suppress in any manner any copyright, trademark or other notices displayed by the Wiley Materials. You may not license, rent, sell, loan, lease, pledge, offer as security, transfer or assign the Wiley Materials on a stand-alone basis, or any of the rights granted to you hereunder to any other person.

- The Wiley Materials and all of the intellectual property rights therein shall at all times remain the exclusive property of John Wiley & Sons Inc, the Wiley Companies, or their respective licensors, and your interest therein is only that of having possession of and the right to reproduce the Wiley Materials pursuant to Section 2 herein during the continuance of this Agreement. You agree that you own no right, title or interest in or to the Wiley Materials or any of the intellectual property rights therein. You shall have no rights hereunder other than the license as provided for above in Section 2. No right, license or interest to any trademark, trade name, service mark or other branding ("Marks") of WILEY or its licensors is granted hereunder, and you agree that you shall not assert any such right, license or interest with respect thereto

- NEITHER WILEY NOR ITS LICENSORS MAKES ANY WARRANTY OR REPRESENTATION OF ANY KIND TO YOU OR ANY THIRD PARTY, EXPRESS, IMPLIED OR STATUTORY, WITH RESPECT TO THE MATERIALS OR THE ACCURACY OF ANY INFORMATION CONTAINED IN THE MATERIALS, INCLUDING, WITHOUT LIMITATION, ANY IMPLIED WARRANTY OF MERCHANTABILITY, ACCURACY, SATISFACTORY QUALITY, FITNESS FOR A PARTICULAR PURPOSE, USABILITY, INTEGRATION OR NON-INFRINGEMENT AND ALL SUCH WARRANTIES ARE HEREBY EXCLUDED BY WILEY AND ITS LICENSORS AND WAIVED BY YOU.

- WILEY shall have the right to terminate this Agreement immediately upon breach of this Agreement by you.

- You shall indemnify, defend and hold harmless WILEY, its Licensors and their respective directors, officers, agents and employees, from and against any actual or threatened claims, demands, causes of action or proceedings arising from any breach of this Agreement by you.

- IN NO EVENT SHALL WILEY OR ITS LICENSORS BE LIABLE TO YOU OR ANY OTHER PARTY OR ANY OTHER PERSON OR ENTITY FOR ANY SPECIAL, CONSEQUENTIAL, INCIDENTAL, INDIRECT, EXEMPLARY OR PUNITIVE DAMAGES, HOWEVER CAUSED, ARISING OUT OF OR IN CONNECTION WITH THE DOWNLOADING, PROVISIONING, VIEWING OR USE OF THE MATERIALS REGARDLESS OF THE FORM OF ACTION, WHETHER FOR BREACH OF CONTRACT, BREACH OF WARRANTY, TORT, NEGLIGENCE, INFRINGEMENT OR OTHERWISE (INCLUDING, WITHOUT LIMITATION, DAMAGES BASED ON LOSS OF PROFITS, DATA, FILES, USE, BUSINESS OPPORTUNITY OR CLAIMS OF THIRD PARTIES), AND WHETHER OR NOT THE PARTY HAS BEEN ADVISED OF THE POSSIBILITY OF SUCH DAMAGES. THIS LIMITATION SHALL APPLY

NOTWITHSTANDING ANY FAILURE OF ESSENTIAL PURPOSE OF ANY LIMITED REMEDY PROVIDED HEREIN.

- Should any provision of this Agreement be held by a court of competent jurisdiction to be illegal, invalid, or unenforceable, that provision shall be deemed amended to achieve as nearly as possible the same economic effect as the original provision, and the legality, validity and enforceability of the remaining provisions of this Agreement shall not be affected or impaired thereby.

- The failure of either party to enforce any term or condition of this Agreement shall not constitute a waiver of either party's right to enforce each and every term and condition of this Agreement. No breach under this agreement shall be deemed waived or excused by either party unless such waiver or consent is in writing signed by the party granting such waiver or consent. The waiver by or consent of a party to a breach of any provision of this Agreement shall not operate or be construed as a waiver of or consent to any other or subsequent breach by such other party.

- This Agreement may not be assigned (including by operation of law or otherwise) by you without WILEY's prior written consent.

- Any fee required for this permission shall be non-refundable after thirty (30) days from receipt by the CCC.

- These terms and conditions together with CCC's Billing and Payment terms and conditions (which are incorporated herein) form the entire agreement between you and WILEY concerning this licensing transaction and (in the absence of fraud) supersedes all prior agreements and representations of the parties, oral or written. This Agreement may not be amended except in writing signed by both parties. This Agreement shall be binding upon and inure to the benefit of the parties' successors, legal representatives, and authorized assigns.

- In the event of any conflict between your obligations established by these terms and conditions and those established by CCC's Billing and Payment terms and conditions, these terms and conditions shall prevail.

- WILEY expressly reserves all rights not specifically granted in the combination of (i) the license details provided by you and accepted in the course of this licensing transaction, (ii) these terms and conditions and (iii) CCC's Billing and Payment terms and conditions.

- This Agreement will be void if the Type of Use, Format, Circulation, or Requestor Type was misrepresented during the licensing process.

- This Agreement shall be governed by and construed in accordance with the laws of the State of New York, USA, without regards to such state's conflict of law rules. Any legal action, suit or proceeding arising out of or relating to these Terms and Conditions or the breach thereof shall be instituted in a court of competent jurisdiction in New York County in the State of New York in the United States of America and each party hereby consents and submits to the personal jurisdiction of such court, waives any objection to venue in such court and consents to service of process by

registered or certified mail, return receipt requested, at the last known address of such party.

WILEY OPEN ACCESS TERMS AND CONDITIONS

Wiley Publishes Open Access Articles in fully Open Access Journals and in Subscription journals offering Online Open. Although most of the fully Open Access journals publish open access articles under the terms of the Creative Commons Attribution (CC BY) License only, the subscription journals and a few of the Open Access Journals offer a choice of Creative Commons Licenses. The license type is clearly identified on the article.

The Creative Commons Attribution License

The Creative Commons Attribution License (CC-BY) allows users to copy, distribute and transmit an article, adapt the article and make commercial use of the article. The CC-BY license permits commercial and non-

Creative Commons Attribution Non-Commercial License

The Creative Commons Attribution Non-Commercial (CC-BY-NC)License permits use, distribution and reproduction in any medium, provided the original work is properly cited and is not used for commercial purposes.(see below)

Creative Commons Attribution-Non-Commercial-NoDerivs License

The Creative Commons Attribution Non-Commercial-NoDerivs License (CC-BY-NC-ND) permits use, distribution and reproduction in any medium, provided the original work is properly cited, is not used for commercial purposes and no modifications or adaptations are made. (see below)

Use by commercial "for-profit" organizations

Use of Wiley Open Access articles for commercial, promotional, or marketing purposes requires further explicit permission from Wiley and will be subject to a fee.
Further details can be found on Wiley Online Library
http://olabout.wiley.com/WileyCDA/Section/id-410895.html

Other Terms and Conditions:

v1.10 Last updated September 2015

Questions? customercare@copyright.com or +1-855-239-3415 (toll free in the US) or +1-978-646-2777.